

Physics of natural nanoparticles - water interfaces: chemical reactivity and environmental implications

Alejandro Fernandez-Martinez

▶ **To cite this version:**

Alejandro Fernandez-Martinez. Physics of natural nanoparticles - water interfaces: chemical reactivity and environmental implications. Mineralogy. Université de Grenoble, 2009. English. NNT : . tel-00771937

HAL Id: tel-00771937
https://theses.hal.science/tel-00771937

Submitted on 9 Jan 2013

HAL is a multi-disciplinary open access archive for the deposit and dissemination of scientific research documents, whether they are published or not. The documents may come from teaching and research institutions in France or abroad, or from public or private research centers.

L'archive ouverte pluridisciplinaire **HAL**, est destinée au dépôt et à la diffusion de documents scientifiques de niveau recherche, publiés ou non, émanant des établissements d'enseignement et de recherche français ou étrangers, des laboratoires publics ou privés.

OBSERVATOIRE DE GRENOBLE
et
LABORATOIRE DE GEOPHYSIQUE INTERNE ET TECTONOPHYSIQUE

THESE

Physics of natural nanoparticles – water interfaces: chemical reactivity and environmental implications

présentée par

Alejandro Fernández-Martínez

pour obtenir le titre de
Docteur de l'Université Joseph Fourier – Grenoble I

Spécialité : **Géochimie environnementale**

Composition du jury:

Prof. Björn Winkler	rapporteur	Universitat Frankfurt, Germany
Prof. Neil T. Skipper	rapporteur	UCL, London, U.K.
Dr. Jêrome Rose	examinateur	CEREGE, Aix en Provence, France
Dr. Victor F. Puntes	examinateur	Institut Catalá de Nanotecnologia, Barcelona, Spain
Dr. Gabriel J. Cuello	examinateur, co-directeur de thése	Institut Laue-Langevin, Grenoble, France
Prof. Laurent Charlet	examinateur, co-directeur de thése	Université Joseph-Fourier Grenoble I, France

Abstract

Precise structural studies of nano-crystalline minerals using diffraction techniques have been hindered by the broad diffraction peaks found in their diffraction patterns. In this thesis, I have applied molecular scale techniques such as High-Energy X-ray Diffraction and Molecular Dynamics simulations to study the structure and reactivity of two nano-minerals of important environmental significance: imogolite and schwertmannite. These minerals have nanotube or channel-like structures, and both are strong anion adsorbers.

Imogolite is a nanotubular aluminosilicate present in the clay fraction of volcanic soils. It has high specific surface areas and it is one of the few minerals reactive towards anions and cations, which makes it a very important mineral in soils where it is found. However, the prediction of imogolite chemical reactivity is hindered by its nano-crystalline character. Structural studies up to now have been restricted to X-Ray Diffraction and Electron Diffraction analyses, where the diffraction peaks were used mainly as fingerprints for the identification of the mineral. In this thesis I have performed a detailed structural characterisation of the structure of synthetic imogolite by Transmission Electron Microscopy (TEM), High-Energy X-ray and Molecular Dynamics methods. In addition, the structure of water at the imogolite / water interface has been investigated by theoretical and experimental methods. Using these structural inputs, I have developed a geochemical MUSIC model of imogolite, and compared it to the existing models for Gibbsite (planar equivalent of the external surface of imogolite), evaluating the effect of the curvature on geochemical reactivity. Parameters investigated include, the number of hydrogen bonds per surface adsorption site or the protonation constants of surface hydroxyl groups.

Finally, these molecular-scale investigations have been linked to the biogeochemistry of Selenium in volcanic soils (andisols). Andisols are frequently rich in Selenium but controversially often low in bioavailable selenium. At the same time, imogolite is often found in the clay fraction of these soils. The adsorption of Selenium oxyanions at the Imogolite/water interface has been studied using X-ray Absorption Spectroscopy and DFT methods.

In contrast to imogolite, schwertmannite structure is thought to be akin to that of akaganeite, with sulphate molecules substituting chlorine atoms in channels. The structure of the octahedral iron frame and the positions of the sulphate molecules within the structure have been object of an intense debate during the last 15 years. I present here a combined Pair-Distribution Function and X-ray Diffraction Study of the structure of schwertmannite. A structural model is proposed and discussed in terms of the retention of oxyanions.

Contents

1.- Introduction **1**

1.1.- Mineral nanoparticles 1

1.1.1.- Imogolite nanotubes 2

1.1.2.- Nanoparticles in Acid/Rock Mine Drainage: Schwertmannite 7

1.2.- Selenium bioavailability in volcanic soils: relevance of imogolite nanotubes 9

1.3.- Diffraction techniques for structural studies of environmental nanoparticles 12

2.- Experimental and theoretical methods **21**

2.1.- Pair Distribution Function technique 21

2.2.- X-ray Absorption Spectroscopy 23

2.3.- Simulations 26

2.3.1.- *Ab-initio* DFT calculations 26

2.3.2.- Classical Molecular Dynamics and Monte Carlo simulations 29

2.3.2.1.- Molecular Dynamics method 30

2.3.2.2.- Monte Carlo method 32

3.- Selenite and selenate adsorption mechanisms at the synthetic and biogenic imogolite – water interface **37**

3.1.- Introduction 37

3.2.- Selenite and selenate adsorption mechanisms at the imogolite – water interface 43

4.- Molecular dynamics investigation of the structure of water at the imogolite and gibbsite – water interfaces: effect of the curvature on the hydrophilicity and surface acidity **75**

4.1.- Introduction 75

4.2.- Water structure and hydration properties of imogolite: ‘The nanotube effect’ 79

5.- The structure of schwertmannite, a nanocrystalline iron oxyhydroxysulfate **111**

5.1.- Introduction 111

5.2.- The structure of schwertmannite, a nanocrystalline iron oxyhydroxysulfate 113

6.- Conclusions **139**

Annex I. Multi-scale characterization of synthetic imogolite **145**

Annex II. Other publications **163**

Chapter 1

Introduction

1.1.- Mineral nanoparticles

This thesis is devoted to the study of two mineral nanoparticles commonly found in some environmental compartments. Imogolite, an aluminosilicate clay mineral with nanotubular structure, is commonly found in the clay fraction of volcanic soils or in spodosols. Schwertmannite, an iron oxyhydroxysulfate, forms in acid mine drainage sites where Fe^{2+}-rich mine waters are mixed with oxygenated waters, forming Fe oxyhydroxide nanoparticles by hydrolysis. These two mineral nanoparticles are just a sample of a wide collection of nanoparticles present in the environment as a result of weathering, oxido-reduction, detoxification and microbial processes, between others. Mineral nanoparticles are usually formed in hydrous environments, and thus water is commonly found in their structures, determining many of their properties as, *e.g.*, their aggregation, shape or their surface chemistry. Furthermore, they usually contain hydroxyl groups on their surfaces, which affect their hydrophilicity and thus their solubility. In addition, the disorder associated with the lack of long-range order in their structure challenges any structural study by classical methods as laboratory X-ray diffraction. This fact stress the need for new experimental and theoretical techniques that can be applied to the study of these challenging mineral nanoparticles structures.

Some of the experimental and theoretical methods used in this thesis are commonly applied in other research areas. The Pair Distribution Function (PDF) technique is the 1-D equivalent to the Patterson function technique, a method widely used in the field of protein crystallography. This method has been used during many years to structural studies of liquids and amorphous materials, and it has been only recently that its application to the study of engineered and natural nanoparticles is becoming very popular. The Molecular Dynamics (MD) technique is a theoretical method that has been largely applied to the study of clay minerals. However, the development of accurate sets

of potential parameters has made that its use to the study of mineral nanoparticles is starting only now.

MD simulations have shed light to the water adsorption properties of imogolite. Imogolite has been found to be less hydrophilic than gibbsite –the planar equivalent of the imogolite's external surface–. The curvature of the structure affects its water adsorption properties through changes in the hydrogen-bonding structure of surface hydroxyl groups. This result, stress the importance of the curvature in mineral surfaces, an effect that is commonly found in minerals with tubular or spherical shapes, or with high densities of edge sites, as in most mineral nanoparticles.

In addition, a study of the retention mechanisms of selenium oxyanions on imogolite is presented, showing the environmental relevance of this mineral nanoparticle in the mobility and bioavailability of selenium in volcanic soils.

1.1.1.- Imogolite nanotubes

Imogolite ($Al_2(OH)_3SiO_3OH$) is an aluminosilicate mineral commonly found in soil environments such as the clay fractions of volcanic ash soils or in spodosols (Dahlgren and Ugolini, 1989; Dahlgren and Ugolini, 1991; Ugolini and Dahlgren, 1991; Wada, 1989). Imogolite has a nanotubular geometry, with an internal face dominated by silanol (>$SIOH^0$) functional groups and an external face composed by a curved gibbsite ($Al(OH)_3$), populated by neutral aluminol groups (>Al_2OH^0) (see Figure 1.1).

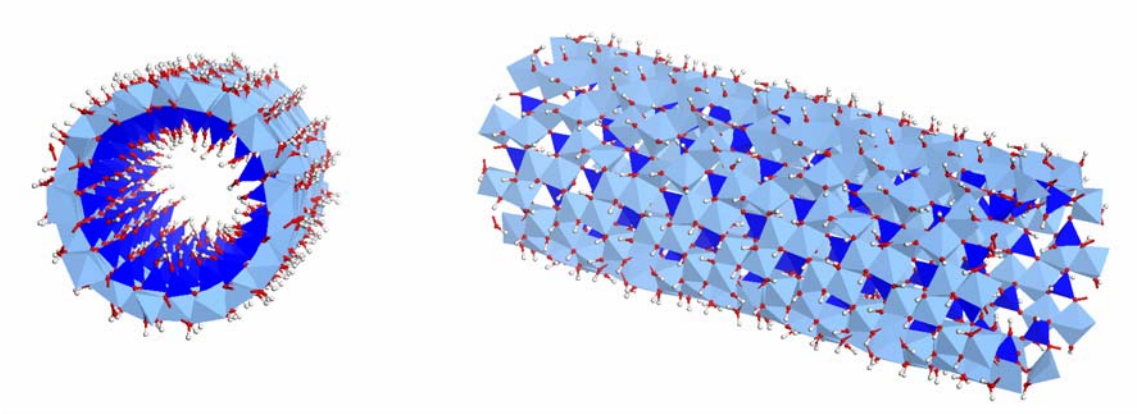


Figure 1.1.- *Two views of the structure of imogolite. Light blue polyhedra are aluminum octahedra. Dark blue are silicon tetrahedral. Red and white spheres are oxygen and hydrogen atoms respectively.*

The presence of these amphoteric surfaces and the lack of isomorphic substitutions (which would act as centers of permanent charge) make imogolite a mineral with a variable charge only dependent on the pH of the solution. However, some authors have hypothesized the existence of a permanent charge, although this hypothesis has not been proved yet experimentally (Alvarez-Ramirez, 2007; Guimaraes et al., 2007; Gustafsson, 2001).

The surface charge of imogolite is complex. The presence of a double surface makes difficult its study by macroscopic wet chemistry methods. Potentiometric titrations of natural imogolite under different ionic strengths have been measured by (Tsuchida et al., 2004), revealing a Point of Zero Salt Effect (PZSE) at pH 6. The net adsorbed ion charge (Δq) in function of pH was determined by Karube *et al.*, obtaining a Point of Zero Net Charge (PZNC) at pH 6 (Karube et al., 1992). The combination of both curves can be done in a *Chorover plot* (Figure 1.2) (Chorover and Sposito, 1995; Sposito, 2004). The intercept of the linear regression of the data gives a value for the permanent structural charge (according to the equation $\Delta q = -\Delta_H - \Delta_0$) which is practically zero ($\Delta_0 = 16 \pm 10$ $mmol_c$ kg^{-1}, to be compared, *e.g.*, with 440 $mmol_c$ kg^{-1} of a synthetic montmorillonite (Gehin et al., 2007)).

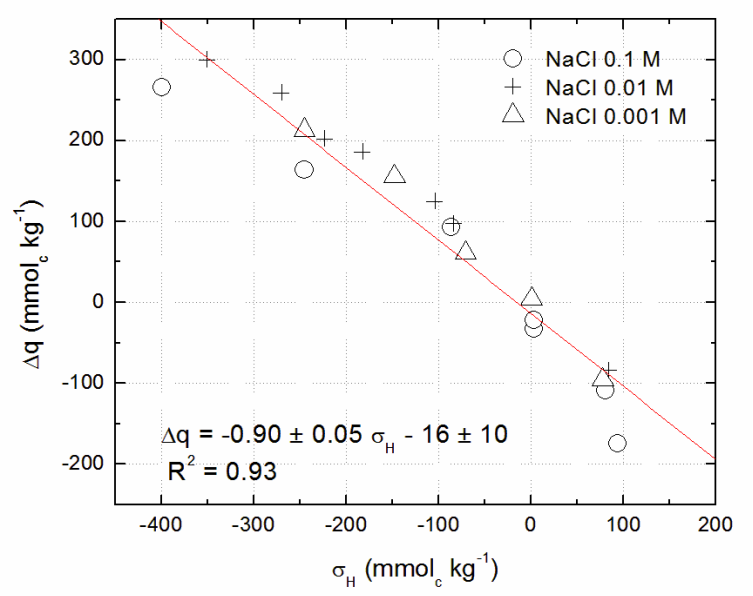


***Figure 1.2**. Plot of the net adsorbed ion charge against the net adsorbed proton charge for natural Imogolite. Data have been taken from Tsuchida et al. (2005). A specific surface of 818 m^2 g^{-1} has been considered. This value is the 'crystallographic' specific surface of Imogolite considering a hydration level of 15% (in mass).*

This would indicate that imogolite bears no permanent structural charge. However, the geometry of imogolite makes that estimations made using this method could be erroneous. The fact that the double-layers of adsorption of the internal and external faces do not overlap makes that the total charge measured by macroscopic methods is the *sum* of the charges developed at both surfaces. These methods are thus not valid to ascertain the existence of a permanent charge at the imogolite surface.

The hypothesis of a permanent charge was proposed by (Gustafsson, 2001). He proposed that the shortening of the outer (closer to the external surface) Al-O bond lengths caused by the curvature of the gibbsite-like atomic sheet leads to a slight oversaturation of the charge of O atoms (positive charge) (Gustafsson, 2001). Inversely, small elongations of the internal (closer to the internal surface) Al-O bond lengths would induce O undersaturation (negative charge). This hypothesis has been confirmed by DFT calculations that show a displacement of the electronic density towards the internal face of the imogolite nanotubes. If Gustafson's hypothesis is right, and imogolite develops a positive charge at its external surface and a negative charge at its internal surface, the total effect of both charges would be cancelled out in any macroscopic measurement, as it has been mentioned previously. On the other hand, the fact that the Chorover plot does not reveal any permanent charge could be also explained if this charge is very small. This is the case of the charge calculated by DFT: calculated Mulliken charges are only 6% bigger for the inner H atoms than for the external ones.

At the same time, while acid-base potentiometric titrations have shown that imogolite develops both positive and negative charges in function of the pH, electrophoretic mobility studies indicate that imogolite has only a positive charge (Karube et al., 1992; Su and Harsh, 1993; Tsuchida et al., 2004). Tsuchida et al. (2005) have shown that this discrepancy can be explained in terms of imogolite's tubular geometry: they propose that the silanol groups ($>SiOH^0$) present in the internal surface do not have any effect on the electrokinetic properties of imogolite, being only the external surface relevant for imogolite electrophoresis mobility measurements.

However, the classically adduced explanation for the occurrence of a permanent charge and for the adsorption of anions at the imogolite − water interface is the presence of vacancies in aluminum octahedral sites. These vacancies would originate $>AlOH^{-1/2}$ surface groups whose pK_{a1} has been predicted to be at $pK_{a1} = 10$ (equation 1)

(Gustafsson, 2001), implying that these sites would be positively charged at solution pH values lower than 10,

$$> AlOH_2^{+1/2} \leftrightarrow \quad > AlOH^{-1/2} + H^+ \qquad (1)$$

These two hypotheses would explain also the positive values of electrophoretic mobility found by some authors (Su and Harsh, 1993; Tsuchida et al., 2004) (see Figure 1.3)

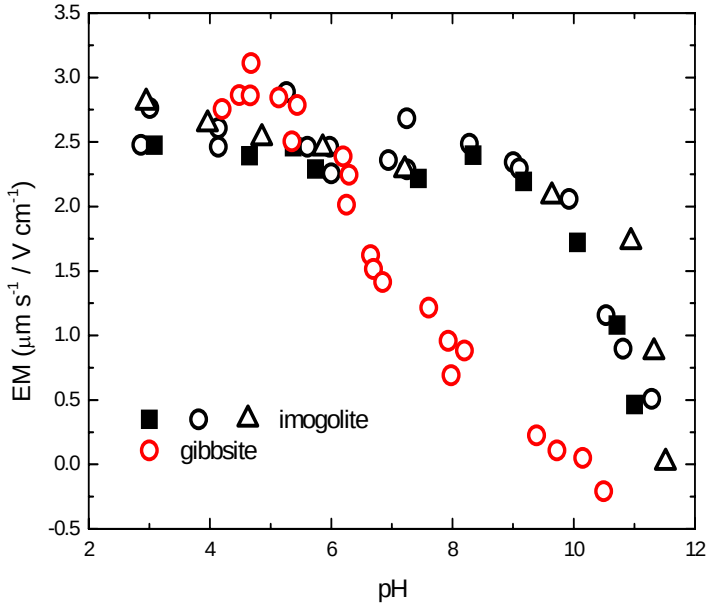


Figure 1.3.- *Electrophoretic mobility of imogolite and gibbsite. Data for gibbsite is from (Rosenqvist et al., 2002), at an ionic strength of I = 0.1 M NaCl. Circles and squares represent data from (Harsh et al., 1992) at ionic strengths of I = 0.01 M NaCl and Squares are data at I = 0.01 M CsCl respectively. Triangles are data from (Su and Harsh, 1993) at I = 0.01 M NaCl.*

Imogolite is an important component in the soils where it occurs. Its small size, with an external diameter of 2.2 nm and tube lengths in the order of the micron, and its poor crystallinity give it large specific surface areas. Brunauer, Emmett and Teller (BET) measurements using N_2 before and after degassing at 275 ºC yielded 400 m^2/g (Ackerman et al., 1993). It is important to note that these BET values are much smaller than the ideal crystallographic value of a dry imogolite nanotube, which would be of ~1200 m^2/g. Different reasons can be invoked to explain this difference:

- Imogolite nanotubes form bundles, therefore reducing the accessible area for the adsorption of N_2 molecules (Ackerman et al., 1993; Mukherjee et al., 2005).

- The formation of these bundles makes that imogolite develops porosity. Thermogravimetric analyses have shown that water is still present in these pores at the temperature where the dehydroxylation (and hence the collapse of the tubular structure) occurs (Annex I). Measured values of water content by Controlled Rate Thermal Analyses (Annex I) yield a weight fraction of 13% (w/w) at 275 ºC, equivalent to a water content of one hydration layer. This strongly adsorbed water contributes to reduce the specific surface area measured by BET methods.
- The internal pore of imogolite has a diameter of ~1 nm (Cradwick et al., 1972). This small size and the high density of silanol groups on the surface create an environment with a high electrostatic potential, where water molecules may be very strongly adsorbed. This has been shown by Creton *et al.* (2008) who calculated values of the diffusion coefficients of the water molecules in the internal pore four times smaller than for bulk water (Creton et al., 2008a).

Water is thus an important component of the imogolite structure. However, only few studies have focused on the structure and dynamics of water adsorbed on imogolite (Ackerman et al., 1993; Creton et al., 2008a; Creton et al., 2008b; Farmer et al., 1983). Creton *et al.* (2008a,b) performed Molecular Dynamics (MD) simulations of the water present in the inter-tube pores of hexagonal close-packed bundles of imogolite showing that water interacts with the silanol groups much strongly than with the aluminol groups on the external surface. This strong interaction and the reduced size of the internal pore (diameter ≈ 1 nm) difficult the diffusion of water along the tube axis (Zang et al., 2009), making the external imogolite surface the more relevant face from a geochemical point of view (Arai et al., 2006).

Chapter 4 of this thesis presents a theoretical MD study of the water structure at the gibbsite and at the external imogolite surface. Adsorption energies and patching effects at the surface are discussed, and their impact on the surface chemistry of imogolite is discussed. MD simulations allow studying the behavior of water at the internal and external surfaces of imogolite separately. The use of some experimental methods, like thermogravimetry and infrared spectroscopy is presented in the Annex I, which stress the needs for other spectroscopic techniques to be applied in the study of water structure and dynamics on imogolite.

Although much advance has been done in the understanding of the charge behavior of mineral surfaces, the surface acidity constant –or protonation constant– is revealing as a much more dynamic concept than it was thought. The studies about the protonation constants of gibbsite are a good example of the evolution of this concept. Hiemstra et al. (1996) developed a MUSIC model for gibbsite reporting values for the first (pK_{a1}) and second (pK_{a2}) protonation constants of the (001) surface sites of 0 and 11.9, respectively (Hiemstra and VanRiemsdijk, 1996; Hiemstra et al., 1996). More recently other authors have applied *ab-initio* molecular modeling combined with a bond-valence analysis to the determination of intrinsic protonation constant values, showing the predicted dependence on the mineral surface charge (Bickmore et al., 2004; Schindler and Stumm, 1987). These authors have reported one value (pKa1 = 5.2) in a pH range of environmental relevance, and very similar to the experimental value of 5.9 ± 0.2 reported by Gan *et al.* (2006) (Bickmore et al., 2004). The accurate determination of surface acidity constants seems then a difficult task. The new spectroscopic methods as the one described by Gan *et al.* (2006) are only applicable to the study of mineral surfaces with no defects and relatively large surfaces (in the order of the μm^2). The determination of acidity constants for functional groups belonging to minerals with sizes in the nanoscale is thus very difficult to attain experimentally.

In the case of imogolite, the big size of the unit cell prevents the use of *ab-initio* molecular dynamics techniques that could be applied in the same way as Bickmore *et al*. (2004) did for the surface of gibbsite. *For this reason, in this thesis, we have chosen to use classical MD to study the hydrated surfaces of gibbsite and imogolite, and to evaluate the effect that the curvature of the imogolite surface has over the structure and energetics of adsorbed water. Simulations are also useful to constrain the number of hydrogen bonds per surface adsorption site, a parameter that is usually fitted in surface complexation models.*

1.1.2.- Nanoparticles in Acid/Rock Mine Drainage: Schwertmannite

Schwertmannite is a poorly crystalline ferric oxyhydroxysulfate that forms ochreous coatings on sulfide-bearing rocks and soils. It also precipitates in streams and lakes receiving acid mine drainage where the weathering of iron sulfide minerals produces SO_4 and Fe(II) acid solutions. When exposed to the atmosphere, bacterially mediated oxidation of Fe(II) occurs and large quantities of nanoparticulated Fe(III) phases may

form. Moreover, schwertmannite is a key solid in removing acidity in treatment systems where Fe(II) is rapidly oxidized by addition of alkalinity to acid mine drainage (Gagliano et al., 2004; Rotting et al., 2008). Further, in anoxic environments such as acid lakes, flooded soils and wetlands, schwertmannite particles can serve as electron acceptor for Fe(III) reducing bacteria, releasing the Fe(II) necessary for sulfate reduction and neoformation of iron sulfides (Burton et al., 2007). Schwertmannite forms aggregates of nanoparticles of typical hedge-hog morphology (see Figure 1.4)

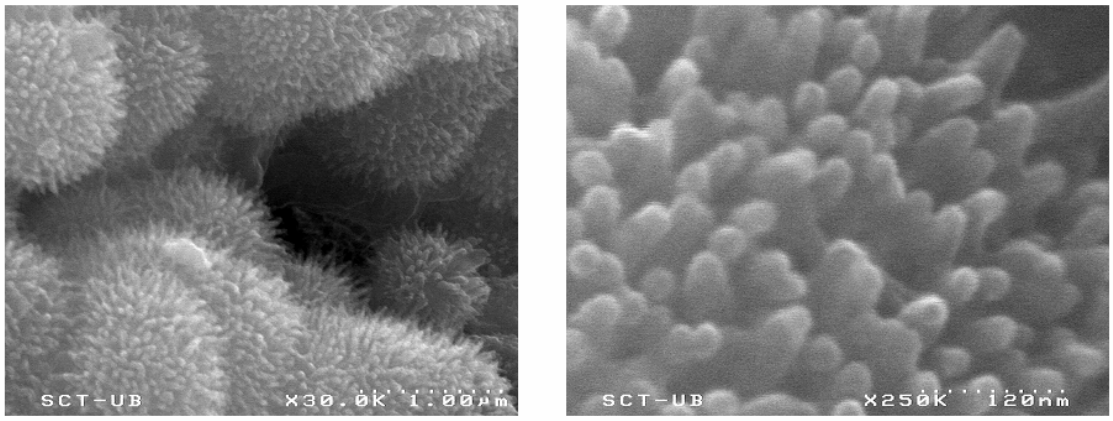


Figure 1.4*. Scanning Electron Micrographs of schwertmanite aggregates, showing the typical hedge-hog morphology. Image courtesy of Carles Ayora (CSIC, Barcelona, Spain).*

Due to its high specific surface and positive charge in acid waters, schwertmannite efficiently removes oxyanions such as AsO_4^{3-}, SeO_4^{2-} and CrO_4^{2-} from water (Carlson et al., 2002; Regenspurg and Peiffer, 2005; Waychunas et al., 1995). However, despite its ubiquity and its important geochemical role, schwertmannite was only recently recognized as a mineral (Bigham et al., 1994). Reasons for this late recognition include its poor crystallinity, its frequent association with more crystalline phases such as goethite and jarosite, and its metastable structure, which transforms into goethite and jarosite within months (Acero et al., 2006; Bigham et al., 1996).

In this thesis, a combined study of Pair Distribution Functions, X-ray diffraction patterns and electronic structure calculations has been successfully applied to the resolution of the structure of schwertmannite. This structure has been a subject of debate since its discovery, 15 years ago, due to the lack of long-range order inherent to the structure. The use of PDF allows examining the local structure of the octahedral iron frame, and fitting it against a real space model, a possibility that it is hindered in the

reciprocal space by the broad reflections present in the diffraction patterns. On the other hand, the position of the sulphate molecules within the structure has been shown to have a big impact on the intensities of some diffraction peaks. Simulations of diffraction patterns have allowed us to discern the most probable positions of the sulphates within the structure. Results from electronic structure calculations support the proposed structure obtained from PDF.

1.2.- Selenium bioavailability in volcanic soils: relevance of imogolite nanotubes

Selenium has been identified during long time as a dangerous substance because of its toxicity and it has been only in the recent past that its physiological importance as a trace element fundamental to health has been assessed. (Schwarz and Foltz, 1957), linked the existence of liver, muscle and heart diseases with selenium deficit. The Kashin-Beck disease, an articulation disease found in children from the north of China, north of Korea and Siberia, was shown to be related to selenium deficit in soils (Stone, 2009). Selenium is thus known as a 'double-edged sword' element, having one of the narrowest ranges between dietary deficiency (< 40 μg day^{-1}) and toxic levels (> 400 μg day^{-1}) (Levander and Burk, 2006). Therefore, it is essential to understand the physico-chemical and biological processes that govern its bioavailability in the environment.

The bioavailability of a trace element is related to the factors that make it available to an organism, that is, in a form that can be transported across the organism's biological membrane (Reeder et al., 2006). However, this concept is not very precise, as, for instance, a substance could be adsorbed on a colloidal particle small enough to pass through this membrane. This has motivated the use of the term "bioaccessibility", representing "the fraction of a substance that becomes soluble within the gut or lungs and therefore available for absorption through a membrane" (Reeder et al., 2006; Ruby et al., 1996; Ruby et al., 1999). Bioavailability and bioaccessibility rely then on a variety of entangled physico-chemical factors affecting mainly solubility of the substances, like speciation, ionic strength, pH or redox potential.

Selenium speciation: its role on selenium bioavailability

An example emphasizing the relevance of selenium bioavailability against high selenium concentrations has been provided by (Amweg et al., 2003). The authors have

studied the effects of an algae-bacterial selenium-reduction system applied to irrigation waters of the San Joaquin Valley (California, USA). The system helped to reduce 80% of the influent selenium in waters, but the concentration of selenite and organic selenium suffered an 8-fold increase. As a result of the water treatment, selenium concentrations in organisms increased 2-4 times due to the presence of these two forms of selenium, which are more bioavailable to biota than the original species. Speciation is thus a key factor in the fate of selenium species in the environment and in their availability to organisms. Usually, Se(0) is considered to have little toxicological significance to most organisms (Combs et al., 1996; Schlekat et al., 2000), although biological activity has been reported for elemental selenium nanoparticles (Zhang et al., 2005). Selenite and selenate are both water soluble inorganic species typically found in aerobic water sources. Selenite is both more bioavailable and approximately 5 to 10 times more toxic than selenate (Lemly, 1993). Organic selenium, in the form of selenide, Se(-II), is the most bioavailable form, and it is taken up by algae 1000 times more readily than inorganic forms (Lemly, 1993; Maier et al., 1993). Another example showing the importance of selenium speciation in soils on bioavailability is the case of selenium deficiency in the Zhangjiakou District of the Hebei province in China (Johnson et al., 2000). Soils from the Zhangjiakou District present an average of 0.15 mg of selenium kg^{-1}, which can be considered a low concentration, but not a critically low level. In this area, the Keshan disease, a heart disease, affects some part of the population. This disease had been usually attributed to a lack of selenium in diet. However, (Johnson et al., 2000) demonstrated that the prevalence of the disease is not correlated with a lack of selenium in the soil as might be expected. The cause for the selenium deficiency is rather a result of the fact that the soil-bound selenium is not in a form available for plants. These soils are rich in organic matter, which can be the responsible of the selenium immobilization, either through direct adsorption or through redox processes: reduction of selenate to selenite would favor the adsorption of the latter onto iron and aluminum oxyhydroxides.

Role of adsorption processes on selenium bioavailability

Apart from speciation, other factors have influence on selenium bioavailability, like the sorption properties of soils, sediments and aquifer substrates, the mobility of the different species and their solubility with respect to solid phases. Different processes at the mineral/water interface can be considered responsible for the selenium associations

with mineralogical soil components: adsorption, co-precipitation and surface precipitation processes, the two latter depending on solubility of the target solid phases. Adsorption is defined as 'the process through which a chemical substance accumulates at the common boundary of two contiguous phases' (Sposito, 2004). It highly depends on factors like ionic strength of the medium, which can reduce the adsorption properties of some minerals through the reduction of the size of Stern layer of adsorption (Sposito, 2004). Competition effects are also an important factor which may reduce selenium adsorption, *e.g.*, when fertilizers are applied on soils, like phosphates or nitrates. For instance, selenite sorption in Indian soils have been studied by (Dhillon and Dhillon, 2000), showing that selenite adsorption is reduced by a 50% when phosphate anions are present as competitors.

Selenium species can be adsorbed through two different mechanisms at the mineral/water interface (Balistrieri and Chao, 1987; Hansmann and Anderson, 1985; Neal et al., 1987a; Neal et al., 1987b): outer-sphere and inner-sphere complexation. Formation of outer-sphere complexes is an electrostatic-driven sorption mechanism, strongly dependent on surface charge and thus on solution ionic strength (Sposito, 2004). Inner-sphere complexes form when an ion is adsorbed "specifically" on a "crystallographic site", *i.e.*, when covalent or ionic bonds are created with functional sites present on the mineral faces. These bonds have a stronger degree of covalence and are more stable than outer-sphere complex formation (Sposito, 2004). They are responsible in much cases of the long-term immobilization of ions at the mineral/water interface (Duc et al., 2003).

Soils from volcanic regions, volcanic-ashes produced simultaneously to volcanic gases, and sediments developed from these ashes are usually rich in selenium (Byers et al., 1938; Davidson and Powers, 1959; Ihnat, 1989; Lakin, 1972). But, paradoxically, diseases related to selenium deficiency (*i.e.*, 'white muscle disease') have been reported in regions of the world dominated by selenium-rich volcanic soils such as andosols (Rayman, 2000). In fact, andosols are the soils with higher selenium distribution coefficients (Nakamaru et al., 2005). The particle / solution distribution coefficient (K_d) of selenium in Japanese agricultural andosols are as high as 600-800 L kg^{-1}. The origin in this apparent discrepancy is two folded: on one hand, it has been reported that the specific mineralogical characteristics of volcanic soils lead to the immobilization of

large quantities of organic matter (Wang and Chen, 2003); selenium associates with organic matter being immobilized and thus becomes unavailable to the biota (Wang and Gao, 2001). As stated above, clear difference should be made then between low bioavailability and deficiency, terms that have been used in a confusing way by some authors (Rayman, 2000; Reilly, 1997; Sirichakwal et al., 2005). On the other hand, little is known about the specific interactions of selenium oxyanions (predominant species of inorganic selenium in volcanic soils) and the mineralogical components specific to these soils (imogolite and allophane), which could be responsible of the low selenium bioavailability. Some studies have highlighted this possibility: sequential extractions performed on andosol samples have shown high correlation coefficients between occurrence of short-range-ordered aluminosilicates such as allophane, imogolite and active aluminum, and selenium K_d values (Nakamaru et al., 2005). Selenium bioavailability in these soils may be thus controlled by the adsorption of selenite and selenate, the two predominant species in those oxic soils, on mineral surfaces and organic matter.

In Chapter 3 of this thesis a study of the adsorption mechanisms of selenite, SeO_3^{2-}, and selenate, SeO_4^{2-}, the two oxyanions present in aerated soils like andosols, on two different specimens of imogolite (synthetic and biogenic) will be presented.

1.3.- Diffraction techniques for structural studies of environmental nanoparticles

Nanosize minerals present structural features that difficult their study by classical diffraction analysis methods. Atoms in their surfaces are exposed to interactions with solvents and ionic species, which cause relaxation effects and so deviations from the bulk periodic structure. Moreover, the ratio of surface atoms vs. bulk atoms scales with 1/R, being R the radius of the mineral nanoparticle (assuming spherical shape). This implies that for very small nanoparticle sizes relaxation effects will be very relevant to the average structure. On the other hand, reduced number of atoms in the bulk implies that only few atomic planes will be participating coherently in the diffraction. This translates into ill-defined Bragg peaks in the diffraction patterns, and a non-negligible diffuse scattering.

Classical diffraction analysis methods are limited under these conditions, as they rely on the Bragg peaks' positions and intensity. This kind of analyses are performed usually in the reciprocal space, through the use of convolution methods as Rietveld refinement (Rietveld, 1969), pattern reconstruction through microstructural analyses (Lanson, 1997), or following de-convolution strategies, as the Warren-Averbach method (Warren, 1969). These methods have been applied to the study of environmental nanoparticles during the last 30 years. However, in most cases present in the literature, their use has been restricted to identification purposes. This is especially true in the cases of imogolite and schwertmannite. The diffraction patterns of these two environmental nanoparticles present very broad oscillations, which prevent the use of any convolution or de-convolution technique (Barham, 1997; Bigham et al., 1994; Farmer et al., 1983; Vandergaast et al., 1985; Wada, 1989).

In some cases, the use of these techniques has led to incorrect or incomplete results, generating debates that are still open today. It is the case of the structures of the mackinawite and ferrihydrite nanoparticles (Michel et al., 2005; Michel et al., 2007a; Michel et al., 2007b; Wolthers et al., 2003). The first analysis of fresh precipitates of mackinawite presented by Wolthers *et al.* (2003) proposed a structure composed by two different tetragonal phases with different lattice parameters, one of them corresponding to the lattice planes closer to the surface of the nanoparticle. However, the analysis relied on peak fitting of very broad reflections. Recently, a paper by Michel *et al.* (2007) showed using real-space analysis of PDF functions that only one phase was necessary to describe its local atomic ordering. Interestingly, the resulting lattice parameters from the PDF analysis coincided with the lattice parameters of bulk mackinawite (Lennie et al., 1995) meaning that, in this system, relaxation effects at the surface and structural strains do not affect the nanoparticle structure. The structure of ferrihydrite has been a subject of debate over the last 20 years. The most widely accepted idea is that it is formed by three different phases: major defect-free crystallites, minor defective crystallites and ultradisperse hematite (Manceau and Gates, 1997). In a recent paper, Michel *et al.* (1997) have proposed a structure with the Baker-Figgis δ-isomer of the Al_{13}-Keggin structure as its structural motif. The PDF analyses reported in this paper show a perfect match between the real space structures of the experimental and the proposed Al_{13}-Keggin structure for ferrihydrite. However, some authors have reported that, although the short-range structure is well reproduced, there is a lack of agreement in the diffraction pattern, with one diffraction peak absent, indicative of a different long-range

ordering (Rancourt and Meunier, 2008). This result highlights the complementarity of short-range real-space studies with long-range diffraction pattern analyses.

This complementarity is highlighted in the Chapter 5 of this thesis, devoted to the study of the structure of schwertmannite, a nanocrystalline iron oxyhydroxysulfate. While the presence of sulfate cannot be discerned from PDF measurements due to the dominant signal of Fe-Fe and Fe-O correlations, variations in sulfate concentration in the samples are responsible of strong variations in the intensity of the (101) reflection in the X-ray diffraction pattern of schwertmannite. This result indicates that, although schwertmannite has a small coherent domain size, there is an underlying long range order in the structure.

The use of PDF analysis (presented in Chapter 2), in combination with other techniques, has revealed thus as a powerful technique to the study of mineral nanoparticles, with diffraction patterns dominated by diffuse scattering that are very difficult to analyze by reciprocal-space methods.

REFERENCES

Ackerman, W.C., Smith, D.M., Huling, J.C., Kim, Y.W., Bailey, J.K., and Brinker, C.J. (1993) Gas vapor adsorption in imogolite - A microporous tubular aluminosilicate. Langmuir, 9(4), 1051-1057.

Alvarez-Ramirez, F. (2007) Ab initio simulation of the structural and electronic properties of aluminosilicate and aluminogermanate natotubes with imogolite-like structure. Physical Review B, 76(12).

Amweg, E.L., Stuart, D.L., and Weston, D.P. (2003) Comparative bioavailability of selenium to aquatic organisms after biological treatment of agricultural drainage water. Aquatic Toxicology, 63(1), 13-25.

Arai, Y., McBeath, M., Bargar, J.R., Joye, J., and Davis, J.A. (2006) Uranyl adsorption and surface speciation at the imogolite-water interface: Self-consistent spectroscopic and surface complexation models. Geochimica et Cosmochimica Acta, 70(10), 2492-2509.

Balistrieri, L.S., and Chao, T.T. (1987) Selenium Adsorption by Goethite. Soil Science Society of America Journal, 51(5), 1145-1151.

Barham, R.J. (1997) Schwertmannite: A unique mineral, contains a replaceable ligand, transforms to jarosites, hematites, and/or basic iron sulfate. Journal of Materials Research, 12(10), 2751-2758.

Bickmore, B.R., Tadanier, C.J., Rosso, K.M., Monn, W.D., and Eggett, D.L. (2004) Bond-Valence methods for pK(a) prediction: critical reanalysis and a new approach. Geochimica et Cosmochimica Acta, 68(9), 2025-2042.

Bigham, J.M., Carlson, L., and Murad, E. (1994) Schwertmannite, a new iron oxyhydroxysulphate from Pyhasalmi, Finland, and other localities. Mineralogical Magazine, 58(393), 641-648.

Byers, H.G., Miller, J.T., Williams, K.T., and Lakin, H.W. (1938) Selenium occurrence in certain soils in the United States with a discussion of related topics. Third Report U.S.D.A. Tech. Bul. 601., US.

Chorover, J., and Sposito, G. (1995) Surface-charge characteristics of kaolinitic tropical soils. Geochimica et Cosmochimica Acta, 59(5), 875-884.

Combs, G.F., Garbisu, C., Yee, B.C., Yee, A., Carlson, D.E., Smith, N.R., Magyarosy, A.C., Leighton, T., and Buchanan, B.B. (1996) Bioavailability of selenium accumulated by selenite-reducing bacteria. Biological Trace Element Research, 52(3), 209-225.

Cradwick, P.D., Wada, K., Russell, J.D., Yoshinag.N, Masson, C.R., and Farmer, V.C. (1972) Imogolite, a hydrated aluminum silicate of tubular structure. Nature-Physical Science, 240(104), 187-&.

Creton, B., Bougeard, D., Smirnov, K.S., Guilment, J., and Poncelet, O. (2008a) Molecular dynamics study of hydrated imogolite - 2. Structure and dynamics of confined water. Physical Chemistry Chemical Physics, 10(32), 4879-4888.

-. (2008b) Molecular dynamics study of hydrated imogolite. 1. Vibrational dynamics of the nanotube. Journal of Physical Chemistry C, 112(27), 10013-10020.

Dahlgren, R.A., and Ugolini, F.C. (1989) Formation and stability of imogolite in a tephritic spodosol, Cascade Range, Washington, USA. Geochimica et Cosmochimica Acta, 53(8), 1897-1904.

-. (1991) Distribution and characterization of short-range-order minerals in spodosols from the Washington cascades. Geoderma, 48(3-4), 391-413.

Davidson, D.F., and Powers, H.A. (1959) Selenium content of some volcanic rocks from Western United States and Hawaiian Islands. Bulletin of the Geological Survey of U.S., 1084-C, 69-81.

Dhillon, S.K., and Dhillon, K.S. (2000) Selenium adsorption in soils as influenced by different anions. Journal of Plant Nutrition and Soil Science-Zeitschrift Fur Pflanzenernahrung Und Bodenkunde, 163(6), 577-582.

Duc, M., Lefevre, G., Fedoroff, M., Jeanjean, J., Rouchaud, J.C., Monteil-Rivera, F., Dumonceau, J., and Milonjic, S. (2003) Sorption of selenium anionic species on apatites and iron oxides from aqueous solutions. Journal of Environmental Radioactivity, 70(1-2), 61-72.

Farmer, V.C., Adams, M.J., Fraser, A.R., and Palmieri, F. (1983) Synthetic imogolite - Properties, synthesis and possible applications. Clay Minerals, 18(4), 459-472.

Gehin, A., Greneche, J.M., Tournassat, C., Brendle, J., Rancourt, D.G., and Charlet, L. (2007) Reversible surface-sorption-induced electron-transfer oxidation of Fe(II) at reactive sites on a synthetic clay mineral. Geochimica et Cosmochimica Acta, 71(4), 863-876.

Guimaraes, L., Enyashin, A.N., Frenzel, J., Heine, T., Duarte, H.A., and Seifert, G. (2007) Imogolite nanotubes: Stability, electronic, and mechanical properties. Acs Nano, 1(4), 362-368.

Gustafsson, J.P. (2001) The surface chemistry of imogolite. Clays and Clay Minerals, 49(1), 73-80.

Hansmann, D.D., and Anderson, M.A. (1985) Using Electrophoresis in Modeling Sulfate, Selenite, and Phosphate Adsorption onto Goethite. Environmental Science & Technology, 19(6), 544-551.

Harsh, J.B., Traina, S.J., Boyle, J., and Yang, Y. (1992) Adsorption of cations on imogolite and their effect on surface-charge characteristics. Clays and Clay Minerals, 40(6), 700-706.

Hiemstra, T., and VanRiemsdijk, W.H. (1996) A surface structural approach to ion adsorption: The charge distribution (CD) model. Journal of Colloid and Interface Science, 179(2), 488-508.

Hiemstra, T., Venema, P., and VanRiemsdijk, W.H. (1996) Intrinsic proton affinity of reactive surface groups of metal (hydr)oxides: The bond valence principle. Journal of Colloid and Interface Science, 184(2), 680-692.

Ihnat, M. (1989) Occurence and distribution of Selenium. 354 p. CRC Press, Boca Raton, Florida.

Johnson, C.C., Ge, X., Green, K.A., and Liu, X. (2000) Selenium distribution in the local environment of selected villages of the Keshan Disease belt, Zhangjiakou

District, Hebei Province, People's Republic of China. Applied Geochemistry, 15(3), 385-401.

Karube, J., Nakaishi, K., Sugimoto, H., and Fujihira, M. (1992) Electrophoretic behavior of imogolite under alkaline conditions. Clays and Clay Minerals, 40(6), 625-628.

Lakin, H.W. (1972) Selenium Accumulation in Soils and Its Absorption by Plants and Animals. Geological Society of America Bulletin, 83(1), 181-189.

Lanson, B. (1997) Decomposition of experimental x-ray diffraction patterns (profile fitting): A convenient way to study clay minerals. Clays and Clay Minerals, 45(2), 132-146.

Lemly, A.D. (1993) Guidelines for evaluating selenium data from aquatic monitoring and assessment studies. Environmental Monitoring and Assessment, 28(1), 83-100.

Lennie, A.R., Redfern, S.A.T., Schofield, P.F., and Vaughan, D.J. (1995) Synthesis and Rietveld crystal structure refinement of mackinawite, tetragonal FeS. Mineralogical Magazine, 59(397), 677-683.

Levander, O.A., and Burk, R.F. (2006) Update of human dietary standards for selenium. Selenium. Its Molecular Biology and Role in Human Health, 1, p. 399-410. Springer US, New York.

Maier, K.J., Foe, C.G., and Knight, A.W. (1993) Comparative toxicity of selenate, selenite, seleno-dl-methionine and seleno-dl-cystine to *Daphnia-Magna*. Environmental Toxicology and Chemistry, 12(4), 755-763.

Manceau, A., and Gates, W.P. (1997) Surface structural model for ferrihydrite. Clays and Clay Minerals, 45(3), 448-460.

Michel, F.M., Antao, S.M., Chupas, P.J., Lee, P.L., Parise, J.B., and Schoonen, M.A.A. (2005) Short- to medium-range atomic order and crystallite size of the initial FeS precipitate from pair distribution function analysis. Chemistry of Materials, 17(25), 6246-6255.

Michel, F.M., Ehm, L., Antao, S.M., Lee, P.L., Chupas, P.J., Liu, G., Strongin, D.R., Schoonen, M.A.A., Phillips, B.L., and Parise, J.B. (2007a) The structure of ferrihydrite, a nanocrystalline material. Science, 316(5832), 1726-1729.

Michel, F.M., Ehm, L., Liu, G., Han, W.Q., Antao, S.M., Chupas, P.J., Lee, P.L., Knorr, K., Eulert, H., Kim, J., Grey, C.P., Celestian, A.J., Gillow, J., Schoonen, M.A.A., Strongin, D.R., and Parise, J.B. (2007b) Similarities in 2-and 6-line

ferrihydrite based on pair distribution function analysis of X-ray total scattering. Chemistry of Materials, 19(6), 1489-1496.

Mukherjee, S., Bartlow, V.A., and Nair, S. (2005) Phenomenology of the growth of single-walled aluminosilicate and aluminogermanate nanotubes of precise dimensions. Chemistry of Materials, 17(20), 4900-4909.

Nakamaru, Y., Tagami, K., and Uchida, S. (2005) Distribution coefficient of selenium in Japanese agricultural soils. Chemosphere, 58(10), 1347-1354.

Neal, R.H., Sposito, G., Holtzclaw, K.M., and Traina, S.J. (1987a) Selenite Adsorption on Alluvial Soils .1. Soil Composition and Ph Effects. Soil Science Society of America Journal, 51(5), 1161-1165.

-. (1987b) Selenite Adsorption on Alluvial Soils .2. Solution Composition Effects. Soil Science Society of America Journal, 51(5), 1165-1169.

Rancourt, D.G., and Meunier, J.F. (2008) Constraints on structural models of ferrihydrite as a nanocrystalline material. American Mineralogist, 93(8-9), 1412-1417.

Rayman, M.P. (2000) The importance of selenium to human health. Lancet, 356(9225), 233-241.

Reeder, R.J., Schoonen, M.A.A., and Lanzirotti, A. (2006) Metal speciation and its role in bioaccessibility and bioavailability. In N. Sahai, M.A.A. Schoonen, and H.C.W. Skinner, Eds. The emergent field of medical mineralogy and geochemistry, p. 59-113. Mineralogical Society of America and the Geochemical Society, USA.

Reilly, C. (1997) Selenium in food and health. 360 p. Blackie Academic & Professional, London.

Rietveld, H.M. (1969) A profile refinement method for nuclear and magnetic structures. Journal of Applied Crystallography, 2, 65-&.

Rosenqvist, J., Persson, P., and Sjoberg, S. (2002) Protonation and charging of nanosized gibbsite (alpha-Al(OH)(3)) particles in aqueous suspension. Langmuir, 18(12), 4598-4604.

Ruby, M.V., Davis, A., Schoof, R., Eberle, S., and Sellstone, C.M. (1996) Estimation of lead and arsenic bioavailability using a physiologically based extraction test. Environmental Science & Technology, 30(2), 422-430.

Ruby, M.V., Schoof, R., Brattin, W., Goldade, M., Post, G., Harnois, M., Mosby, D.E., Casteel, S.W., Berti, W., Carpenter, M., Edwards, D., Cragin, D., and Chappell,

W. (1999) Advances in evaluating the oral bioavailability of inorganics in soil for use in human health risk assessment. Environmental Science & Technology, 33(21), 3697-3705.

Schindler, P.W., and Stumm, W. (1987) Aquatic Surface Chemistry, Chemical Processes at the Particle-Water Interface. Ed. J. Wiley and Sons, New York.

Schlekat, C.E., Dowdle, P.R., Lee, B.G., Luoma, S.N., and Oremland, R.S. (2000) Bioavailability of particle-associated Se to the bivalve *Potamocorbula amurensis*. Environmental Science & Technology, 34(21), 4504-4510.

Schwarz, K., and Foltz, C.M. (1957) Selenium as an integral part of Factor 3 against dietary necrotic liver degeneration. Soc, 79, 3292-3293.

Sirichakwal, P.P., Puwastien, P., Polngam, J., and Kongkachuichai, R. (2005) Selenium content of Thai foods. Journal of Food Composition and Analysis, 18(1), 47-59.

Sposito, G. (2004) The surface chemistry of natural particles. 242 p. Oxford University Press, New York.

Stone, R. (2009) A Medical Mystery in Middle China. Science, 324(5933), 1378-1381.

Su, C.M., and Harsh, J.B. (1993) The electrophoretic mobility of imogolite and allophane in the presence of inorganic anions and citrate. Clays and Clay Minerals, 41(4), 461-471.

Tsuchida, H., Ooi, S., Nakaishi, K., and Adachi, Y. (2004) Effects of pH and ionic strength on electrokinetic properties of imogolite. 3rd International Conference on Interfaces Against Pollutions, p. 131-134, Julich, GERMANY.

Ugolini, F.C., and Dahlgren, R.A. (1991) Weathering environments and occurrence of imogolite and allophane in selected andisols and spodosols. Soil Science Society of America Journal, 55(4), 1166-1171.

Vandergaast, S.J., Wada, K., Wada, S.I., and Kakuto, Y. (1985) Small-angle X-ray powder diffraction, morphology and structure of allophane and imogolite. Clays and Clay Minerals, 33(3), 237-243.

Wada, K. (1989) Allophane and imogolite. In J.B. Dixon, and S.B. Weed, Eds. Minerals in soil environments, p. 1051-1087.

Wang, M.C., and Chen, H.M. (2003) Forms and distribution of selenium at different depths and among particle size fractions of three Taiwan soils. Chemosphere, 52(3), 585-593.

Wang, Z.J., and Gao, Y.X. (2001) Biogeochemical cycling of selenium in Chinese environments. Applied Geochemistry, 16(11-12), 1345-1351.

Warren, B.E. (1969) X-ray diffraction. Addison-Wesley, Reading.

Wolthers, M., Van der Gaast, S.J., and Rickard, D. (2003) The structure of disordered mackinawite. American Mineralogist, 88(11-12), 2007-2015.

Zang, J., Konduri, S., Nair, S., and Sholl, D.S. (2009) Self-Diffusion of Water and Simple Alcohols in Single-Walled Aluminosilicate Nanotubes. Acs Nano, 3(6), 1548-1556.

Zhang, E.S., Wang, H.L., Yan, X.X., and Zhang, L.D. (2005) Comparison of short-term toxicity between Nano-Se and selenite in mice. Life Sciences, 76(10), 1099-1109.

Chapter 2

Experimental and Theoretical Methods

This chapter briefly presents some of the experimental and theoretical methods used in this work, obviating explanations of other widely used techniques as transmission electron microscopy, infrared spectroscopy or wet chemical methods that will be explained in the chapters where their use is presented. The experimental techniques presented here include X-ray absorption spectroscopy and X-ray Pair Distribution Function. Key ideas behind *ab-initio* DFT calculations and Molecular Dynamics simulations will be presented too. The purpose of this chapter is to provide some basic information about the methods to the reader not used to them, allowing him to understand the results obtained within the thesis.

2.1.- Pair Distribution Function technique

The PDF is a diffraction technique which involves the use of (1) high energy radiation (high energy X-rays, electrons or hot neutrons) and (2) a real-space analysis of the data mediated by a Fourier transformation of the interference function or *S(Q)*. The theoretical basis of the PDF technique will be explained here in terms of neutron and X-ray scattering, the two types of radiation used in this thesis.

The diffracted amplitude of neutrons or X-rays after interacting with a sample can be expressed in terms of the like this:

$$A(\vec{Q}) = \frac{1}{\langle b \rangle} \sum_{n}^{N} b_n e^{i\vec{Q}_n(t)\vec{x}_n} \qquad (2.1)$$

where $\vec{Q}$, a vector in the reciprocal space, is the scattering or diffraction vector, or the momentum transfer, $\vec{x}_n$ is the atomic position, b_n is the scattering amplitude of the atom n and $\vec{Q}$ is defined as:

$$\vec{Q} = \vec{Q}_i - \vec{Q}_f \tag{2.2}$$

$$\left|\vec{Q}\right| = \frac{4\pi \sin(\theta)}{\lambda} \tag{2.3}$$

being $\vec{Q}_i$ and $\vec{Q}_f$ the momenta of the incident and scattered radiation respectively, λ the wavelength of the incident and scattered radiation (we consider only elastic processes) and θ is the half the angle between $\vec{Q}_i$ and $\vec{Q}_f$.

In equation 2.1, $\langle ... \rangle$ represents a compositional average:

$$\langle b \rangle = \frac{1}{N}\sum_n b_n = \sum_\alpha c_\alpha b_\alpha \tag{2.4}$$

being c_α the concentration of element α and N the number of atoms in the sample. Equation 2.1 relates the positions of the atoms in a sample with the scattered amplitude through a Fourier transformation. The inconvenient to solve crystallographic problems using this equation is that the scattered amplitude $A(\vec{Q})$ is not available experimentally. Instead, we can measure the intensity, or what is the same, the square of the magnitude of $A(\vec{Q})$:

$$\begin{aligned} I_N(\vec{Q}) = A(\vec{Q})A^*(\vec{Q}) = \iint \rho(\vec{r})\rho(\vec{x}+\vec{r})\exp(-2\pi i\vec{Q}\vec{x})dv_x dv_u = \\ = \int P(\vec{x})\exp\exp(-2\pi i\vec{Q}\vec{x})dv_x \end{aligned} \tag{2.5}$$

where:

$$P(\vec{x}) = \int \rho(\vec{r})\rho(\vec{x}+\vec{r})dv_x \tag{2.6}$$

is the electron density autocorrelation function, or the Patterson function. If we normalize the function $I_N(\vec{Q})$ by the number of atoms in the system N, and by the square of the average atomic form factor or scattering amplitude (or scattering length), we have the definition of the *interference function*:

$$\Gamma(\vec{Q}) = \frac{I_N(\vec{Q})}{N\langle b \rangle^2} = \frac{1}{N}\int P(\vec{x})\exp(-2\pi i\vec{Q}\vec{x})dv_x \equiv S(\vec{Q}) \tag{2.7}$$

In isotropic or randomly oriented systems as powders or nanoparticles, the so-called 'isotropic approximation' can be made (Cuello, 2007), yielding the 'Debye equation for diffraction' (Debye, 1915):

$$I_N(Q) \propto S(Q) = 1 + \frac{1}{N}\sum_{i,j\neq i}^{N} b_i b_j \frac{\sin(Qr_{ij})}{Qr_{ij}} \tag{2.8}$$

Equation 2.8 links the observed scattered intensity, I_N, with a sum over all the pairs of atoms in the sample, r_{ij}. *S(Q)* is called the 'static structure factor', being *Q* the norm of the scattering vector. A real-space analysis of this intensity distribution in series of sinus functions can be made through a Fourier transformation:

$$g(r) - 1 = \frac{1}{2\pi^2 r\rho}\int_0^\infty Q[S(Q) - 1]\sin(Qr)dr \qquad (2.9)$$

The function *g(r)* is called the Pair Distribution Function (PDF). It is proportional to the probability of finding two atoms separated by a distance of *r*. In contrast with the partial-PDF obtained with other spectroscopic methods such as Extended X-ray Absorption Fine Structure (EXAFS), the PDF function obtained from diffraction experiments is not chemically selective, thus giving a structural description of the local order around all the atoms in the structure.

More details about this technique can be found in (Egami and Billinge, 2003).

2.2.- X-ray Absorption Spectroscopy

X-ray absorption spectroscopy (XAS) is a probe of the local structure around selected atom species in solids, liquids and molecular gases (Kelly et al., 2008; Teo, 1986). For atoms in a condensed system, the observed X-ray absorption spectrum is not a smooth function of energy but oscillates for several hundreds eV above the absorption edge. The details of these oscillations, called EXAFS (Extended X-ray Absorption Fine Structure), depend strongly on the local atomic environment of the absorbing atom, with a few nearest neighboring atoms accounting for essentially all the observed variations in the absorption.

X-ray absorption spectroscopy is a useful complement to X-ray diffraction which provides accurate long-range information about the structure of crystalline materials. In a typical XAS experiment, performed in transmission geometry, the intensity *I(x, E)* of transmitted X-rays through a sample of thickness *x* is measured as a function of energy. The loss of X-ray intensity is given by the exponential Lambert-Beer attenuation law:

$$\frac{I(x,E)}{I(0,E)} = e^{-\mu(E)x} \qquad (2.15)$$

where $\mu(E)$ is the linear absorption coefficient. As well as depending on the energy of the incident beam, μ also depends on the composition of the irradiated sample. The

absorption coefficient μ(E) is well approximated by a sum of the absorption coefficients of individual atoms, proportional to the x-ray absorption cross section $\sigma(E)$.

In the X-ray region (below 50 keV approximately), the cross section for the interaction of radiation with matter is dominated by photo-electric excitation processes which manifest themselves as sharp rises in the absorption, usually termed edges (i.e. K, L1, L2 and L3), when the incident photon has an energy equal to the binding energy of a core-level electron (*i.e.* 1s, 2s, $2p_{1/2}$ and $2p_{3/2}$). Clear oscillations of the absorption coefficient are observed in a wide energy region above the edge (of about 1000 eV). The absence of such modulations in low density systems and gases points to a strict relationship between EXAFS oscillations and the presence of neighboring atoms.

EXAFS and its local nature are best understood in terms of wave-behavior of the photo-electron created in the absorption process. The wave associated with the photo-excited electron can be scattered by neighboring atoms as shown in Figure 2.1 and returns to the photo-absorber. The interference between the outgoing and backscattered components leads to modulations of the final state wave-function as a function of the electron energy. This in turn modulates the absorption coefficient $\mu(E)$ producing the EXAFS oscillations.

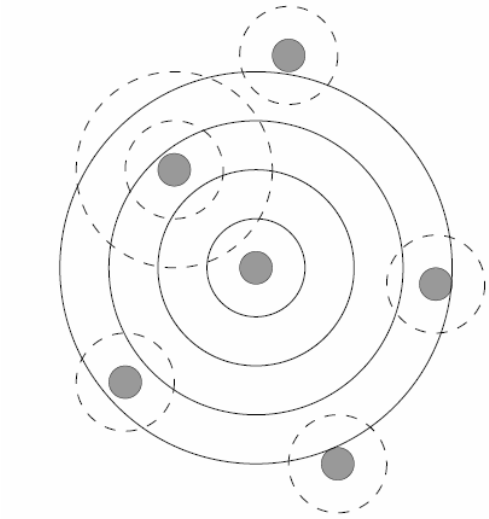


Figure 2.1. *Schematic view of the radial component of the outgoing (continuous line) and backscattered parts (dashed lines) of the photo-electron wave in a condensed system. The interference between these two components leads to modulations of the final state.*

The X-ray absorption spectrum is traditionally divided into two regimes: X-ray Absorption Near Edge Structure (XANES) and Extended X-ray Absorption Fine

Structure (EXAFS). Though the two regions overlap and have the same physical origin, this distinction is convenient for the interpretation:

- XANES region: (within about 50-100 eV above the absorption edge) the photoelectron is strongly scattered by the atoms surrounding the photo-absorber and the amplitude of the multiple scattering is important. The shape of the XAS spectra in this region is strongly sensitive to the formal oxidation state and coordination chemistry of the absorbing atom;
- EXAFS region: (from about 80 eV above the edge) the photo-electron has sufficient energy for treating the multiple scattering in terms of distinct two-, three-, …, *n*-body contributions. Nevertheless, the two-body contributions are generally the dominant terms.

The EXAFS function is defined as:

$$\chi(k) = \frac{\mu(k) - \mu_0(k)}{\mu_0(k)} \tag{2.16}$$

where $k = \sqrt{\frac{2m}{\hbar^2}(E - E_0)}$ is the wave-vector is the wave-vector of the photo-electron (E_0 is the core binding energy) and μ_0 is a smooth, atomic-like, background absorption of an “embedded atom", in the ideal absence of neighboring scatterers.

In the following we report the simple analytic form of the EXAFS signal $\chi(k)$ obtained from the Diffusion Theory (Rehr and Albers, 2000). It assumes both the approximation of spherical waves for the wave-function associated to the outgoing and backscattered photo-electrons and the single scattering approximation (meaning that it considers only two-body contributions). Even though this formulation assumes the rude single scattering approximation to the problem, it is useful at present because it provides an easy general comprehension of XAS. The final analytic form for equation 2.16 is expressed as:

$$\chi(k) = \sum_j A(r_j, k) \sin\left[2kr_j + \Phi_j(k, r)\right] e^{-2\sigma_j^2 k^2} e^{-2r_j/\lambda_j(k)} \tag{2.17}$$

where

- The sum over *j* involves all the coordination shells around the photo-absorber atom.

- The amplitude factor $A(r_j, k)$ is proportional to N_j , *i.e.*, the number of atoms in the *j*-th shell and it is inversely proportional to $k \cdot r_j^2$ (r_j is the distance between the photo-absorber site and the atoms in the *j* shell).

- The $e^{-2\sigma_j^2 k^2}$ term is similar to the diffraction Debye-Waller factor and it is related to the thermal disorder, with the difference that in EXAFS σ_j^2 is the mean-square relative displacement (MSRD) of *j* atom (or shell) with respect to the absorber atom:

$$\sigma_{a-j}{}^2 = \sigma_a{}^2 + \sigma_j{}^2 - 2\sigma_a\sigma_j\rho\,,$$

being the *a* index a reference of the photo-absorber atom, and ρ a correlation factor with values $-1 \leq \rho \leq 1$.

- The $e^{-2r_j/\lambda_j(k)}$ term describes the inelastic processes during the propagation of the photo-electron and $\lambda_j(k)$ is the limited mean-free-path of the electron.

- $\Phi_j(k, r)$ is the phase shift due to photo-electron diffusion from the photo-absorber site and from the neighboring atoms.

2.3.- Simulations

In this section we shortly describe the principle of the *ab-initio* Density Functional Theory (DFT) approximation adopted by the Vienna Ab-initio Simulation Package (VASP) (Kresse and Hafner, 1993; Kresse and Hafner, 1994) and DMol3 (Delley, 2000), which were the codes employed in this work. We will give some basics about the Molecular Dynamics and Monte Carlo simulations (Frenkel and Smit, 2002) performed with the LAMMPS (Plimpton, 1995) and Sorption (Accelrys Inc.) codes, respectively.

2.3.1.- *Ab-initio* DFT calculations

In physics and chemistry, a calculation is said to be *ab-initio*, or from first principles, if it starts directly at the level of established laws of physics. Nevertheless, some approximations are needed to make achievable such calculations as discussed below. This method provides the main tools for the understanding of the properties of matter, in all its possible states, by solving the fundamental equations for electrons.

In quantum mechanics a system is described by a wave function Ψ which is determined by the solution of the Schrödinger equation describing the nuclear and electronic motions:

$$\hat{\mathrm{H}}(r,R)\Psi(r,R) = (-\sum_{i-1}^{N_e}\frac{\hbar^2\nabla_i^{\,2}}{2m_e} - \sum_{I-1}^{N_i}\frac{\hbar^2\nabla_I^{\,2}}{2M_I} + \frac{1}{2}\sum_{I\neq I'}\frac{ZZ'e^2}{|R_I - R_{I'}|} -) +$$
$$+ \frac{1}{2}\sum_{i\neq j}\frac{e^2}{|r_i - r_j|} - \sum_{i,I}\frac{Z_I e^2}{|r_i - R_I|})\Psi(r,R) = \qquad (2.18)$$
$$= (\hat{T}_e + \hat{T}_i + \hat{V}_{i-i} + \hat{V}_{e-e} + \hat{V}_{i-e})\Psi(r,R) = E\Psi(r,R)$$

where r and R correspond to the positions of the N_e electrons and N_i ions, $\hat{T}_e$ and $\hat{T}_i$ are the electronic and nuclear kinetic energies and $\hat{V}_{i-i}$, $\hat{V}_{e-e}$ and $\hat{V}_{i-e}$ are the ion-ion, electron-electron and ion-electron coulombic interactions, respectively.

Due to the impossibility of solving exactly this equation when dealing with many body particles some approximations are needed. In the following we briefly describe the approximations adopted during this work:

- Adiabatic (or Born-Oppenheimer) approximation: as the general electronic velocities are much larger than the nuclear ones, hence, the nuclear and electronic motions can be decoupled and treated separately. In particular, the Schrödinger equation for the system can be decomposed as:

  $$\Psi(r,R) = \psi_R(r)\Phi(R) \qquad (2.19)$$

  where the electronic wave-function, $\psi_R(r)$, is only parametrically depending on the nuclear position variable R. Hence, each electronic structure calculation is performed for a fixed nuclear configuration.

- DFT: within this approximation the electronic properties of a system of many interacting particles can be viewed as a functional of the ground state density $\rho(r)$. The modern formulation of density functional theory originated in a famous work written in 1964, where Hohenberg and Kohn provided the proofs for the existence of such a functional (Hohenberg and Kohn, 1964).

  Kohn-Sham equations

  Subsequently, Kohn and Sham (Kohn and Sham, 1965), starting from the variational principle established by Hohenberg and Kohn, proposed to replace the original many-body problem by an “auxiliary" independent particle problem. The *ansatz* of Kohn and Sham assumes that the ground state density of the original

interacting system is equal to that of some chosen non-interacting system. This leads to independent particle equations that are exactly solvable with the many-body terms incorporated into an exchange-correlation functional of the density. The Kohn-Sham (KS) equations for the auxiliary system of N non-interacting electrons are:

$$\left\{-\frac{1}{2}\nabla^2 + v_{eff}(r)\right\}\psi_i = \varepsilon_i \psi_i \tag{2.20}$$

and

$$\rho(r) = \sum_{i=1}^{N} |\psi i(r)|^2 \tag{2.21}$$

where $\rho(r)$ is the electronic density of the system, $v_{\text{eff}}(r)$ is an effective potential resulting from the external potential, the Hartree electronic interaction and the exchange and correlation potential $E_{xc}[\rho(r)]$ (which is discussed below); ε_i (multipliers of the KS equations) are related, in first approximation, to the energy levels occupied by the interacting electrons. The procedure to obtain the total energy of the system is completely autoconsistent. The solution of equation 2.20 produces the wave functions ψ_i and then the electronic density from equation 2.21 which is used to define the effective potential in equation 2.20. This process is repeated until the tolerance imposed on the difference between the input and the output density is reached.

Exchange and correlation energy

The Local Density Approximation (LDA) holds when $\rho(r)$ is a smooth function of r. In this case, the exchange and correlation functional $E_{xc}[\rho(r)]$ is approximated by an integral over space of the exchange and correlation energy which is assumed to be the same as in a homogeneous electron gas of $\rho(r)$ density. On the other hand, for very inhomogeneus systems the Generalized-Gradient Approximation (GGA), which depends on the density and on its gradient, is preferably used. In this work we have used the GGA approximation.

- Pseudopotentials: the physical properties of solids are dependent on the valence electrons to a much greater degree than on the tightly bound core electrons. This approximation uses this fact to replace the complicated effects of

the motion of the core electrons of an atom or ion and its nucleus with an effective potential, or pseudopotential. This fictitious potential acts in the internal region of the atoms, reproducing the screening effect of the core electrons within the core region. The “all-electron", *i.e.*, the exact wave-functions, are replaced by pseudo-wavefunctions. The pseudopotential is then generated by fulfilling the following requirements:

- The corresponding pseudo-wavefunctions and the all-electron agree beyond a chosen core radius R_c.

- Pseudo- and all-electron eigenvalues agree for a chosen atomic reference configurations meaning that the pseudopotential must describe the valence properties in a different environment including atoms, ions, molecules and condensed matter (transferability).

- The logarithmic derivatives of the pseudo and the all-electron wavefunctions agree at R_c.

- The integrated charge inside R_c for each wavefunction agrees meaning that the pseudo- and the all-electron wavefunctions have the same norm (norm-conserving pseudopotential).

- Basis set expansion: in order to solve the 2.20 and 2.21 KS equations it is necessary to reduce the problem to a finite number of variables. This is done by expanding the unknown $\psi_i(r)$ wavefunctions in terms of known basis function. The most common basis function sets are plane waves and localized atomic orbitals. In this work we have used two different codes, each of one using a different type of functions: VASP uses plane waves (Kresse and Hafner, 1993; Kresse and Hafner, 1994) and DMol3 uses numerical orbitals (Delley, 1990; Delley, 2000) that have been obtained from calculations performed on isolated atoms.

2.3.2.- Classical Molecular Dynamics and Monte Carlo simulations

In Molecular Dynamics and Monte Carlo simulations, macroscopic properties of a system are studied through microscopic simulations. The connection between microscopic simulations and macroscopic properties is made via statistical mechanics which provides the rigorous mathematical expressions that relate macroscopic properties to the distribution and motion of the atoms and molecules of the *N*-body

system. Some definitions of concepts of statistical mechanics are given here (Frenkel and Smit, 2002):

The thermodynamic state of a system is usually defined by a small set of parameters, for example, the temperature, T, the pressure, P, and the number of particles, N. Other thermodynamic properties may be derived from the equations of state and other fundamental thermodynamic equations.

The mechanical or microscopic state of a system is defined by the atomic positions, q, and momenta, p. These can also be considered as coordinates in a multidimensional space called phase space. For a system of N particles, this space has $6N$ dimensions. A single point in phase space, denoted by G, describes the state of the system.

An ensemble is a collection of points in phase space satisfying the conditions of a particular thermodynamic state.

In a molecular dynamics simulation a sequence of points in phase space is generated as a function of time, in a deterministic manner. These points belong to the same ensemble, and they correspond to the different conformations of the system and their respective momenta. In a Monte Carlo simulation the sequence of points in phase space are generated in a stochastic way.

In this work we have used two different ensembles:

- *Canonical Ensemble (NVT)*: It is a collection of all systems whose thermodynamic state is characterized by a fixed number of atoms, N, a fixed volume, V, and a fixed temperature, T.
- *Isobaric-Isothermal Ensemble (NPT)*: This ensemble is characterized by a fixed number of atoms, N, a fixed pressure, P, and a fixed temperature, T.

In order to connect the macroscopic system to the microscopic system, time-independent statistical averages are often introduced, which rely on the Ergodic hypothesis:

$$\text{MD:} \qquad \langle A \rangle_{ensemble} = \langle A \rangle_{time} \tag{2.22}$$

$$\text{MC:} \qquad \langle A \rangle_{ensemble} = \langle A \rangle_{configurations} \tag{2.23}$$

This hypothesis states that if one allows the system to evolve in time indefinitely (MD) or to generate a big enough number of microscopic configurations, the system will eventually pass through all possible states. One goal, therefore, of a MD and MC simulation is to generate enough representative conformations such that this equality is satisfied.

2.3.2.1.- Molecular Dynamics method

The molecular dynamics simulation method is based on Newton's second law or the equation of motion, $\boldsymbol{F} = m \cdot \boldsymbol{a}$, where $\boldsymbol{F}$ is the force exerted on the particle, m is its mass and $\boldsymbol{a}$ is its acceleration. From the knowledge of the force acting on each atom, it is possible to determine its acceleration in the system. Integration of the equations of motion then yields a trajectory that describes the positions, velocities and accelerations of the particles as they vary with time. From this trajectory, the average values of properties can be determined. Therefore, to calculate a trajectory, one only needs the initial positions of the atoms, an initial distribution of velocities and the acceleration, which is determined by the gradient of the potential energy function.

The equations of motion are deterministic, *i.e.*, the positions and the velocities at time zero determine the positions and velocities at all other times, *t*. The initial positions can be obtained from experimental structures, such as the X-ray crystal structure. In our case, all the atoms of the imogolite and gibbsite structures are allowed to move. We have chosen to use a flexible system because both systems have surfaces populated by OH functional groups, whose positions and orientations determine their ability to form H-bonds with water molecules. Furthermore, the force-field (set of parameters determining the potential) used in the simulations, CLAYFF (Cygan et al., 2004), has been calibrated using the gibbsite structure (between others) and thus it reproduces well the crystal structure of our systems.

The initial distribution of velocities have been determined from a random distribution with the magnitudes conforming to the required temperature and corrected so there is no overall momentum, *i.e.*:

$$\vec{P} = \sum_{i=1}^{N} m_i \vec{v}_i = 0 \tag{2.24}$$

The velocities, $\boldsymbol{v_i}$, are have been chosen randomly from a Maxwell-Boltzmann distribution at room temperature, which gives the probability that an atom i has a velocity $\boldsymbol{v_x}$ in the x direction at a temperature T:

$$p(v_{ix}) = \left(\frac{m_i}{2\pi k_B T} \right)^{1/2} \exp\left[-\frac{1}{2} \frac{m_i v_{ix}^2}{k_B T} \right] \tag{2.25}$$

The temperature can be calculated from the velocities using the relation:

$$T = \frac{1}{(3N)} \sum_{i=1}^{N} \frac{|p_i|}{2m_i} \tag{2.26}$$

where N is the number of atoms in the system.

Integration Algorithms

The potential energy is a function of the atomic positions (3N) of all the atoms in the system. Due to the complicated nature of this function, there is no analytical solution to the equations of motion, they must be solved numerically. We have chosen to use the Verlet algorithm as implemented in the code LAMMPS (Plimpton, 1995), the MD code used in our simulations.

All the integration algorithms assume the positions, velocities and accelerations can be approximated by a Taylor series expansion:

$$\begin{aligned} r(t+\delta t) &= r(t) + v(t)\delta t + \frac{1}{2}a(t)\delta t^2 + \ldots \\ v(t+\delta t) &= v(t) + a(t)\delta t + \frac{1}{2}b(t)\delta t^2 + \ldots \\ a(t+\delta t) &= a(t) + b(t)\delta t + \ldots \end{aligned} \tag{2.27}$$

where r is the position, v is the velocity (the first derivative with respect to time), a is the acceleration (the second derivative with respect to time), etc. To derive the Verlet algorithm one can write:

$$\begin{aligned} r(t+\delta t) &= r(t) + v(t)\delta t + \frac{1}{2}a(t)\delta t^2 \\ r(t-\delta t) &= r(t) - v(t)\delta t + \frac{1}{2}a(t)\delta t^2 \end{aligned} \tag{2.28}$$

Summing these two equations, one obtains:

$$r(t+\delta t) = 2r(t) - r(t-\delta t) + a(t)\delta t^2 \tag{2.29}$$

The Verlet algorithm uses positions and accelerations at time t and the positions from time t-δt to calculate new positions at time t+δt.

Time averages

In order to extract thermodynamic information from the microscopic trajectories generated using the MD method, the Ergodic hypothesis is applied. An example is given here showing the calculation of the average potential energy of the system:

$$V = \langle V \rangle = \frac{1}{M} \sum_{i=1}^{M} V_i \tag{2.30}$$

where M is the number of microscopic configurations in the simulation and V_i is the potential energy of each configuration.

2.3.2.2.- Monte Carlo method

A Monte Carlo simulation consists of some physical or mathematical system that can be described in terms of probability distribution functions, $f(x^N)$, being x^N the coordinates of the N particles composing the system. The $f(x^N)$ describes the evolution of the overall system, whether in space, or energy, or time, or even some higher dimensional phase space. The goal of the Monte Carlo method is to simulate the physical system by random sampling from the $f(x^N)$ and by performing the necessary supplementary computations needed to describe the system evolution. In essence, the physics and mathematics are replaced by random sampling of possible states from $f(x^N)$ that describe the system (Frenkel and Smit, 2002):

$$f(x^N) = \frac{\exp\left[-\frac{1}{k_B T} V(x^N)\right]}{Z} \tag{2.31}$$

where Z is the partition function of the system:

$$Z = \int dx^N \exp\left[-\frac{1}{k_B T} V(x^N)\right] \tag{2.32}$$

The central task of a MC simulation is to randomly generate points in the configuration space according to this probability distribution $f(x^N)$. This means that, on average, the number of points generated per unit volume around a point x^N is equal to $L \cdot f(x^N)$, where L is the total number of points that we have generated. Once we generate this distribution $f(x^N)$, a thermodynamic average of a magnitude A is calculated:

$$\langle A \rangle = \frac{1}{L} \sum_{i=1}^{L} L f(x_i^N) A(x_i^N) \tag{2.33}$$

The MC simulations used in this work have been used to load water molecules on a fixed sorbent (imogolite and gibbsite) in the canonical ensemble (NVT). This was accomplished by a random series of insertion steps and equilibration moves (only moves that do not change the loading were permitted) until the specified loading was reached.

The Metropolis algorithm was used to generate the configurations. The acceptance probability from an *m* to an *n* configuration in the NVT ensemble is given by:

$$P_{m,n} = \min\left\{1, \exp\left[\frac{E_n - E_m}{k_B T}\right]\right\} \tag{2.34}$$

where E_m is the total energy of configuration *m* and E_n is the total energy of configuration *n*. In other words, transitions to a configuration of lower energy ($E_n < E_m$) are always accepted, but transitions to high energy configurations ($E_n > E_m$) are only accepted with a probability which decreases exponentially with the difference in energy to zero. As such, high energy configurations are unlikely to be sampled, precisely what the probability density of the canonical ensemble dictates.

The Metropolis Monte Carlo method implemented in the Sorption code provides three step types for a canonical ensemble: rotation, translation and re-growth. A step type is selected at random, using the weights as specified at the start of the Sorption run. The selected step type is applied to a random sorbate as follows:

- Rotation: The selected sorbate is rotated about its center of geometry by an angle of $\delta\theta$ about an axis, *C*. The rotation $\delta\theta$ is drawn from a uniform distribution between $-\Delta_r$ and Δ_r, where Δ_r is the maximum rotation amplitude as specified at the start of the Sorption run. The axis *C* is the vector from a random point on a sphere to its origin.
- Translation: The selected sorbate molecule is translated by a distance of δr along an axis, *C*. The translation δr is drawn from a uniform distribution between 0 and Δ_t, where Δ_t is the maximum translation amplitude as specified at the start of the Sorption run. The axis *C* is the vector from a random point on a sphere to its origin.
- Re-growth: The selected sorbate molecule is removed and a new sorbate is inserted at a random position in the sorbent with a random orientation.

REFERENCES

Cuello, G.J. (2007) Structure factor determination of amorphous materials by neutron diffraction. Journal of Physics: Condensed Matter, 20(24).

Cygan, R.T., Liang, J.J., and Kalinichev, A.G. (2004) Molecular models of hydroxide, oxyhydroxide, and clay phases and the development of a general force field. Journal of Physical Chemistry B, 108(4), 1255-1266.

Debye, P. (1915) X-ray dispersal. Annalen Der Physik, 46(6), 809-823.

Delley, B. (1990) An all-electron numerical method for solving the local density functional for polyatomic molecules. Journal of Chemical Physics, 92(1), 508-517.

-. (2000) From molecules to solids with the DMol(3) approach. Journal of Chemical Physics, 113(18), 7756-7764.

Egami, T., and Billinge, S.J.L. (2003) Underneath the Bragg Peaks: Structural analysis of complex materials. Pergamon, Elsevier.

Frenkel, D., and Smit, B. (2002) Understanding Molecular Simulation: from algorithms to applications. Academic Press, San Diego.

Hohenberg, P., and Kohn, W. (1964) Inhomogeneous electron gas. Physical Review B, 136(3B), B864-&.

Kelly, S.D., Hesterberg, D., and Ravel, B. (2008) Analysis of Soils and Minerals Using X-ray Absorption Spectroscopy in Methods of Soil Analysis. Soil Science Society of America, Madison, WI.

Kohn, W., and Sham, L.J. (1965) Self-consistent equations including exchange and correlation effects. Physical Review, 140(4A), 1133-&.

Kresse, G., and Hafner, J. (1993) Ab-initio molecular dynamics for liquid metals. Physical Review B, 47(1), 558-561.

-. (1994) Ab-initio molecular dynamics simulation of the liquid-metal amorphous semiconductor transition in germanium. Physical Review B, 49(20), 14251-14269.

Plimpton, S. (1995) Fast parallel algorithms for short-range molecular dynamics. Journal of Computational Physics, 117(1), 1-19.

Rehr, J.J., and Albers, R.C. (2000) Theoretical approaches to x-ray absorption fine structure. Reviews of Modern Physics, 72(3), 621-654.

Teo, B.K. (1986) EXAFS: basic principles and data analysis. Springer, New York.

Chapter 3

Selenite and selenate adsorption mechanisms at the synthetic and biogenic imogolite – water interface

3.1.- Introduction

Three main processes are considered responsible for the selenium associations with mineralogical soil components at the mineral−water interface: adsorption, co-precipitation and surface precipitation. The two latter depend on the solubility of the target solid phases. Adsorption is defined as 'the process through which a chemical substance accumulates at the common boundary of two contiguous phases' (Sposito, 2004). It highly depends on factors like ionic strength of the medium, which can reduce the adsorption properties of some minerals through the reduction of the size of Stern layer of adsorption (Sposito, 2004), or the solution pH. Competition effects are also an important factor which may reduce selenium adsorption, *e.g.*, when fertilizers are applied on soils, like phosphates or nitrates. For instance, selenite sorption in Indian soils have been studied by (Dhillon and Dhillon, 2000), showing a decreasing of 50% when phosphate anions are present as competitors.

Two different mechanisms are responsible for the adsorption of selenium species (Balistrieri and Chao, 1987; Hansmann and Anderson, 1985; Neal et al., 1987a; Neal et al., 1987b): outer-sphere and inner-sphere complexation. Formation of outer-sphere complexes is an electrostatic-driven sorption mechanism, strongly dependent on surface charge and thus on solution ionic strength (Sposito, 2004). Inner-sphere complexes form when an ion is adsorbed "specifically" on a "crystallographic site", *i.e.*, when covalent or ionic bonds are created with functional sites present on the mineral faces. These bonds have a stronger degree of covalence and are more stable than outer-sphere complex formation (Sposito, 2004). They are responsible in much cases of the long-term immobilization of ions at the mineral/water interface (Duc et al., 2003).

Selenium associations with iron, aluminum and manganese oxides and hydroxides, carbonates and organic matter have been widely reported (Selim and Sparks, 2001). Iron and aluminum oxides have surfaces with a variable charge in function of the solution pH, which implies a higher sorption process of selenite and selenate at low pH, where the positive charge is developed in the mineral surface (Yu, 1997). For instance, selenite and selenate species adsorb onto ferric oxy-hydroxides, the affinity of these solids for selenate being generally smaller than for selenite (Balistrieri and Chao, 1987; Hayes et al., 1987; Lo and Chen, 1997; Su and Suarez, 2000; Zhang and Sparks, 1990). This behavior may be related to differences in the nature of respective surface complexes, and to geometrical factors that may affect the extent of inner-sphere complexation. In general, selenite is sorbed by inner-sphere complexation, although the exact coordination (mono- or bi- dentate) depends on the mineral structure and surface charge. Ferric oxy-hydroxides whose surface reactivity toward selenium species has been studied include: goethite (Balistrieri and Chao, 1987; Hayes et al., 1987; Hiemstra and Van Riemsdijk, 1999; Lo and Chen, 1997; Manceau and Charlet, 1994; Parida et al., 1997; Peak and Sparks, 2002; Su and Suarez, 2000; Zhang and Sparks, 1990) HFO (Hydrous Ferric Oxide) (Davis and Leckie, 1980; Hayes et al., 1987; Lo and Chen, 1997; Manceau and Charlet, 1994; Peak and Sparks, 2002; Su and Suarez, 2000), other iron oxy-hydroxide polymorphs (Parida et al., 1997) and hematite (Peak and Sparks, 2002). A list of the different complexes formed on the surfaces of these solids is given in Table 3.1.

The application of X-ray Absorption Spectroscopy (XAS) to the study of adsorbed complexes at the mineral-water interface has helped to explain striking macroscopic observations. It is the case of selenate oxyanions sorption on goethite and HFO. Some authors had pointed out that the sorption of selenate showed an ionic strength dependence, which was been traditionally attributed to the occurrence of an outer-sphere (electrostatic) mechanism of adsorption (Hayes et al., 1987). (Manceau and Charlet, 1994), demonstrated using XAS that selenate binds onto the goethite and HFO structures by forming inner-sphere complexes. In this case, the influence of humidity and drying processes in the sample conditioning was the responsible for the different conclusions.

Species	Adsorbent	Surface complex	Technique used	Reference
SeO_3^{2-} (selenite)	α-FeOOH (Goethite)	Bidentate inner-sphere	EXAFS	Hayes et al. (1987) Manceau and Charlet (1994)
			DRIFT	Su and Suarez (2000)
	α-Fe_2O_3	Bidentate inner-sphere	X-ray Standing Waves	(Catalano et al., 2006)
	am-$Fe(OH)_3$	Bidentate inner-sphere	DRIFT	Su and Suarez (2000)
	Hydrous Ferric Oxide	Bidentate inner-sphere	EXAFS	Manceau and Charlet (1994)
	Hydroxy Aluminum Polymer	Bidentate inner-sphere Outer-sphere	EXAFS, XANES	Peak (2006)
	Hydrous Manganese Oxide	Bidentate inner-sphere[a] Monodentate inner-sphere	EXAFS	(Foster et al., 2003)
	Hydroxy Aluminosilicate Polymer	Bidentate inner-sphere Outer-sphere	EXAFS, XANES	Peak (2006)
	Montmorillonite	Outer-sphere	EXAFS	(Charlet et al., 2007)
		Bidentate inner-sphere	EXAFS, XANES	Peak (2006)
SeO_4^{2-} (selenate)	am-$Fe(OH)_3$	Bidentate inner-sphere	ATR-FTIR, DRIFT	Su and Suarez (2000)
	α-Al_2O_3	Monodentate inner-sphere	EXAFS, XANES	Peak (2006)
	γ-Al_2O_3	Inner-sphere	EXAFS	(Boyle-Wight et al., 2002)
	α-FeOOH (Goethite)	Monodentate inner-sphere (at pH < 6) Outer-sphere (at pH > 6)	Raman, ATR-FTIR	(Wijnja and Schulthess, 2000)
		Outer-sphere		Hayes et al. (1988)
		Bidentate inner-sphere	EXAFS	Manceau and Charlet (1994)
	Hydrous Ferric Oxide	Bidentate inner-sphere	EXAFS	Manceau and Charlet (1994)

[a] The authors raise some concerns about the possibility that the observed Se(IV)-Mn(II) complex belongs to a surface precipitate and not to an adsorbed complex.

Table 3.1*. Surface complexes of selenium oxyanions adsorbed at the mineral/water interface of various iron, aluminum and manganese oxides and clays, whose structures have been described by spectroscopic methods.*

A recent paper by (Fukushi and Sverjensky, 2007), in which an extended triple layer model taking into account the electrostatics of water dipole desorption during ligand exchange reactions has predicted these differences in behavior.

The lower ionic strength and higher surface coverage used by (Hayes et al., 1988) is predicted to favor an outer-sphere selenate species, whereas the higher ionic strength used by (Manceau and Charlet, 1994), is predicted to favor an inner-sphere selenate species, as suggested also by (Peak and Sparks, 2002). This implies a high effect of the electrostatic potential of the mineral surface on the surface complexation mechanisms, as confirmed by (Hiemstra and Van Riemsdijk, 1999). These authors were able to fit the data of Hayes et al. (1988) assuming the formation of only a bidentate inner-sphere complex (Hiemstra and Van Riemsdijk, 1999).

Other studies focusing on the adsorption mechanisms of selenium oxyanions include the works of (Peak and Sparks, 2002), who employed Extended X-ray Absorption Fine Structure (EXAFS) and Attenuated Total Reflectance-Fourier Transform Infrared (ATR-FTIR) spectroscopies to determine selenite bonding mechanisms on hematite, goethite, and hydrous ferric oxide (HFO). They also showed that selenate forms only inner-sphere surface complexes on hematite, but it forms a mixture of outer- and inner-sphere surface complexes on goethite and HFO. This continuum of adsorption mechanisms is strongly affected by both pH and ionic strength.

Aluminum oxide reactions to selenite and selenate have been studied to a lower extent than their iron oxides counterparts. The sorption properties and mechanisms are however very similar. Concerning selenite, (Papelis et al., 1995), showed using EXAFS that inner-sphere complexes are formed on gibbsite, fact corroborated by the ionic strength independent behavior of the adsorption. Same results were found by (Schulthess and Hu, 2001). (Peak, 2006), showed that selenite forms a mixture of outer-sphere and inner-sphere bidentate-binuclear (corner-sharing) surface complexes on Hydrous Aluminum Oxides (HAO) and selenate forms primarily outer-sphere surface complexes on HAO. An interesting result shows that selenate forms outer-sphere surface complexes on corundum at pH 3.5 but inner-sphere monodentate surface complexes at pH 4.5 and above, on the same surface. This difference in behavior may be related to proton-promoted structural changes in the surface of corundum or to the co-existence of outer-sphere and inner-sphere complexes at low pH, which would be affecting the intensity of the EXAFS signal. Changes in the protonation state of the

selenate molecule are not expected due to the low pK_{a2} of the selenate molecule (pK_{a2} = 1.8) (Peak, 2006).

Following these works, we present here a combined theoretical and spectroscopic study of the selenite and selenate adsorption mechanisms at the imogolite − water interface. As it has been stated in Chapter 1.2, knowledge of the adsorption mechanisms of selenium oxyanions on imogolite is necessary to correctly understand the processes controlling selenium bioavailability in volcanic soils. Synthetic and biogenic imogolite samples have been used in this study. There is a general agreement in the literature than both synthetic and natural imogolite have similar atomic arrangements (Alvarez-Ramirez, 2007; Bursill et al., 2000; Farmer et al., 1983). Only differences in the bundle structure of the nanotubes have been reported, that could be partly explained supposing that synthetic imogolite has a slightly bigger diameter (2.2-2.4 nm) (Farmer et al., 1983) than natural imogolite (2.0 nm) (Cradwick et al., 1972). In this study, we have used synthetic and natural biogenic samples in order to assure that the studies performed on synthetic imogolite correctly mimic the processes that can be found in nature.

Selenite and selenate adsorption mechanisms at the synthetic and biogenic imogolite – water interface

A. Fernández-Martínez[1,2,3], K. Tazaki[4], G. J. Cuello[2,5], G. Roman-Ross[6], I. Alliot[7], D. Tisserand[1], A. C. Scheinost[8,9], L. J. Michot[10], E. Montarges-Pelletier[10], G. Sposito[3,11] and L. Charlet[1,3]

[1] *Equipe de Géochimie de l'Environnement, LGIT, University of Grenoble and CNRS. B.P. 53, 38041 Grenoble, France.*

[2] *Institut Laue-Langevin. B.P. 156, 38042 Grenoble, France.*

[3] *Environmental Science Policy and Management Department, University of California, Berkeley, CA 94720-3114, USA*

[4] *Department of Earth Sciences, Faculty of Science, Kanazawa University, Kakuma, Kanazawa, Ishikawa 920-1192, Japan*

[5] *Ikerbasque & Department of Applied Physics II, Faculty of Sciences, Basque Country University, 48080 Bilbao, Spain*

[6] *Department of Chemistry, Faculty of Sciences, University of Girona, Campus de Montilivi, 17071 Girona, Spain*

[7] *DRFMC SP2M NRS, CEA Grenoble, 38054 Grenoble, France*

[8] *Rossendorf Beamline ESRF, 38043 Grenoble, France*

[9] *Forschungszentrum Dresden Rossendorf, Inst Radiochem, 01314 Dresden, Germany*

[10] *Laboratory Environment & Mineralogy, INPL, UMR 7569 CNRS, 54501 Vandoeuvre Les Nancy, France*

[11] *Geochemistry Department, Lawrence Berkeley National Laboratory, Berkeley, CA 94720, USA*

To be submitted to Langmuir

ABSTRACT

The adsorption mechanisms of selenate and selenite at the external surface of synthetic and biogenic natural samples of imogolite –a nanotubular aluminosilicate present in the clay fraction of andisols and spodosols– have been studied using X-ray Absorption Spectroscopy and molecular modeling. Both oxyanions form inner-sphere complexes at the imogolite surface. This specificity of imogolite for selenate and selenite affects the geochemical cycling of selenium in volcanic environments, and is proposed as one of the geochemical pathways influencing the deficiency of selenium in organisms living in volcanic soils.

INTRODUCTION

Selenium is an essential element for nutrition of capital importance in the human biology. Nutrition scientists proclaim the year 1957 as the date when selenium started to be considered as an essential nutrient (Schwarz and Foltz, 1957). After its discovery by Berzelius, several episodes have underlined the importance of selenium in the human body. In 1935, 57 people from Keshan county (Heilongjiang province, China) died after a degenerative cardiac illness, related to the 'white muscle disease' suffered by animals (Gu, 1987). These illnesses were known to be related to a selenium deficit (Stone, 2009). Another sickness, the Kashin-Beck disease, responsible for a disorder of the bones and joints of the hands and fingers, elbows, knees, and ankles of children and adolescents mainly from the regions of North China, North Korea and Siberia, has been related to a deficit in selenium (Moreno-Reyes et al., 1998; Stone, 2009). Soil selenium content analyses have shown an important deficit in these regions, which implies a daily dietary consumption less than 10 μg day^{-1} (Kohrle et al., 2000; Moreno-Reyes et al., 1998).

Soils from volcanic regions, volcanic-ashes produced simultaneously to volcanic gases, and sediments developed from these ashes are usually rich in selenium (Byers et al., 1938; Davidson and Powers, 1959; Ihnat, 1989; Lakin, 1972). But, paradoxically, diseases related to selenium deficiency (*i.e.*, 'white muscle disease') have been also reported in regions of the world dominated by selenium-rich volcanic soils such as andosols (Rayman, 2000). In fact, andosols are the soils with higher selenium distribution coefficients (Nakamaru et al., 2005). The particle / solution distribution coefficient (K_d) of selenium in Japanese agricultural andosols are as high as 600-800 L kg^{-1}. The origin in this apparent discrepancy is two folded: on one hand, it has been reported that the specific mineralogical characteristics of volcanic soils lead to the immobilization of large quantities of organic matter (Wang and Chen, 2003); selenium associates with organic matter being immobilized and thus becomes unavailable to the biota (Wang and Gao, 2001). Clear difference should be made then between low bioavailability and deficiency, terms that have been used in a confusing way by some authors (Rayman, 2000; Reilly, 1997; Sirichakwal et al., 2005). On the other hand, little is known about the specific interactions of selenium oxyanions (predominant species of inorganic selenium in volcanic soils) and the mineralogical components specific to these soils (imogolite and allophane), which could be responsible of the low selenium bioavailability. Some studies have highlighted this possibility: sequential extractions

performed on andosol samples have shown high correlation coefficients between occurrence of short-range-ordered aluminosilicates such as allophane, imogolite and active aluminum, and selenium K_d values (Nakamaru et al., 2005). Selenium bioavailability in these soils may be thus controlled by the adsorption of selenite and selenate −the two predominant species in those oxic soils− on mineral surfaces and organic matter.

Imogolite ($Al_2(OH)_3SiO_3OH$) is an aluminosilicate mineral commonly found in some of these volcanic soil environments, such as the clay fraction of andosols (Ugolini and Dahlgren, 1991; Wada, 1989). It is a poorly-crystalline mineral of nanotubular structure, with an internal face dominated by silanol ($>SiOH^0$) functional groups and an external face composed by a curved gibbsite ($Al(OH)_3$), populated by neutral aluminol groups ($>Al_2OH^0$) ((Cradwick et al., 1972), see Figure 1).

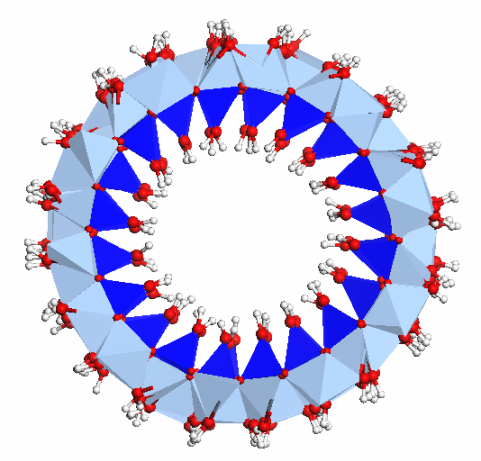


Figure 1*. Side view of the structure of imogolite. Light blue polyhedra are aluminum octahedral, dark blue polyhedra are silicon tetrahedral, red and white spheres are oxygen and hydrogen atoms respectively.*

The nanotubes have diameters of $d_i \approx$ 1nm (internal) and $d_e \approx$ 2.2 nm (external), and lengths in the order of the micrometer (Bursill et al., 2000; Cradwick et al., 1972; Vandergaast et al., 1985). The presence of amphoteric surfaces and the lack of isomorphic substitutions (which would act as centers of permanent charge) make imogolite a mineral with a variable charge only dependent on the pH of the soil solution. Permanent charge at the imogolite surface, and hence its ability to adsorb anions, has always been attributed to the presence of vacancies in its structure (Wada, 1989), although some authors have hypothesized a permanent charge that would be originated by the undersaturation of surface oxygen atoms due to the strain induced by the curvature (Alvarez-Ramirez, 2007; Guimaraes et al., 2007; Gustafsson, 2001). The high specific surface areas of these volcanic soils components, up to 800 m^2/g, and the positive charges that they develop may be the responsible for their high affinity of

selenium. Other soil components with high affinity for selenium are iron-humus complexes (Ihnat, 1989) and poorly crystalline iron oxides such as ferrihydrite, as *e.g.* for New Zealand soils (John et al., 1975).

While different pedogenetic processes have been proposed to explain the formation of imogolite in spodsols (Dahlgren and Ugolini, 1989; Wang et al., 1986), there is general agreement that imogolite is precipitated in-situ in B horizons of andosols, where there is a low content of Al-complexing organic compounds and where the low-leaching rate favors the polymerization of Al and its co-precipitation with monomeric Si (Ugolini and Dahlgren, 1991). More recently, other authors have proposed a biotic route for the formation of imogolite directly from plagioclase (Tazaki et al., 2006). These authors observed the development of bio-films containing imogolite at the surface of incubated pumice grains, suggesting that imogolite bio-mineralization may be another pathway for the formation of imogolite on volcanic environments.

In this study we explore the adsorption mechanisms of selenite, SeO_3^{2-}, and selenate, SeO_4^{2-}, two oxyanions present in aerated soils like andosols, on two different specimens of imogolite: synthetic and biogenic. Adsorption isotherms have been performed on the synthetic samples prior to the spectroscopic experiments. The local environment of the selenium oxyanions adsorbed on imogolite has been studied using X-ray Absorption Spectroscopy (XAS) and molecular simulations. Knowledge of the mechanisms of retention of selenium oxyanions at mineral surfaces is essential to understand the processes controlling the biogeochemical cycling of selenium in volcanic soils, and to correctly assess its deficit and any potential selenium supplementation strategy that may be applied in these environments.

MATERIALS AND METHODS

Synthetic samples

Imogolite was synthesized following the procedure described by (Denaix et al., 1999). Aluminum nitrate (99.999%, Alfa Aesar) and Tetraethyl orthosilicate (99.999%, Alfa Aesar) were mixed in ultra pure water (MilliQ) at an Al/Si ratio of 2 and aluminum concentration of 0.002 M. Dilute NaOH (0.1 M) was injected at a rate of 2 mL/min under vigorous stirring, until reaching an hydrolysis ratio OH/Al of 1. After injection, the solution was stirred for 12h to avoid the polymerization of aluminum hydroxides. The solutions were heated at 95ºC during 5 days in closed Teflon bottles. To remove excess alcohol, Na^+ and NO_3^- ions from solution, the solutions were dialyzed against

ultra pure water (MilliQ) during 15 days, using a molecular weight cut-off membrane of 2000 Da (Spectra/Por® membranes, Carl Roth). After dialyzing, part of the imogolite solution was freeze-dried and other part was concentrated using a roto-evaporation method, avoiding the formation of flocks.

Natural samples

Pumice rocks were collected from the Kurayoshi pumice layer in Kurayoshi, Tottori, Japan. They were rinsed ten times with distilled water to remove fine particles. The washed grains were incubated at room temperature under distilled water in a covered baker with a glass plate inside. They were incubated during one year during which solution pH, Eh and dissolved oxygen were monitored using a HORIBA portable spectrometer. After the incubation period, transparent films that were identified as imogolite developed on the grain surfaces and covered the glass plate. Transmission and Scanning Electron Microscopy (SEM) reveal the presence of *Gram-negative* bacteria and of imogolite films in close contact with the bacterial cell wall. More details about the incubation experiments and characterization of the resulting imogolite films have been published elsewhere (Tazaki et al., 2006). SEM images of biogenic imogolite are presented in Figure 2.

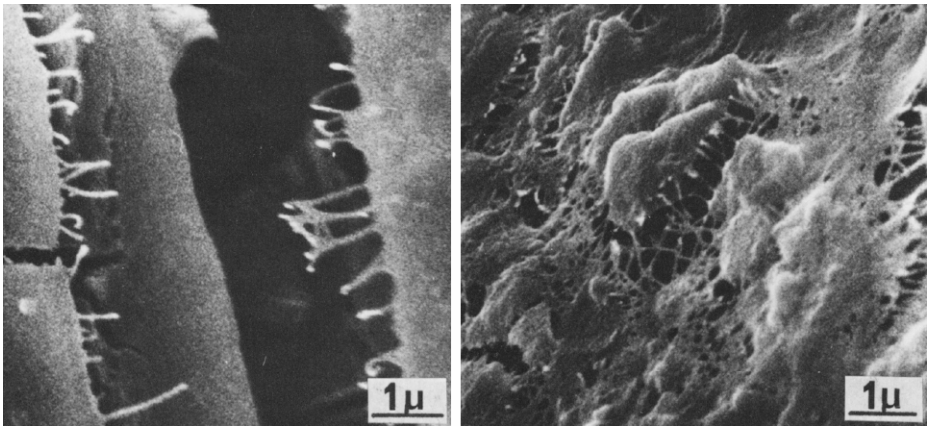


Figure 2*. SEM images of the entangled network of imogolite and biofilm developed over pumice grains.*

Fourier Transform Infrared Spectroscopy (FTIR)

FTIR spectra of the imogolite freeze-dried powders were taken to characterize the product obtained after the synthesis. Transmission FTIR spectra were obtained using a Bruker HYPERION 3000 FTIR microscope in the transmission mode. KBr pellets (1

mg of imogolite in 100 mg of KBr) were used. One hundred scans taken using a resolution of 2 cm^{-1} were averaged to obtain spectra in the range 4000–370 cm^{-1}.

Adsorption experiments

Sorption experiments of selenite, SeO_3^{2-}, on synthetic imogolite were conducted in a N_2 atmosphere glove box (Jacomex) in which the oxygen partial pressure (pO_2) was monitored continuously with a Jacomex O_2 sensor. The O_2 content never exceeded 1 ppm in the glove box atmosphere, corresponding to a maximum solute O_2 concentration of 0.13 μmol/L. In these experiments, the sorption of SeO_3^{2-} was studied as a function of pH on a short reaction time scale. Experiments were carried out in closed 350 ml glass reactors with three inputs, one for the pH electrode and the two others for stock solution/suspension addition and sample extraction, respectively. An aliquot of imogolite stock suspension in the form of gel containing 200 mg of imogolite was added to 0.001 M $NaNO_3$ ionic background solution samples. The suspension was basified with NaOH to pH 9 overnight (approximately 16 h), and then a solution containing selenite was added until a total concentration of 0.008 mmol/L was reached in the reactor. The sorption experiments proceeded by decreasing the pH incrementally with successive additions of HNO_3. After each addition, the suspension was allowed to equilibrate. Once the pH drift was less than 0.02 pH unit/10 min, a 10 ml sample of suspension was filtered through a 0.22 μm pore size membrane and analyzed for selenium concentration by induced coupled plasma atomic emission spectrometry (ICP-AES). Samples at pH 4, 7 and 9 were filtered using 0.22 μm pore size membranes and loaded into sample-holders for XAS measurements and sealed with Kapton tape. These sample-holders were introduced into small plastic boxes that were taken out of the glove box and immediately shock-frozen in liquid nitrogen. The samples were transported to the beamline in a Dewar filled with liquid nitrogen. At the beamline, the samples were transferred within 2 min from the Dewar to the He atmosphere of the closed-cycle He cryostat and cooled to 15 K within less than 20 min.

The same procedure used to obtain the selenite adsorption isotherm on synthetic imogolite was repeated for selenate under the hood, without the need of anoxic conditions. Samples at pH 3 and 4 were filtered and loaded into the XAS sample-holders. The selenate samples were measured at the FAME beamline of the ESRF (Grenoble, France). No special caution was taken in the transport of the samples, due to their inertness to oxygen.

Biogenic transparent films of imogolite were recovered using a spatula from the surfaces of pumice rock grains, after incubation for one year, as indicated above. 25 mg of imogolite biogenic films were added to a solution containing 8 mmol/L of selenate. The pH was fixed to pH 5 using HNO_3. After two hours, the solutions were filtered and the biogenic samples were loaded into XAS sample-holders.

X-ray absorption spectroscopy

Two different experimental set-ups were used to acquire selenium K-edge Extended X-ray Absorption Fine-Structure (EXAFS) spectra. EXAFS spectra of samples of selenite adsorbed on synthetic imogolite were collected at the Rossendorf Beamline at ESRF (Grenoble, France). The energy of the X-ray beam was tuned by a double crystal monochromator operating in channel-cut mode using a Si(111) crystal pair. Two platinum-coated Si mirrors before and after the monochromator were used to collimate the beam into the monochromator and to reject higher harmonics. A 13-element high purity germanium detector (Canberra) together with a digital signal processing unit (XIA) were used to measure reaction samples in fluorescence mode. Reference samples were measured in transmission mode using Oxford ionization chambers (300 mm) filled with 95% N_2 and 5% Ar (I_0) and with 100% Ar (I_1 and I_2). Spectra were collected at 15 K using a closed cycle He cryostat with a large fluorescence exit window and a low vibration level (CryoVac). Photoinduced redox reactions were effectively prevented by the cold temperature, since the absorption edges remained stable during short-term exposure (10 min) as well as during the EXAFS measurements which took up to 5 h. For energy calibration, a gold foil (K-edge at 11919 eV) was chosen because of its greater inertness in comparison to Se. Dead time correction of the fluorescence signal, energy calibration and the averaging of single scans were performed with the software package SixPack.

EXAFS spectra of samples of selenate adsorbed on synthetic and biogenic imogolite were collected at the FAME beamline (Proux et al., 2005) at ESRF (Grenoble, France). The energy of the X-ray beam was tuned by a double crystal monochromator using a Si(220) double-crystal. The spectra were acquired using fluorescence mode with a germanium 30-element detector. The experiments were performed at room temperature.

Normalization, transformation from energy into *k* space, and subtraction of a spline background was performed with WinXAS using routine procedures (Ressler, 1998). The EXAFS data were fitted with WinXAS using theoretical backscattering amplitudes

and phase shifts calculated with FEFF 8.2 (Ankudinov et al., 2002). The fits were performed in the real space. This method provides a precision of ±0.01 Å for shell distances and a resolution of about ±0.1 Å for neighboring shells. The error of coordination numbers is ± 25%.

DFT calculations

Geometry optimizations of selenium complexes adsorbed of imogolite clusters were performed using DMol3 (Delley, 2000). Prior to the imogolite calculations, a calibration step was performed in order to optimize the parameters of the calculations. For this purpose we have selected to use the structure of $Al_2(SeO_3)_3 \cdot 6H_2O$, reported by (Morris et al., 1992) from X-ray data. Different approximations of the DFT were tried. First, calculations using the Local Density Approximation and the Perdew and Wang exchange functional (Perdew and Wang, 1992) were performed, resulting in an underestimation of the bond lengths and a poor description of the hydrogen bonding. For this reason the Perdew–Burke–Ernzerhof (PBE) exchange correlation functional (Perdew et al., 1996) of the Generalized Gradient Approximation (GGA) was chosen to calculate the exchange-correlation energy. The PBE approximation reproduced well the lattice parameters of the $Al_2(SeO_3)_3 \cdot 6H_2O$ structure, within a 5%. The bond lengths were slightly overestimated by the same percentage. GGA-PBE was the approximation providing the best behavior of water hydrogen bonding. A Double Numerical plus Polarization (DNP) set (Delley, 1990) was used as basis set to describe the atomic orbitals.

An atomic cluster formed by 13 aluminum octahedra and 3 silicon tetrahedra extracted from a 1 × 1 × 3 structure of imogolite was used in the cluster calculations of selenium complexes. The size of the cluster was chosen to have at least four central aluminum octahedra coordinated with the same coordination found the structure of imogolite.

Three different complexes of selenite adsorbed at the surface of this cluster were simulated. Explicit water was introduced on the $>SiOH^0$ surface in order to prevent the formation of hydrogen bonds between adjacent silanol groups at the internal surface, which creates a distortion in the structure. After optimization, all the clusters preserved the curvature of the structure.

RESULTS

FTIR of synthetic imogolite

In Figure 3, structural bands belonging to imogolite can be recognized at frequencies 423, 560, 937 and 3500 cm^{-1}, characteristic of imogolite structure (Farmer et al., 1979; Parfitt et al., 1980). The position of the band at 995 cm^{-1} corresponding to Si-O stretching depends on the Al:Si ratio. A low Al:Si ratio shifts the band towards higher wavenumbers (Henmi et al., 1981). The peak at 995 cm^{-1} is indicative of a structure with a 2:1 Al:Si ratio, as in the structure of imogolite.

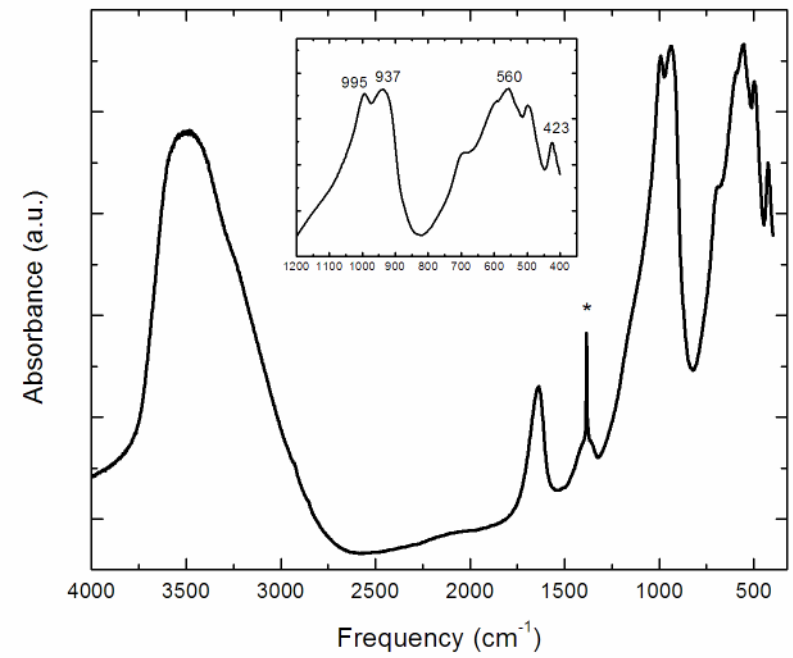


Figure 3*. FTIR spectra of synthetic imogolite. The band marked with an asterisk (*) corresponds to nitrate.*

Adsorption isotherms

The characteristic disordered texture of freeze-dried imogolite is that of an entangled network of nanotubes, forming aggregates (flocks) that are very difficult to re-disperse in solution. For this reason, adsorption experiments were performed using imogolite in the form of gel instead of freeze-dried powder. This allows maximizing the surface area available for adsorption. Figure 4 shows the results of the adsorption isotherms of selenate and selenite on imogolite.

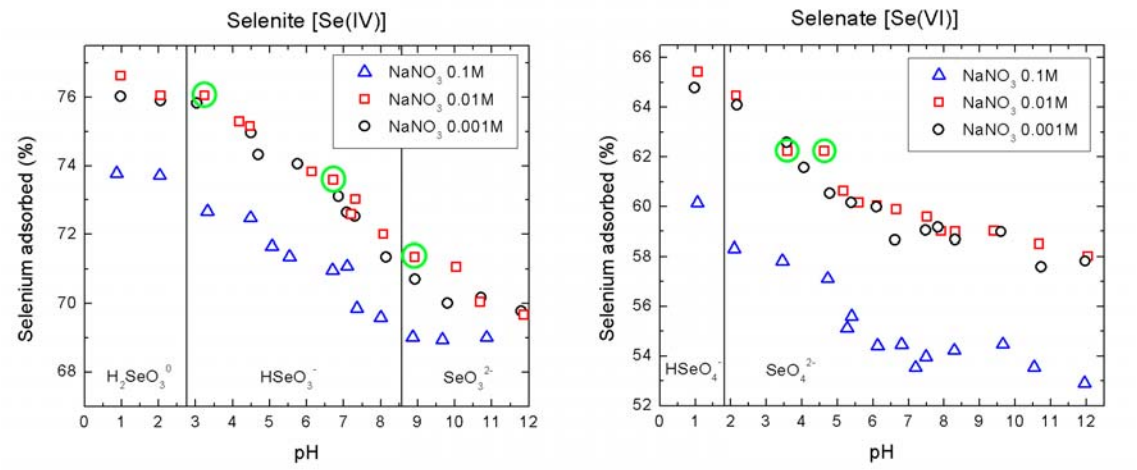


***Figure 4**. Adsorption isotherms of selenite (left) and selenate (right) in function of the solution pH. The protonation state of both oxyanions is indicated at the bottom of both graphs. The vertical lines indicate the values of pK_a for both oxyanions. Green circles indicate the samples that have been measured using X-ray absorption spectroscopy.*

The dependence of the adsorption on the ionic strength has been used classically as a test to discern the mechanism of adsorption by which a molecule is adsorbed at the mineral/water interface (Hayes et al., 1987). Formation of outer-sphere complexes is an electrostatic driven sorption mechanism, strongly dependent on surface charge and thus on solution ionic strength (Sposito, 2004). On the other hand, inner-sphere complexes form when an ion is adsorbed ‘‘specifically’’ on a ‘‘crystallographic site’’, *i.e.*, when covalent or ionic bonds are created with functional sites present on the mineral faces. These bonds have a stronger degree of covalence and are more stable than outer-sphere complex formation (Sposito, 2004). The results at I_{NaNO3} = 0.001 M and I_{NaNO3} = 0.01 M show an adsorption behavior independent of the ionic strength, which would indicate that an adsorption process involving a specific inner-sphere mechanism is taking place. However, lower percentages of adsorption are attained at I_{NaNO3} = 0.1 M. Two different facts could explain this difference: (1) the isotherms are dependent on the ionic strength, being the dependency indistinguishable in the case of lower I_{NaNO3} values, and (2) at high I_{NaNO3} values, the flocculation of the imogolite nanotubes takes place, reducing their specific surface area. Imogolite is known to form liquid crystals, whose structure varies in function of the imogolite concentration, the ionic strength and of the solution pH (Donkai et al., 1993). When the ionic strength increases, the liquid crystal phase is no longer stable, and flocculation of the imogolite tubes takes place, lowering the surface area available for adsorption.

The sorption isotherms for both oxyanions show an adsorption edge at about pH 5 and different percentages of adsorbed selenium depending on the ionic strength (I_{NaNO3}) and the pH of the solution. At high solution pH values (pH 10) around ~69% of the selenite has adsorbed onto the imogolite surface. The adsorption of selenate at this pH is lower, showing percentages of ~53% at I_{NaNO3} = 0.1 M and ~58% at I_{NaNO3} = 0.01 M and I_{NaNO3} = 0.001 M. Also, no positive charge is expected to develop at these high solution pH values by protonation of aluminol or silanol functional groups. Considering the behavior of the external surface charge as similar to that of gibbsite, the values of the protonation constant for the doubly-coordinated neutral aluminol groups would be pK_{a1} ~ 5.5 log units (Bickmore et al., 2004; Gan and Franks, 2006), or even pK_{a1} ~ 0.0 log units (Hiemstra et al., 1996). This would indicate that at pH 10 the external surface of imogolite would be neutral, which would prevent the adsorption of anions. Reactivity of hydroxylated silica surfaces has been studied reporting pK_{a1} values for silanol deprotonation from 2 (Brinker and Scherer, 1990) to 5 (Arai et al., 2006), also indicating a neutral or negatively charged internal surface at pH 10. The high percentages of selenite and selenate adsorbed at high solution pH values could be then explained by two different hypotheses, or by the combination of both: (1) the presence of a small permanent positive charge at the external surface of imogolite, as it has been predicted by (Gustafsson, 2001); (2) the presence of vacancies at the octahedral layer, composed by aluminum octahedra. These vacancies would originate $>AlOH^{-1/2}$ sites whose pK_{a1} has been predicted to be at pK_{a1} = 10 (equation 1), implying that these sites would be positively charged at solution pH values lower than 10:

$$> AlOH_2^{+1/2} \leftrightarrow \quad > AlOH^{-1/2} + H^+ \qquad (1)$$

These two hypotheses would explain also the positive values of electrophoretic mobility found by some authors (Su and Harsh, 1993; Tsuchida et al., 2004).

The presence of a positive charge would explain any possible electrostatic mechanism of adsorption. However, the formation of inner-sphere complexes, already observed for gibbsite, cannot be excluded. Inner-sphere complexes originate by the structural affinity of the sorbent with the sorbates (Sposito, 2004).

Selenite X-ray Absorption Spectroscopy and DFT modeling

In order to discern the mechanisms of adsorption responsible for the immobilization of selenium oxyanions at the imogolite-water interface, EXAFS experiments were

performed on six samples prepared at different solution pH values and at I_{NaNO3} = 0.001 (see green circles in Figure 4). The Fourier transformations of the EXAFS signal reproduce the local environment around the selenium atoms. This function is usually called the Radial Distribution Function (RDF). The RDFs of the selenite samples (Figure 7) show the presence of a first shell centered at r_1 = 1.70 Å, corresponding to the three oxygen atoms forming the selenite molecule, $HSeO_3^{2-}$, and a second shell with lower intensity. The presence of a second shell in the RDF is indicative of the formation of a surface complex, in the case that the solution is not saturated with respect any solid phase of selenium which could eventually precipitate. The concentrations used in this work are low enough to prevent the formation of other solid phases.

In order to understand the origin of the second shell cluster-type DFT calculations of selenite complexes at the imogolite surface have been performed. The optimization of the geometry of these clusters allows obtaining a reliable structure that can be used as input in the analysis of the EXAFS data. Three different structures were optimized (see Figure 5), considering the formation of two different selenite inner-sphere complex linked to the surface through bidentate ligands, and of an outer-sphere complex forming hydrogen bonds with three $>Al_2OH^0$ groups from the surface.

In a first try, a cluster of atoms including a shell of adsorbed water (one water molecule for each oxygen surface atom) was included in a calculation containing a selenite molecule forming an inner-sphere complex with a bidentate ligand. The result of the calculation showed that the geometry of the selenite complex changed depending on the structure of the hydrogen bonds formed between water molecules and the oxygens of the ligand and of the selenite molecule. For this reason, simpler structures containing only one water molecule were performed, in order to reduce the degrees of freedom of the system. It has been shown that the inclusion of explicit water in DFT simulation of adsorbed complexes strongly affects the charge distribution between a sorbent and a sorbate, influencing vibrational properties and the stability of surface complexes (Hiemstra et al., 2007; Kubicki et al., 2007). In order to evaluate the effect of water on the complexes studied, we have included a water molecule in some of the calculations, oriented with an OH pointing perpendicular to the surface and donating a hydrogen bond to a surface oxygen atom. This water molecule orientation has been observed in simulations of the imogolite − water interface, being the most stable configuration of water at the imogolite surface (Creton et al., 2008).

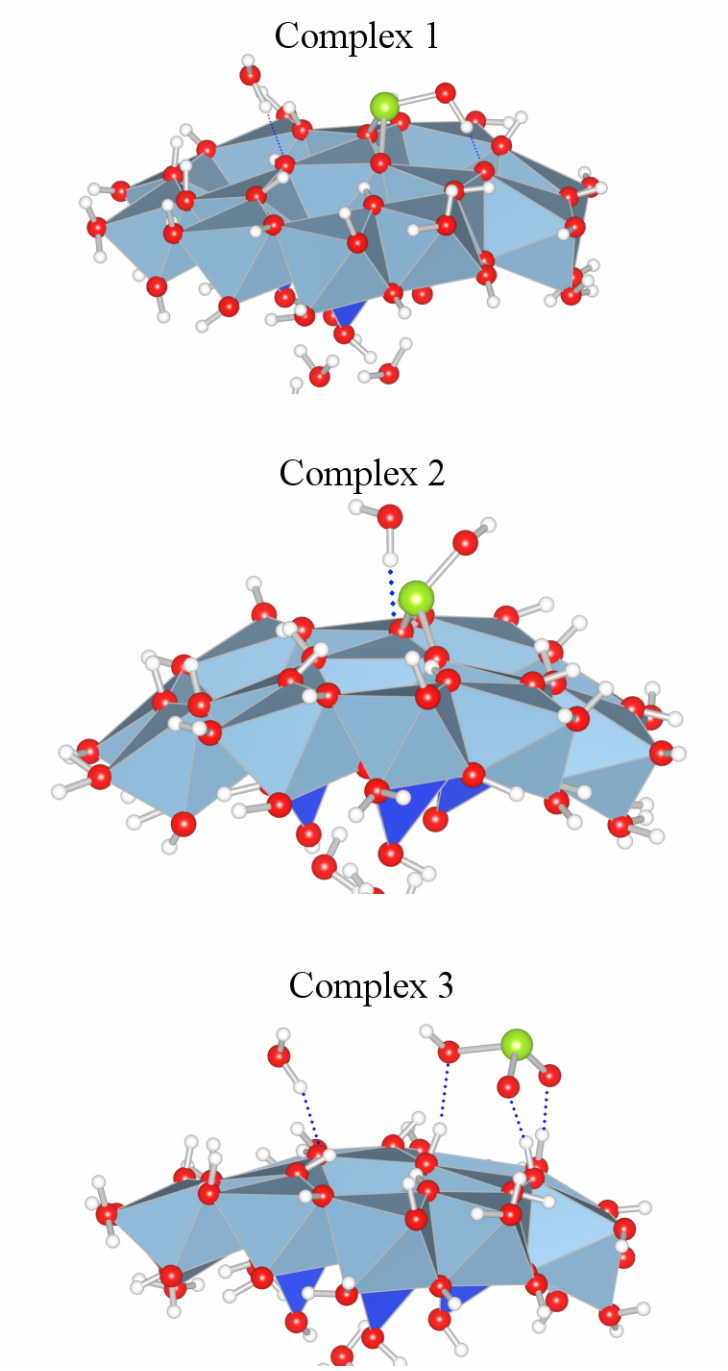


Figure 5. *Optimized models of selenite complexes at the imogolite cluster. Colors are the same as in Figure 1. The green sphere is the selenium atom. Complexes 1 and 2 are inner-sphere selenite complexes with mononuclear bidentate ligands. In complex 1 the selenite hydrogen atom forms a hydrogen bond with a surface oxygen atom. The inclusion of a water molecule forming a hydrogen atom with one of the oxygen atoms belonging to the ligand forces the selenite molecule to adopt an orientation with its basal plane perpendicular to the surface, as in complex 2. Complex 3 is an inner-sphere complex in which the three selenite oxygen atoms*

form hydrogen bonds with the surface over an octahedral vacant site. Complex 2 shows a very good agreement with the EXAFS data.

Figure 5 shows the DFT-optimized structures of the selenite complexes. The resulting distances are shown in Table 1. In complex 1 the water molecule was initially placed far from the selenite molecule. The optimized structure shows the formation of a hydrogen bond between the hydrogen atom of selenite with a surface oxygen atom. The complex 2 shows a water molecule giving a hydrogen bond to a surface atom. In this case, the presence of the water molecule affects the orientation of the selenite molecule, whose basal plane (formed by the three oxygen atoms) is almost perpendicular to the surface due to a weak hydrogen bond between the water oxygen atom and the selenite hydrogen atom. This water molecule affects also the geometry of the selenite molecule. The strong hydrogen bond formed between the water molecule and the surface makes that the non-bonded oxygen atom from the selenite molecule is repelled. The selenite molecule is then highly deformed, with one O-Se-O angle of almost 180°, and with no symmetry (C_1), which is very unrealistic (see right part of Figure 6). Energetically, this deformation is not favorable, being the difference in energy with the complex 1 of ΔU = 5.44 eV.

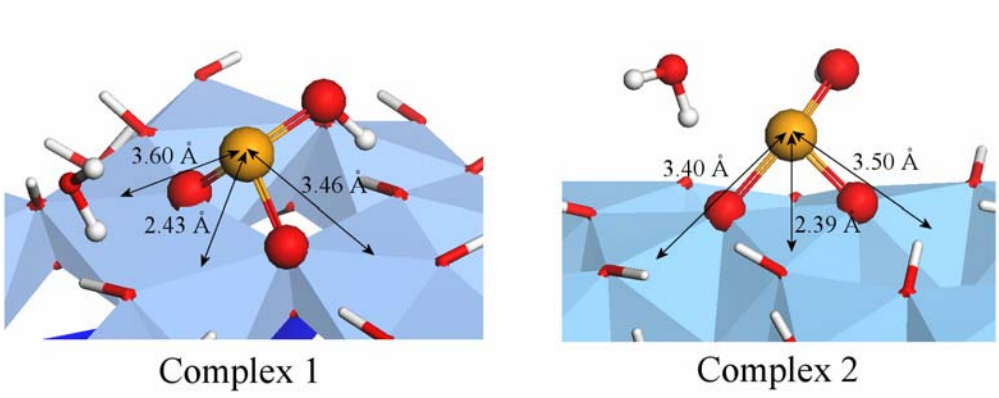


Figure 6*. View of complexes 1 and 2. The position of the water molecule influences strongly the geometry of the adsorbed selenite molecule. In complex 1 the water molecule is far from the selenite. In complex 2 the water molecule donates a hydrogen bond to one of the oxygen atoms participating in the ligand, distorting the selenite.*

The decreasing of the selenite symmetry from C_{2v} to C_1 would affect its vibrational properties, generating new modes of vibration that could be observed using FTIR spectroscopy. The observation of these modes on a selenite molecule adsorbed at the mineral−water interface with C_1 symmetry has never been observed, to our knowledge.

Only (Wang and Zhang, 2002) reported a C_1 symmetry for the HSO_3 molecule, but they did not reported its origin. This fact and the disagreement with the Se-Al distances observed by EXAFS make that the presence of complex 2 at the imogolite−water interface is very unlikely.

In complex 3 the selenite molecule is placed over a vacant octahedral site, with its basal plane oriented parallel to the surface. The three selenite oxygen atoms are receiving hydrogen bonds from surface OH groups, stabilizing the position of the molecule.

Complex	**Atoms**	**N**	**R (Å)**
1	<Se-O>*	3	1.768
	$Se\text{-}Al_1$	1	2.43
	$Se\text{-}Al_2$	1	3.46
	$Se\text{-}Al_3$	1	3.60
2	<Se-O>*	3	1.84
	$Se\text{-}Al_1$	1	2.39
	$Se\text{-}Al_2$	1	3.40
	$Se\text{-}Al_3$	1	3.50
3	<Se-O>*	3	1.778
	$Se\text{-}Al_1$	1	4.19
	$Se\text{-}Al_x$	-	> 5

* *The average Se-O distance has been reported in order to compare to the EXAFS data, where the resolution is not high enough to allow resolving the differences between the three Se-O distances expected in the $HSeO_3^-$ molecule.*

Table 1*. Interatomic distances obtained from DFT geometry optimizations of the complexes shown in Figure 5. In complex 3 most of the Se-Al distances are longer than 5 Å, and thus not observable by EXAFS. The deformation of the selenite pyramidal geometry in complex 2 yields very long Se-O distances.*

The fits of the RDF functions are shown in Figure 7. Resulting interatomic distances, coordination numbers and Debye-Waller factors are given in Table 2. The results for selenite are similar for the samples at the three pH values (4, 7 and 9), all of them revealing a two-shell structure. The fitting procedure has been as follows: EXAFS phases and amplitudes have been generated for the three structural models optimized by DFT using FEFF8.2. Each model was tested and the best model was selected in view of the agreement between theoretical and experimental interatomic distances. The best fit results are found using the structure of complex 1 as initial structure. In this complex

(see Figure 6), apart from the three O atoms at $<d_{Se-O}>$ = 1.768 Å, one Al atom is placed at a distance of d_{Se-Al1} = 2.43 Å and two more at d_{Se-Al2} = 3.46 Å and d_{Se-Al3} = 3.60 Å. The distances and coordination numbers obtained after fitting of the RDF functions are in excellent agreement with the structure of complex 1. The small values of the Debye-Waller factors are indicative of the goodness of the structural model, revealing low structural disorder apart from the effect of the low temperature at which the experiments were performed.

Species	**pH**	**S_0^2**	**E_0 (eV)**	**Atoms**	**R (Å)**	**N**	**σ^2 (Å^2)**
Se(IV)	4	0.90	14.45	Se-O	1.701 ± 0.006	3*	0.001 ± 0.0005
				Se-Al_1	2.41 ± 0.03	0.65 ± 0.15	0.005 ± 0.002
				Se-Al_2	3.39 ± 0.03	1*	0.001 ± 0.001
				Se-Al_3	3.57 ± 0.04	1*	0.001 ± 0.001
Se(IV)	7	0.90	11.50	Se-O	1.687 ± 0.003	3*	0.001 ± 0.0004
				Se-Al_1	2.36 ± 0.02	0.85 ± 0.20	0.001 ± 0.001
				Se-Al_2	3.36 ± 0.02	1*	0.006 ± 0.001
				Se-Al_3	3.58 ± 0.04	1*	0.002 ± 0.001
Se(IV)	9	0.90	16.65	Se-O	1.688 ± 0.006	3*	0.002 ± 0.001
				Se-Al_1	2.35 ± 0.03	1.05 ± 0.25	0.002 ± 0.001
				Se-Al_2	3.37 ± 0.02	1*	0.005 ± 0.002
				Se-Al_3	3.70 ± 0.03	1*	0.007 ± 0.002

* *All the coordination numbers have been fixed to their theoretical values (see Table 1) except for the first shell of aluminum atoms.*

Table 2*. Interatomic distances (R), coordination numbers (N) and mean-square relative displacements (σ^2) obtained from EXAFS data analyses.*

In addition, tests of the stability of these results have been done by trying to fit the RDFs using the same EXAFS paths with different initial distances. The results always converged to the structure of complex 1, indicating the accuracy of the optimized model. However, the fitted value of the coordination number of the first shell of Al, at d_{Se-Al1} ~ 2.40 Å, characteristic of a mononuclear bidentate ligand, deviates significantly from the expected theoretical value of $N_{2\text{-}DFT}$ = 1, falling to values of $N_{2\text{-}EXAFS}$ = 0.65 ± 0.15. For this reason we have evaluated a possible structure where the Al shell at d_{Se-Al1} ~ 2.40 Å is not present (complex 1B, see Figure 8; the vacant site is marked with an X). This complex has a mononuclear bidentate ligand over an octahedral vacant site. In this

case the Se-Al distances match perfectly those of the complex 1 (see Table 2), the first Al shell not being present in the structure. Nevertheless, the best fit is found when this first Al shell is included in the data refinement, giving the values reported in Table 2. This fact could indicate that complexes 1 and 1B are occurring simultaneously and thus that vacancies are present in the structure of imogolite.

Optimization of complex 3 yields distances to the Al atoms that are too long in comparison with the distances observed in the EXAFS data. All the tests trying to fit the data with this model failed, which led us to disregard it as a candidate to explain selenite adsorption mechanisms. Other complex evaluated was an inner-sphere complex with a trinuclear bidentate ligand, arranged in the same way as the orthosilicate molecules at the internal imogolite surface. However, the distances between apical oxygen atoms of neighboring aluminum octahedra are too long to form this complex.

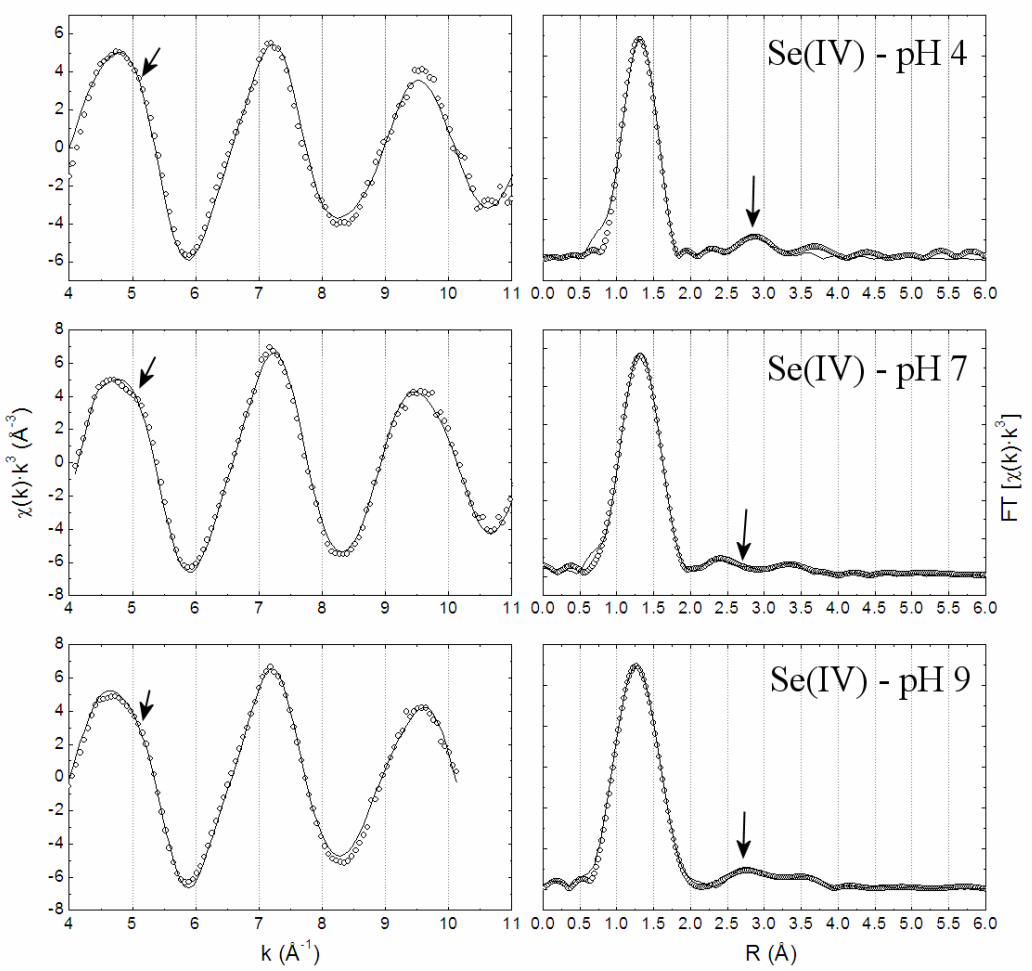


Figure 7*. EXAFS signals (left) and their Fourier transformations (RDFs, right) of selenite [Se(IV)] adsorbed on synthetic imogolite. Experimental data are represented by points; fits by*

solid lines. The arrows indicate the shoulder corresponding to the second shell in the EXAFS signal and its corresponding effect in the RDFs.

Selenate X-ray Absorption Spectroscopy and DFT modeling

The three selenate samples studied, (two synthetic and one biogenic) show a RDF composed of two shells indicating the presence of a well ordered structure around the selenate ion (see Figure 10). The second shell is more pronounced than in the case of selenite. In order to obtain a structural model from which to generate the phases and amplitudes for the EXAFS data analysis, a structural model was constructed. The model, optimized using DFT calculations, represented an inner-sphere complex of selenate (Figure 9).

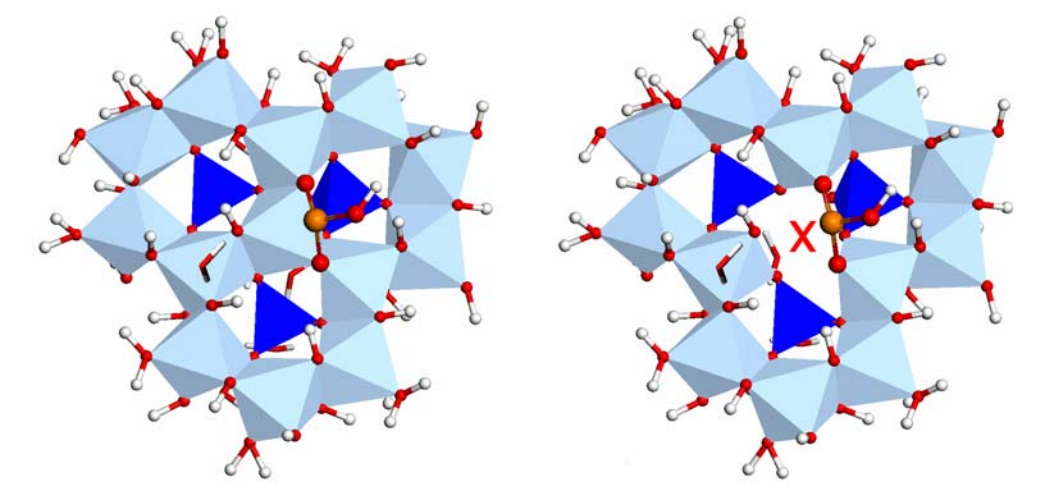


***Figure 8**. Left: complex 1. Right: complex 1B with one vacant octahedral aluminum site. The selenium atom is represented by a yellow sphere.*

After visual examination of the RDFs obtained from EXAFS data, we decided to construct a complex with a bidentate mononuclear ligand. The interatomic distances of the geometry optimized selenate complex are given in Table 3.

In the optimized structure two of the Se-O distances are longer than in the aqueous selenate molecule, where they have values of $d_{Se\text{-}O}$ = 1.65 Å (Manceau and Charlet, 1994). This elongation is caused by the mismatching of distances between oxygen atoms from the aluminum octahedron, with values of $d_{O\text{-}O}$ ~ 2.85 Å, longer than the O-O distances in the selenate molecule ($d_{O\text{-}O}$ ~ 2.72 Å); the formation of an inner-sphere complex makes that the Se-O distances of the selenate molecules increase, decreasing the symmetry of the molecule from T_d to C_s, a symmetry group including a mirror

plane. The local structure of the selenium atoms includes three shells of aluminum atoms placed at distances of $d_{Se\text{-}Al1}$ = 2.25 Å, $d_{Se\text{-}Al2}$ = 3.17 Å and $d_{Se\text{-}Al3}$ = 3.67 Å.

Complex	Atoms	N	R (Å)
1	<Se-O>*	3	1.725
	$Se\text{-}Al_1$	1	2.25
	$Se\text{-}Al_2$	1	3.17
	$Se\text{-}Al_3$	1	3.67

* *The average Se-O distance has been reported in order to compare to the EXAFS data, where the resolution is not high enough to allow resolving the differences between the four Se-O distances expected in the adsorbed SeO_4^{2-} molecule.*

Table 3*. Interatomic distances obtained from DFT geometry optimizations of the selenate complex.*

Species	pH	S_0^2	E_0 (eV)	Atoms	R (Å)	N*	σ^2(Å^2)
Se(VI)	3	0.90	14.45	Se-O	1.68 ± 0.01	4	0.001 ± 0.001
				$Se\text{-}Al_1$	2.33 ± 0.04	1	0.005 ± 0.001
				$Se\text{-}Al_2$	3.16 ± 0.03	1	0.004 ± 0.002
				$Se\text{-}Al_3$	3.61 ± 0.03	1	0.005 ± 0.001
Se(VI)	4	0.90	11.50	Se-O	1.703 ± 0.003	4	0.001 ± 0.001
				$Se\text{-}Al_1$	2.26 ± 0.03	1	0.002 ± 0.001
				$Se\text{-}Al_2$	3.09 ± 0.06	1	0.004 ± 0.002
				$Se\text{-}Al_3$	3.52 ± 0.02	1	0.003 ± 0.001
Se(VI)	5	0.90	17.26	Se-O	1.689 ± 0.006	4	0.004 ± 0.002
on				$Se\text{-}Al_1$	2.35 ± 0.04	1	0.008 ± 0.003
biogenic				$Se\text{-}Al_2$	3.17 ± 0.02	1	0.004 ± 0.001
imogolite				$Se\text{-}Al_3$	3.69 ± 0.02	1	0.002 ± 0.002

* *All the coordination numbers have been fixed to their theoretical values (see Table 3).*

Table 4*. Interatomic distances (R), coordination numbers (N) and mean-square relative displacement (σ^2) obtained from EXAFS data analyses of selenate adsorbed of synthetic and biogenic imogolite.*

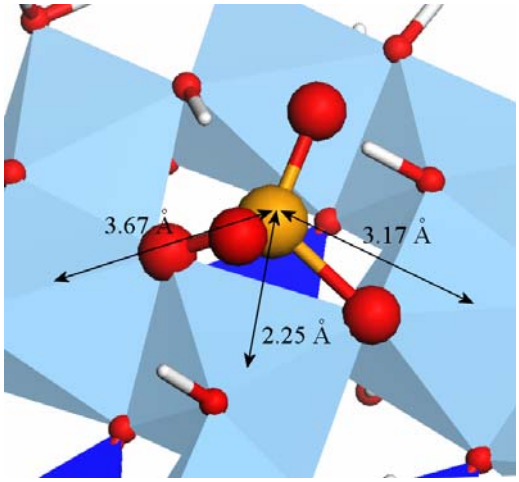


Figure 9*. View of the DFT-optimized inner-sphere selenate complex with the interatomic distances to aluminum atoms.*

The results of the fits are shown in Table 4 and in Figure 10. The three samples show very similar local structures that are in very good agreement with the optimized selenate complex. In the fits all the coordination numbers have been fixed to their theoretical values. Values of the Debye-Waller factors are higher than for selenite due to the effect of the temperature (selenate samples have been measured at room temperature). The fits are very stable, and the Debye-Waller factors relatively small, which indicates the goodness of the structural model used as input to analyze the data.

DISCUSSION

EXAFS analyses reveal the occurrence of inner-sphere complexes for both oxyanions and on both synthetic and biogenic imogolite samples. In the case of selenite, DFT simulations reveal the existence of a competition between water molecules and selenite ions for surface adsorption sites: the formation of a hydrogen bond between a water molecule and an oxygen atom participating in the complex strongly affects the symmetry of the complex, deforming the selenite molecule to an unphysical geometry. The occurrence of this adsorption site for water molecules at the surface of imogolite has been reported by some authors (Creton et al., 2008), (Fernández-Martínez *et al*., *in preparation*), who have indicated that these sites accept hydrogen bonds from water molecules, providing very stable adsorption sites with strong adsorption energies.

This same site for water adsorption has been reported to occur in the surface of gibbsite (Wang et al., 2006) with even higher adsorption energies for water than

imogolite (Fernández-Martínez *et al.*, *in preparation*). The adsorption of selenite molecules upon removal of these strongly adsorbed water molecules reveals a high specificity of the imogolite surface for the inner-sphere complexation (or chemisorption) of selenite molecules.

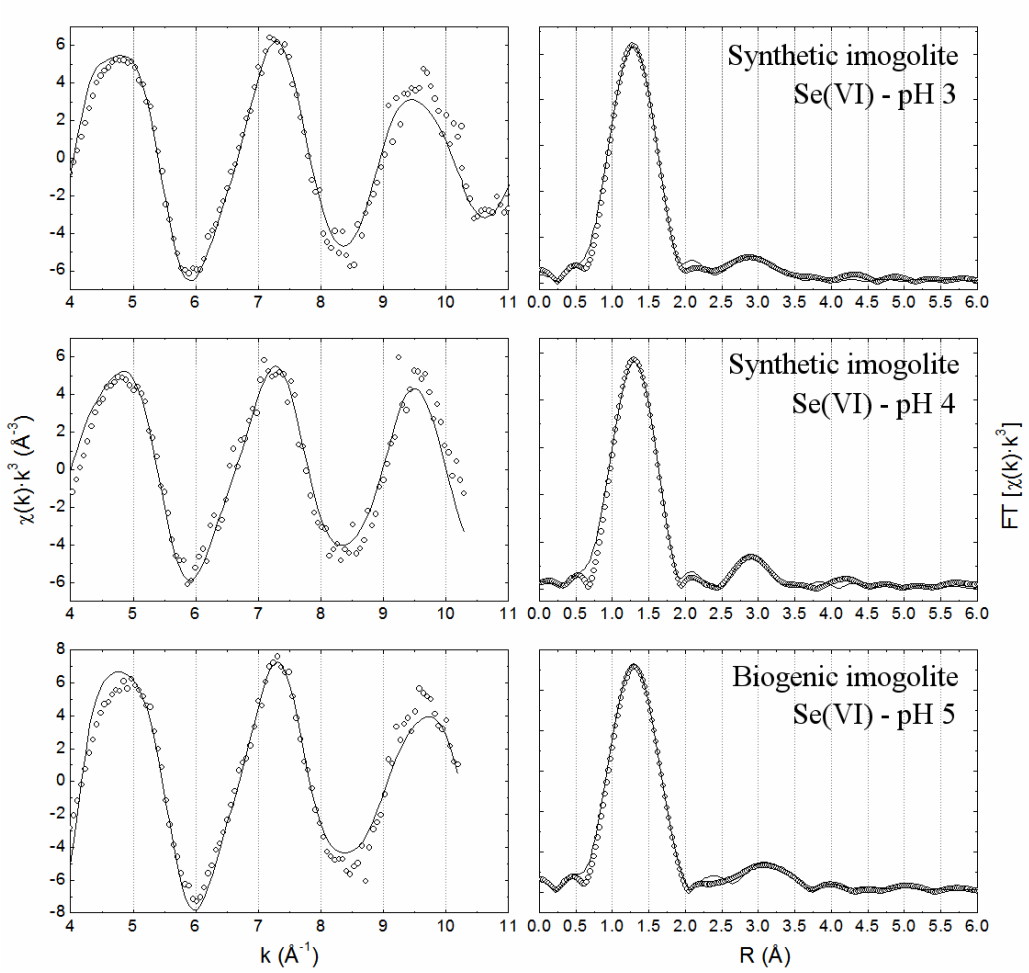


Figure 10. *EXAFS signals (left) and their Fourier transformations (RDFs, right) of selenate [Se(VI)] adsorbed on synthetic and biogenic imogolite. Experimental data are represented by points; fits by solid lines. The presence of a second shell can be clearly distinguished in the RDFs.*

The variability in the coordination number of the first shell indicates the possibility that the selenite molecules could be adsorbing over a vacant octahedral aluminum site. This hypothesis and the high pK_{a1} of singly coordinated $>AlOH_2^{+1/2}$ sites present on unsaturated oxygen atoms at vacancy sites (pK_{a1} = 10) would explain the development

of a surface charge at high solution pH values, as reported by electrophoretic measurements (Su and Harsh, 1993; Tsuchida et al., 2004).

In the case of selenate a similar inner-sphere complexation takes place. Both selenite and selenate have mononuclear bidentate ligands, making that an Al atom is relatively close to the selenium atom, at distances of d_{SeAl1} = 2.38 Å and d_{SeAl1} = 2.30 Å for selenite and selenate, respectively. These distances match very well the distances obtained from the DFT calculations. Some authors have reported short second shell distances for selenate complexes adsorbed on goethite (Manceau and Charlet, 1994). These authors discussed the plausibility of selenate ion pairing formation at the goethite surface, which would give a second shell formed by another selenium atom, indistinguishable by EXAFS from iron atoms. The authors denied this possibility, arguing that this formation of selenate ion pairs has never been observed neither in solution nor in the bulk of selenium compounds (Manceau and Charlet, 1994). In the case of selenite, the formation of diselenite groups is encountered in compounds containing transition metals as $VOSe_2O_5$ (Meunier et al., 1974), $CoSe_2O_5$ (Hawthorne et al., 1987) or $ZnSe_2O_5$ (Meunier and Bertaud, 1974). However, the existence of this ion pairing at the imogolite surface would give different EXAFS signals, as the EXAFS technique is sensitive enough to distinguish backscatterers as Al (Z = 13) and Se (Z = 34). This allows us disregarding the formation of ion pairs to explain the second shell observed in our calculations. On the other hand, the Se-Al distances observed in this study are much shorter than the distances observed between Se(VI) and Fe(III) atoms in selenate inner-sphere complexes on goethite, with $d_{Se\text{-}Fe}$ = 2.76 Å. This fact can be explained by the smaller ionic radius of the Al(III) ions (0.53 Å) in comparison to the ionic radius of Fe(III) (0.64 Å). The existence of this first shell of aluminum atoms seems then plausible from a structural point of view.

The formation of a structured shell of adsorbed water at mineral surfaces, especially on mineral surfaces populated by hydroxyl groups, has a high influence on the ion adsorption. Some authors have revealed that adsorbed water at the curved external surface of imogolite has a similar structure than on the planar surface of gibbsite (Creton et al., 2008). However, the curvature causes that adsorbed water on imogolite has lower adsorption energies and forms less structured shells of water. Peak *et al.* (2006) reported outer-sphere complexation of selenate ions at the Hydrous Aluminum Oxide (HAO) − water interface. The structure of the HAO surface is, in some way, similar to that of an 'amorphous' gibbsite, with alternation of single and doubly-

coordinate $>AlOH_2^{+1/2}$ and $>Al_2OH^0$ groups. (Papelis et al., 1995) reported outer-sphere complexation of selenate ions at the gibbsite surface. The ability of selenate to form inner-sphere complexes at the surface of imogolite reveals then differences in the surface chemistry between gibbsite and imogolite that could be related to the fact that water is less structured on the imogolite surface than on other planar hydroxylated aluminum oxide surfaces.

The formation of these complexes has a great relevance in the biogeochemical cycling of selenium in environments dominated by volcanic formations, where imogolite develops in the soils' clay fraction. The mobility of oxyanions like selenate and selenite is greatly influenced by the formation of complexes at mineral−water interfaces. The formation of inner-sphere complexes (chemisorbed molecules) is then a very important process controlling the concentration of selenium in soil solutions of volcanic soils, like andosols.

CONCLUSIONS

The combined use of molecular modeling and spectroscopic methods has allowed us to describe the formation of inner-sphere complexes of selenium oxyanions (selenate and selenite) at the surface of imogolite. DFT calculations of selenite complexes have revealed the important role played by water molecules in the stability of the complexes. The formation of a hydrogen-bond between a water molecule and a surface oxygen atom participating in the inner-sphere complex greatly affects the geometry of the selenite molecule, deforming it to unrealistic conformations. The fact that selenite forms strong complexes at the imogolite – water interface reveals the stronger affinity of imogolite for selenite, a specificity strong enough to be able to remove a water molecule prior to the formation of the complex.

The different behavior for the complexation of selenate at the gibbsite and imogolite − water interfaces (according to (Papelis *et al*., 1995) selenate forms outer-sphere complexes at the gibbsite – water interface) reveals the importance of the curvature on the surface chemistry of imogolite. Fernández-Martínez et al (in preparation, 2009) have shown that the shell of adsorbed water at the imogolite surface is less structured than at the surface of gibbsite, the orientations of the hydroxyl groups having an important effect on the imogolite adsorption properties of water. In addition, these authors have reported the formation of 'patches' or 'dry regions' at the imogolite and gibbsite

surfaces. Further studies on the influence of these patches on the adsorption of ions should be performed to clarify their role in interfacial phenomena.

Finally, the formation of selenium inner-sphere complexes at the imogolite – water interface is a very relevant finding which will help to clarify the geochemical cycling of selenium in volcanic soils. Inner-sphere complexes involve the formation of covalent bonds, and thus they are expected to reduce the mobility of selenium and its bioavailability to biota. More studies focusing on de-sorption and competition effects will help to better understand the importance of the complexes reported here over the selenium deficiency problems that are affecting volcanic regions.

ACKNOWLEDGEMENTS

Kideok K. Kwon (LBL, Berkeley, USA) is gratefully acknowledged for fruitful discussions about the DFT modeling of selenite complexes at the imogolite surface. Adéline Chabry is thanked for her technical assistance during a stage of 3 months performing selenium adsorption isotherms. Andre Rossberg and Harald Funke (BM20, ESRF, Grenoble, France) are acknowledged for their help with XAS spectra acquisition. A.F.-M. acknowledges the Région Rhône-Alpes for the finantial support received through an Explora'DOC fellowship for a 6-months stay at the University of California, Berkeley. G.R.-R. and L.C. acknowledge partial funding from E.U. Project AQUATRAIN.

REFERENCES

Alvarez-Ramirez, F. (2007) Ab initio simulation of the structural and electronic properties of aluminosilicate and aluminogermanate natotubes with imogolite-like structure. Physical Review B, 76(12).

Ankudinov, A.L., Bouldin, C.E., Rehr, J.J., Sims, J., and Hung, H. (2002) Parallel calculation of electron multiple scattering using Lanczos algorithms. Physical Review B, 65(10), 11.

Arai, Y., McBeath, M., Bargar, J.R., Joye, J., and Davis, J.A. (2006) Uranyl adsorption and surface speciation at the imogolite-water interface: Self-consistent spectroscopic and surface complexation models. Geochimica et Cosmochimica Acta, 70(10), 2492-2509.

Balistrieri, L.S., and Chao, T.T. (1987) Selenium Adsorption by Goethite. Soil Science Society of America Journal, 51(5), 1145-1151.

Bickmore, B.R., Tadanier, C.J., Rosso, K.M., Monn, W.D., and Eggett, D.L. (2004) Bond-Valence methods for pK(a) prediction: critical reanalysis and a new approach. Geochimica et Cosmochimica Acta, 68(9), 2025-2042.

Boyle-Wight, E.J., Katz, L.E., and Hayes, K.F. (2002) Spectroscopic studies of the effects of selenate and selenite on cobalt sorption to gamma-Al2O3. Environmental Science & Technology, 36(6), 1219-1225.

Brinker, C.J., and Scherer, G.W. (1990) Sol-gel Science: The Physics and Chemistry of Sol-Gel Processing. Academic Press, Inc., New York.

Bursill, L.A., Peng, J.L., and Bourgeois, L.N. (2000) Imogolite: an aluminosilicate nanotube material. Philosophical Magazine a-Physics of Condensed Matter Structure Defects and Mechanical Properties, 80(1), 105-117.

Byers, H.G., Miller, J.T., Williams, K.T., and Lakin, H.W. (1938) Selenium occurrence in certain soils in the United States with a discussion of related topics. Third Report U.S.D.A. Tech. Bul. 601., US.

Catalano, J.G., Zhang, Z., Fenter, P., and Bedzyk, M.J. (2006) Inner-sphere adsorption geometry of Se(IV) at the hematite (100)-water interface. Journal of Colloid and Interface Science, 297(2), 665-671.

Charlet, L., Scheinost, A.C., Tournassat, C., Greneche, J.M., Gehin, A., Fernandez-Martinez, A., Coudert, S., Tisserand, D., and Brendle, J. (2007) Electron transfer at the mineral/water interface: Selenium reduction by ferrous iron sorbed on clay. Geochimica Et Cosmochimica Acta, 71(23), 5731-5749.

Cradwick, P.D., Wada, K., Russell, J.D., Yoshinag.N, Masson, C.R., and Farmer, V.C. (1972) Imogolite, a hydrated aluminum silicate of tubular structure. Nature-Physical Science, 240(104), 187-&.

Creton, B., Bougeard, D., Smirnov, K.S., Guilment, J., and Poncelet, O. (2008) Molecular dynamics study of hydrated imogolite - 2. Structure and dynamics of confined water. Physical Chemistry Chemical Physics, 10(32), 4879-4888.

Dahlgren, R.A., and Ugolini, F.C. (1989) Formation and stability of imogolite in a tephritic spodosol, Cascade Range, Washington, USA. Geochimica et Cosmochimica Acta, 53(8), 1897-1904.

Davidson, D.F., and Powers, H.A. (1959) Selenium content of some volcanic rocks from Western United States and Hawaiian Islands. Bulletin of the Geological Survey of U.S., 1084-C, 69-81.

Davis, J.A., and Leckie, J.O. (1980) Surface-Ionization and Complexation at the Oxide-Water Interface .3. Adsorption of Anions. Journal of Colloid and Interface Science, 74(1), 32-43.

Delley, B. (1990) An all-electron numerical method for solving the local density functional for polyatomic molecules. Journal of Chemical Physics, 92(1), 508-517.

-. (2000) From molecules to solids with the DMol(3) approach. Journal of Chemical Physics, 113(18), 7756-7764.

Denaix, L., Lamy, I., and Bottero, J.Y. (1999) Structure and affinity towards Cd2+, Cu2+, Pb2+ of synthetic colloidal amorphous aluminosilicates and their precursors. Colloids and Surfaces a-Physicochemical and Engineering Aspects, 158(3), 315-325.

Dhillon, S.K., and Dhillon, K.S. (2000) Selenium adsorption in soils as influenced by different anions. Journal of Plant Nutrition and Soil Science-Zeitschrift Fur Pflanzenernahrung Und Bodenkunde, 163(6), 577-582.

Donkai, N., Hoshino, H., Kajiwara, K., and Miyamoto, T. (1993) Lyotropic mesophase of imogolite. 3. Observation of liquid-crystal structure by scanning electron and novel polarized optical microscopy. Makromolekulare Chemie-Macromolecular Chemistry and Physics, 194(2), 559-580.

Duc, M., Lefevre, G., Fedoroff, M., Jeanjean, J., Rouchaud, J.C., Monteil-Rivera, F., Dumonceau, J., and Milonjic, S. (2003) Sorption of selenium anionic species on apatites and iron oxides from aqueous solutions. Journal of Environmental Radioactivity, 70(1-2), 61-72.

Farmer, V.C., Adams, M.J., Fraser, A.R., and Palmieri, F. (1983) Synthetic imogolite - Properties, synthesis and possible applications. Clay Minerals, 18(4), 459-472.

Farmer, V.C., Fraser, A.R., and Tait, J.M. (1979) Characterization of the chemical structures of natural and synthetic aluminosilicate gels and sols by infrared spectroscopy. Geochimica et Cosmochimica Acta, 43(9), 1417-1420.

Foster, A.L., Brown, G.E., and Parks, G.A. (2003) X-ray absorption fine structure study of As(V) and Se(IV) sorption complexes on hydrous Mn oxides. Geochimica et Cosmochimica Acta, 67(11), 1937-1953.

Fukushi, K., and Sverjensky, D.A. (2007) A surface complexation model for sulfate and selenate on iron oxides consistent with spectroscopic and theoretical molecular evidence. Geochimica Et Cosmochimica Acta, 71(1), 1-24.

Gan, Y., and Franks, G.V. (2006) Charging behavior of the Gibbsite basal (001) surface in NaCl solution investigated by AFM colloidal probe technique. Langmuir, 22(14), 6087-6092.

Gu, B.Q., Cheng, T. O. (1987) The International Textbook of Cardiology. 14 p. Pergamon, New York.

Guimaraes, L., Enyashin, A.N., Frenzel, J., Heine, T., Duarte, H.A., and Seifert, G. (2007) Imogolite nanotubes: Stability, electronic, and mechanical properties. Acs Nano, 1(4), 362-368.

Gustafsson, J.P. (2001) The surface chemistry of imogolite. Clays and Clay Minerals, 49(1), 73-80.

Hansmann, D.D., and Anderson, M.A. (1985) Using Electrophoresis in Modeling Sulfate, Selenite, and Phosphate Adsorption onto Goethite. Environmental Science & Technology, 19(6), 544-551.

Hawthorne, F.C., Groat, L.A., and Ercit, T.S. (1987) Structure of a cobalt diselenite. Acta Crystallographica Section C-Crystal Structure Communications, 43, 2042-2044.

Hayes, K.F., Papelis, C., and Leckie, J.O. (1988) Modeling Ionic-Strength Effects on Anion Adsorption at Hydrous Oxide Solution Interfaces. Journal of Colloid and Interface Science, 125(2), 717-726.

Hayes, K.F., Roe, A.L., Brown, G.E., Hodgson, K.O., Leckie, J.O., and Parks, G.A. (1987) *In-situ* X-Ray Absorption Study of Surface Complexes - Selenium Oxyanions on Alpha-FeOOH. Science, 238(4828), 783-786.

Henmi, T., Tange, K., Minagawa, T., and Yoshinaga, N. (1981) Effect of SiO_2.Al_2O_3 ratio on the thermal reactions of allophane. 2. Infrared and X-ray powder diffraction data. Clays and Clay Minerals, 29(2), 124-128.

Hiemstra, T., Rietra, R., and Van Riemsdijk, W.H. (2007) Surface complexation of selenite on goethite: MO/DFT geometry and charge distribution. Croatica Chemica Acta, 80(3-4), 313-324.

Hiemstra, T., and Van Riemsdijk, W.H. (1999) Surface structural ion adsorption modeling of competitive binding of oxyanions by metal (hydr)oxides. Journal of Colloid and Interface Science, 210(1), 182-193.

Hiemstra, T., Venema, P., and VanRiemsdijk, W.H. (1996) Intrinsic proton affinity of reactive surface groups of metal (hydr)oxides: The bond valence principle. Journal of Colloid and Interface Science, 184(2), 680-692.

Ihnat, M. (1989) Occurence and distribution of Selenium. 354 p. CRC Press, Boca Raton, Florida.

John, M.K., Saunders, W.M.H., and Watkinson, J.H. (1975) Selenium adsorption by New Zealand soils. I. Relative adsorption of selenite by representative soils and their relationship to soil properties. New Zealand Journal of Agricultural Research, 19, 143-151.

Kohrle, J., Brigelius-Flohe, R., Bock, A., Gartner, R., Meyer, O., and Flohe, L. (2000) Selenium in biology: Facts and medical perspectives. Biological Chemistry, 381(9-10), 849-864.

Kubicki, J.D., Kwon, K.D., Paul, K.W., and Sparks, D.L. (2007) Surface complex structures modelled with quantum chemical calculations: carbonate, phosphate, sulphate, arsenate and arsenite. European Journal of Soil Science, 58(4), 932-944.

Lakin, H.W. (1972) Selenium Accumulation in Soils and Its Absorption by Plants and Animals. Geological Society of America Bulletin, 83(1), 181-189.

Lo, S.L., and Chen, T.Y. (1997) Adsorption of Se(IV) and Se(VI) on an iron-coated sand from water. Chemosphere, 35(5), 919-930.

Manceau, A., and Charlet, L. (1994) The Mechanism of Selenate Adsorption on Goethite and Hydrous Ferric-Oxide. Journal of Colloid and Interface Science, 168(1), 87-93.

Meunier, G., and Bertaud, M. (1974) Crystal chemistry of selenium (+IV). 2. Crystal structure of $ZnSe_2O_5$. Acta Crystallographica Section B-Structural Science, B 30(DEC15), 2840-2843.

Meunier, G., Bertaud, M., and Galy, J. (1974) Crystal chemistry of selenium (+IV) .1. VSe_2O_6, a structure with 3 independent $(VO_5)_{6N-N}$ parallel strings connected by $(Se_2O)^{6+}$ groups. Acta Crystallographica Section B-Structural Science, B 30(DEC15), 2834-2839.

Moreno-Reyes, R., Suetens, C., Mathieu, F., Begaux, F., Zhu, D., Rivera, M.T., Boelaert, M., Neve, J., Perlmutter, N., and Vanderpas, J. (1998) Kashin-Beck osteoarthropathy in rural Tibet in relation to selenium and iodine status. New England Journal of Medicine, 339(16), 1112-1120.

Morris, R.E., Harrison, W.T.A., Stucky, G.D., and Cheetham, A.K. (1992) On the structure of $Al_2(SeO_3)_3$ $6H_2O$. Journal of Solid State Chemistry, 99(1), 200-200.

Nakamaru, Y., Tagami, K., and Uchida, S. (2005) Distribution coefficient of selenium in Japanese agricultural soils. Chemosphere, 58(10), 1347-1354.

Neal, R.H., Sposito, G., Holtzclaw, K.M., and Traina, S.J. (1987a) Selenite Adsorption on Alluvial Soils .1. Soil Composition and Ph Effects. Soil Science Society of America Journal, 51(5), 1161-1165.

-. (1987b) Selenite Adsorption on Alluvial Soils .2. Solution Composition Effects. Soil Science Society of America Journal, 51(5), 1165-1169.

Papelis, C., Brown, G.E., Parks, G.A., and Leckie, J.O. (1995) X-Ray-Absorption Spectroscopic Studies of Cadmium and Selenite Adsorption on Aluminum-Oxides. Langmuir, 11(6), 2041-2048.

Parfitt, R.L., Furkert, R.J., and Henmi, T. (1980) Identification and structure of two types of allophane from volcanic ash soils and tephra. Clays and Clay Minerals, 28(5), 328-334.

Parida, K.M., Gorai, B., Das, N.N., and Rao, S.B. (1997) Studies on ferric oxide hydroxides .3. Adsorption of selenite (SeO_3^{2-}) on different forms of iron oxyhydroxides. Journal of Colloid and Interface Science, 185(2), 355-362.

Peak, D. (2006) Adsorption mechanisms of selenium oxyanions at the aluminum oxide/water interface. Journal of Colloid and Interface Science, 303(2), 337-345.

Peak, D., and Sparks, D.L. (2002) Mechanisms of selenate adsorption on iron oxides and hydroxides. Environmental Science & Technology, 36(7), 1460-1466.

Perdew, J.P., Burke, K., and Ernzerhof, M. (1996) Generalized gradient approximation made simple. Physical Review Letters, 77(18), 3865-3868.

Perdew, J.P., and Wang, Y. (1992) Accurate and simple analytic representation of the electron-gas correlation energy. Physical Review B, 45(23), 13244-13249.

Proux, O., Biquard, X., Lahera, E., Menthonnex, J.J., Prat, A., Ulrich, O., Soldo, Y., Trevisson, P., Kapoujyan, G., Perroux, G., Taunier, P., Grand, D., Jeantet, P., Deleglise, M., Roux, J.P., and Hazemann, J.L. (2005) FAME: A new beamline for X-ray absorption investigations of very-diluted systems of environmental, material and biological interests. Physica Scripta, T115, 970-973.

Rayman, M.P. (2000) The importance of selenium to human health. Lancet, 356(9225), 233-241.

Reilly, C. (1997) Selenium in food and health. 360 p. Blackie Academic & Professional, London.

Ressler, T. (1998) WinXAS: a program for X-ray absorption spectroscopy data analysis under MS-Windows. Journal of Synchrotron Radiation, 5, 118-122.

Schulthess, C.P., and Hu, Z.Q. (2001) Impact of chloride anions on proton and selenium adsorption by an aluminum oxide. Soil Science Society of America Journal, 65(3), 710-718.

Schwarz, K., and Foltz, C.M. (1957) Selenium as an integral part of Factor 3 against dietary necrotic liver degeneration. Soc, 79, 3292-3293.

Selim, H.M., and Sparks, D. (2001) Heavy metals release in soils. 264 p. CRC Press, Boca Raton, FL.

Sirichakwal, P.P., Puwastien, P., Polngam, J., and Kongkachuichai, R. (2005) Selenium content of Thai foods. Journal of Food Composition and Analysis, 18(1), 47-59.

Sposito, G. (2004) The surface chemistry of natural particles. 242 p. Oxford University Press, New York.

Stone, R. (2009) A Medical Mystery in Middle China. Science, 324(5933), 1378-1381.

Su, C.M., and Harsh, J.B. (1993) The electrophoretic mobility of imogolite and allophane in the presence of inorganic anions and citrate. Clays and Clay Minerals, 41(4), 461-471.

Su, C.M., and Suarez, D.L. (2000) Selenate and selenite sorption on iron oxides: An infrared and electrophoretic study. Soil Science Society of America Journal, 64(1), 101-111.

Tazaki, K., Morikawa, T., Watanabe, H., Asada, R., and Okuno, M. (2006) Microbial formation of imogolite. Clay Science, 12(Supplement 2), 245-254.

Tsuchida, H., Ooi, S., Nakaishi, K., and Adachi, Y. (2004) Effects of pH and ionic strength on electrokinetic properties of imogolite. 3rd International Conference on Interfaces Against Pollutions, p. 131-134, Julich, GERMANY.

Ugolini, F.C., and Dahlgren, R.A. (1991) Weathering environments and occurrence of imogolite and allophane in selected andisols and spodosols. Soil Science Society of America Journal, 55(4), 1166-1171.

Vandergaast, S.J., Wada, K., Wada, S.I., and Kakuto, Y. (1985) Small-angle X-ray powder diffraction, morphology and structure of allophane and imogolite. Clays and Clay Minerals, 33(3), 237-243.

Wada, K. (1989) Allophane and imogolite. In J.B. Dixon, and S.B. Weed, Eds. Minerals in soil environments, p. 1051-1087.

Wang, C., McKeague, J.A., and Kodama, H. (1986) Pedogenic imogolite and soils environments - Case study of spodosols in Quebec, Canada. Soil Science Society of America Journal, 50(3), 711-718.

Wang, J.W., Kalinichev, A.G., and Kirkpatrick, R.J. (2006) Effects of substrate structure and composition on the structure, dynamics, and energetics of water at mineral surfaces: A molecular dynamics modeling study. Geochimica et Cosmochimica Acta, 70(3), 562-582.

Wang, L.M., and Zhang, J.S. (2002) Ab initio calculation on thermochemistry of CH3SOxH (x=1-3) and H2SOy (y=2,3). Journal of Molecular Structure-Theochem, 581, 129-138.

Wang, M.C., and Chen, H.M. (2003) Forms and distribution of selenium at different depths and among particle size fractions of three Taiwan soils. Chemosphere, 52(3), 585-593.

Wang, Z.J., and Gao, Y.X. (2001) Biogeochemical cycling of selenium in Chinese environments. Applied Geochemistry, 16(11-12), 1345-1351.

Wijnja, H., and Schulthess, C.P. (2000) Vibrational spectroscopy study of selenate and sulfate adsorption mechanisms on Fe and Al (hydr)oxide surfaces. Journal of Colloid and Interface Science, 229(1), 286-297.

Yu, T.R. (1997) Chemistry of variable charge soils. 520 p. Oxford University Press, New York.

Zhang, P.C., and Sparks, D.L. (1990) Kinetics of Selenate and Selenite Adsorption Desorption at the Goethite Water Interface. Environmental Science & Technology, 24(12), 1848-1856.

Chapter 4

Molecular dynamics investigation of the structure of water at the imogolite and gibbsite – water interfaces: effect of the curvature on the hydrophilicity and surface acidity

4.1.- Introduction

Adsorption at mineral surfaces plays an important role in both agricultural and environmental science because many reactions between soils and aqueous solutions, and all reactions between rocks and aqueous solutions, involve mineral surfaces. These reactions affect life-sustaining processes such as plant nutrition and growth, as well as life-threatening processes such as contaminant transport. As a result, soil science and environmental science require an accurate knowledge of mineral surface adsorption behavior in order to understand processes important to the well-being of our environment and the development of our resources. The modeling of adsorption processes at mineral-water interfaces is done using Surface Complexation Models (SCMs) (Hiemstra et al., 1989; Hiemstra and VanRiemsdijk, 1996; Sposito, 2004). These models are helpful for understanding the behavior of adsorption in a qualitative way, but most of them present some important drawbacks: (1) usually, there are too many adjustable parameters in the models, such as the number of surface sites, the Helmholtz layer capacitances or the surface acidity constants and (2) most of these models are macroscopic in nature, and thus do not take into account the 'molecularity' of the mineral surfaces. For instance, macroscopic assumptions considering mineral surfaces as flat charged planes with only one type of adsorption site are usually made, an assumption that is far from the actual atomic-scale roughness of a mineral surface (Sposito, 2004). A great leap ahead in this field was the development by Hiemstra et al. of the MUSIC model, a multi-site SCM in which the surface acidity constants are

calculated using a bond-valence approach based on a structural description of the surface sites (Brown, 2002; Hiemstra et al., 1989; Hiemstra and VanRiemsdijk, 1996). This model accounts for differences on the surface density of adsorption sites of different faces of minerals. The CD-MUSIC model, a variation of the original one, includes the effects of hydrogen bonding on the charge saturation of each particular site (Hiemstra and VanRiemsdijk, 1996). It is thus a SCM that provides more molecular scale detail than the previous ones (Davis et al., 1978). Furthermore, the advent of new spectroscopic techniques enable the mineral/water interface to be described with atomic resolution and the development of powerful computational methods as the Density Functional Theory, allow constraining some parameters used in SCMs using structural considerations (Machesky et al., 2008; Villalobos et al., 2009).

However, while these models and spectroscopic techniques have been widely applied to the study of crystalline minerals, more difficulties are associated with the study of minerals with crystallite sizes in the nanoscale. The small coherent domains of these nanoparticles make difficult the application of conventional diffraction techniques to their study. Their high surface-to-bulk ratios, with surfaces dominated in some cases by relaxation effects prevent the use of scattering techniques like X-ray reflectivity or X-ray standing waves, that have been demonstrated as very powerful in the study of densities of water and adsorbed ions above well-crystallized, planar mineral surfaces like those of mica, calcite, rutile or quartz (Catalano et al., 2009; Fenter et al., 2006a; Fenter et al., 2008; Fenter et al., 2006b; Fenter and Sturchio, 2004; Geissbuhler et al., 2004; Zhang et al., 2004). As described in the previous chapter, imogolite is a nanocrystalline aluminosilicate with a nanotubular shape that falls in the category of nanoscale minerals. For these reasons, when modeling the adsorption behavior of the external face of imogolite, authors who have developed SCMs have made use of geochemical parameters corresponding to the (001) gibbsite face, which is the imogolite's planar equivalent (Arai et al., 2006; Gustafsson, 2001). Gibbsite, $Al(OH)_3$, is ubiquitous in soil environments and has a large specific surface area, which gives it a high potential as an adsorbent of ions (Sposito, 2008). It is a platy, pseudo-hexagonal mineral dominated by a basal (001) plane and two edge (100) and (110) crystal faces. The surface (001) face of gibbsite is dominated by doubly-coordinated neutral aluminol groups ($>Al_2OH^0$) at a surface density of 13.7 nm^{-2}. The edge faces have singly coordinated $>AlOH^{-1/2}$ groups, at a surface density of 8.1 nm^{-2} (Saalfeld and Wedde,

1974). The protonation constant of these functional groups is the key parameter controlling the adsorption of ions at the gibbsite – water interface, as it determines the development of charge as a function of the pH of the soil solution.

The accurate determination of surface acidity constants is a difficult task. Titration experiments have been routinely used to obtain surface pK_a values during the last 30 years (Schindler and Stumm, 1987). The use of new spectroscopic methods as a complement to titration experiments, as the one described by Gan *et al.* (2006), are only applicable to the study of mineral surfaces with no defects and relatively large surfaces (in the order of the μm^2). Regarding the (001) surface of gibbsite, Hiemstra *et al.* (1996) developed a MUSIC model reporting values for the first (pK_{a1}) and second (pK_{a2}) protonation constants of the (001) surface sites of 0 and 11.9 log units respectively. More recently other authors have applied *ab-initio* Molecular Dynamics combined with a bond-valence analysis to the study of intrinsic protonation constants (Bickmore et al., 2006; Bickmore et al., 2004). It is known that values for the intrinsic pK_a of surface groups have different values than for their corresponding aqueous species (Schindler and Stumm, 1987). Bickmore *et al.* (2004) have shown that these variations are strongly influenced by relaxation effects at the surface due to protonation or de-protonation processes, which affect the pK_a of the surrounding sites in a strong and non-linear way, the differences being of several log units (Bickmore et al., 2004). These authors reported several values for the protonation constant of neutral aluminol sites, with one of them ($pK_{a1} = 5.2$) in a pH range of environmental relevance, and very similar to the experimental value of $pK_{a1} = 5.9 \pm 0.2$ reported by Gan *et al*. (2006) (see Table 4.1).

In the case of imogolite, no study has yet been reported determining values of the protonation constants. In addition, the big size of the imogolite unit cell prevents the use of *ab-initio* Molecular Dynamics techniques that could be applied in the same way as Bickmore *et al*. (2004) did for the surface of gibbsite. For this reason we have chosen to use classical MD to study the hydrated surfaces of gibbsite and imogolite, and to evaluate the effect that the curvature of the imogolite surface has over the structure and energetics of adsorbed water. The results of classical MD simulations rely on the quality of the force-field used to describe the Hamiltonian of the system.

Reaction	**pK_a**	**Reference**
$>Al_2OH_2^+ \leftrightarrow >Al_2OH^0 + H^+$	0	Hiemstra *et al.* (1996)
	5.2	Bickmore *et al*. (2004)
	10.8	
	-1.6	
	-0.4	
	2.3	
	-5.1	
	5.9 ± 0.2	Gan *et al.* (2006)
$>Al_2OH_2^+ + Cl^- \leftrightarrow >Al_2OH + H^+ + Cl^-$	**8.49 ± 0.01**	Rosenqvist *et al.* (2002)
$>Al_2O^-Na^+ + H^+ \leftrightarrow >Al_2OH^0 + Na^+$	-9.62 ± 0.01	

Table 4.1. Reported values for the first protonation constant of doubly coordinated neutral sites at the gibbsite – water interface. Values falling in a pH range of environmental relevance are highlighted in bold. The values reported by Rosenqvist *et al.* (2002) correspond to a reaction involving complexation of electrolyte ions, Na^+ and Cl^- (Rosenqvist et al., 2002).

In this case, we will use a force-field that has been calibrated for bulk systems (gibbsite being one of them) and for bulk water (Cygan et al., 2004). For this reason, we do not attempt to extract absolute values of the protonation constants, but to evaluate the relative values of these constants in the cases of a planar system (gibbsite) and a cylindrical system (imogolite). The lack of accuracy of the force-field used becomes then less important, as the systematic errors will affect equally the results obtained for both systems. Simulations will be used to obtain the number of hydrogen bonds per surface adsorption site, a parameter that is usually fitted in the SCMs, and that will be used as an input in a CD-MUSIC model of both surfaces. 'Patching' effects of water on both surfaces will be described and their relevance evaluated in terms of hydrophobicity and surface chemistry.

Water structure and hydration properties of imogolite: 'The nanotube effect'

A. Fernández-Martínez[1,2,3], I. C. Bourg[4], G. J. Cuello[2,5], M. R. Johnson[2], G. Sposito[3,4] and L. Charlet[1,3]

[1] *Equipe de Geochimie de l'Environnement, LGIT, University of Grenoble and CNRS. B.P. 53, 38041 Grenoble, France.*

[2] *Institut Laue-Langevin. B.P. 156, 38042 Grenoble, France.*

[3] *Environmental Science Policy and Management Department, University of California, Berkeley, CA 94720-3114, USA*

[4] *Geochemistry Department, Lawrence Berkeley National Laboratory, Berkeley, CA 94720, USA*

[5] *Ikerbasque & Department of Applied Physics II, Faculty of Sciences, Basque Country University, 48080 Bilbao, Spain*

To be submitted to Journal of Physical Chemistry C

ABSTRACT

The effect of the curvature of two mineral surfaces with the same composition −the external surface of imogolite and the (001) surface of gibbsite− on their surface chemistry has been explored comparing a curved surface –imogolite– with a planar one –gibbsite–. MD simulations have shown that water molecules adsorb on both surfaces adopting similar orientations. However, the curvature of the imogolite surface prevents the formation of some H-bonds between surface OH groups, preventing the adsorption of A-type water molecules, which are strongly adsorbed at the surface of gibbsite. These differences in H-bonding affect the hydrophilicity of both mineral surfaces, making the imogolite surface more hydrophobic, with a minimum in the enthalpy of water adsorption shifted by $\Delta\Delta G$ = +2.19 kcal/mol with respect to gibbsite. The different arrangement of surface H-bonds affects the bond valences of surface oxygen atoms due to H-bonds with water molecules, which results in a shift of the imogolite $>Al_2OH_2^+$ pK_{a1} of almost one log unit towards acidic values.

INTRODUCTION

Imogolite ($Al_2(OH)_3SiO_3OH$) is an aluminosilicate mineral commonly found in soil environments such as the clay fractions of volcanic ash soils or spodosols (Dahlgren and Ugolini, 1989; Dahlgren and Ugolini, 1991; Ugolini and Dahlgren, 1991; Wang et al., 1986). Imogolite has a nanotubular geometry, with an internal face dominated by silanol ($>SiOH^0$) functional groups and an external face composed by a curved gibbsite ($Al(OH)_3$), with neutral aluminol groups ($>Al_2OH^0$) on its surface (see Figure 1). The nanotubes are highly anisotropic, with diameters of $d_i \approx 1$nm (internal) and $d_e \approx 2.2$nm (external), and lengths in the order of the micrometer (Wada and Yoshinaga, 1969). The presence of amphoteric surfaces and the lack of isomorphic substitutions (which would act as centers of permanent charge) make imogolite a mineral with a variable charge only dependent on the pH of the soil solution. Permanent charge at the imogolite surface has always been attributed to the presence of vacancies in its structure, although some authors have hypothesized a permanent charge that would be originated by the undersaturation of surface oxygen atoms due to the strain induced by the curvature (Alvarez-Ramirez, 2007; Guimaraes et al., 2007; Gustafsson, 2001).

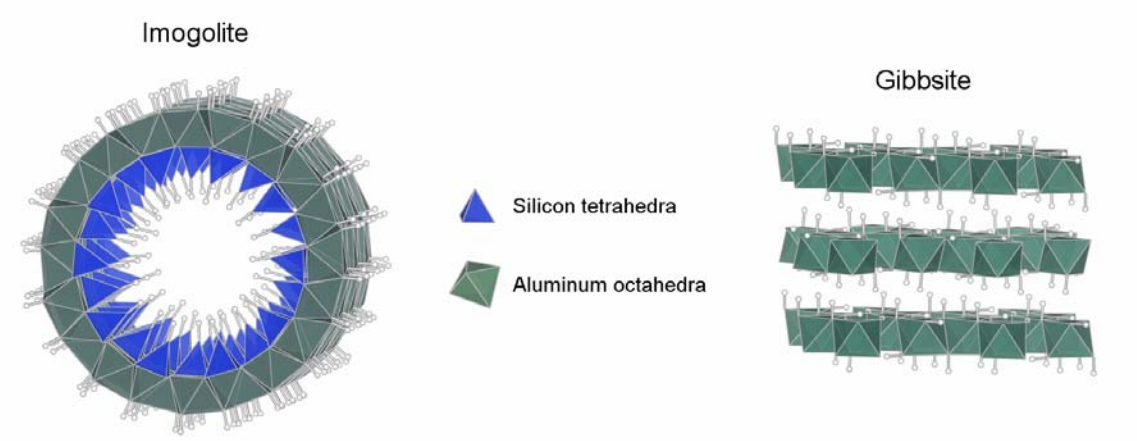


Figure 1*. View of the imogolite and gibbsite structures. The external surface of imogolite is a curved gibbsite layer. The (001) plane of gibbsite correspond to the basal plane of one layer. The white spheres are hydrogens from surface hydroxyl groups (OHs). The orientations of imogolite OHs have been chosen to be perpendicular to the surface. The orientations of gibbsite OHs are the same than in bulk gibbsite (Balan et al., 2006).*

Imogolite is an important component in the soils where it occurs. Its small size, with an external diameter of 2.2 nm and tube lengths in the order of the micrometer, and its poor crystallinity give it large specific surface areas. Some studies have highlighted the

relevance of imogolite and allophane (another nano-crystalline aluminosilicate) in the transfer of metallic cations in soil profiles (Abdelfattah and Wada, 1981; Levard et al., 2009; Rahman et al., 1996). This transfer is controlled by different processes, like the adsorption of ions at the mineral/water interfaces (Sposito, 2004), which is usually described in terms of surface complexation models (SCMs). To date, only a few studies have applied SCMs to the study of ion adsorption at the imogolite/water interface: Arai *et al*. developed a Triple Layer Model (TLM) to explain the complexation of uranyl at the external imogolite surface (Arai et al., 2006). However, these authors used the acidity constants for gibbsite's aluminol groups reported by Sverjensky (Sverjensky, 2005), assuming that, in terms of surface chemistry, imogolite would behave equally to gibbsite. Gustaffson developed a MUSIC model in which he introduced a permanent charge (Gustafsson, 2001), assuming that the number of hydrogen bonds between water and functional OH groups at the gibbsite and imogolite surfaces would be the same and would have identical arrangements. The number of H-bonds formed by a surface oxygen atom is a parameter usually fitted in SCMs, and with high influence in the calculation of the protonation constants of surface sites (Hiemstra and VanRiemsdijk, 1996). Some authors have used Molecular Dynamics (MD) simulations to constrain this number (Machesky et al., 2008). In this work, we have employed MD to ascertain the effect of hydrogen bonding on the protonation constants of surface hydroxyl groups at the surfaces of gibbsite and imogolite. This comparison is very interesting due to the same nature of the external imogolite and (001) gibbsite surfaces. The study of these two systems in parallel reveals the effect that the curvature has on the interactions of water with the mineral surface.

The hydrophilicity – hydrophobicity of a mineral surface has usually been related to the presence or not of a surface charge (Sposito et al., 1998), and determined experimentally by the measurement of contact angles (Abraham, 1978; Good, 1973; Prestidge and Ralston, 1995) or immersion techniques (Cantrell and Ewing, 2001; Michot et al., 1994) and theoretically by the determination of water density profiles or water contact angles (Cruz-Chu et al., 2006; Wang et al., 2006). Wang et al. determined the different degree of hydrophilicity – hydrophobicity of mineral surfaces through the study of water density profiles and hydration energies (Wang et al., 2006). They showed that hydrophobic mineral surfaces like talc act as 'hard-walls' (Abraham, 1978; Yu et al., 1999) or non-interacting barriers, the water density profiles showing different maxima at regular distances from the surface, indicative of the formation of a standing-

wave-like distribution of water. Siloxane surfaces present at basal planes of 2:1 clay minerals are an example of loosely-interacting mineral surfaces (Sposito et al., 1998), that would act as 'hard-walls' if they were isolated. However, the presence in clay minerals of a hydroxyl group at the center of the siloxane cavity, and bonded to the central octahedral sheet, affects the reactivity of siloxane cavities, which act as mild charge donors. Nevertheless, the main effect on the reactivity of these surfaces is due to the presence of isomorphic substitutions in the octahedral and tetrahedral sheets. These substitutions create a permanent negative charge, which makes possible the interaction of water with the mineral surface, creating a shell of adsorbed and ordered water. Another consequence of the presence of these isomorphic substitutions is the formation of cationic complexes adsorbed at the clay interlayer, and with adsorbed water shells that remain usually un-distorted. These cations contribute to create a hydrophilic environment in the clay interlayer, although, as noted before, the siloxane cavities are in principle hydrophobic.

Mineral surfaces populated by hydroxyl groups are more hydrophilic, even in the absence of isomorphic substitutions (Wang et al., 2006). Hydroxyl groups interact with water forming hydrogen-bonds, and in some cases providing very strong adsorption sites for the water molecules, which form highly structured layers. This is the case of imogolite and gibbsite surfaces. The internal surface of imogolite is dominated by silanol groups that, in conjunction with the small pore diameter, contribute to the formation of a very strong structure of water (Creton et al., 2008a). The external surface, similar to the (001) gibbsite surface, is expected to have a hydrophilic behavior as gibbsite does. As shown by Wang *et al.*, the structure and energetics of adsorbed water molecules are affected by the structure of mineral surfaces, being the positions and orientations of the hydroxyl groups the important parameters determining their relative hydrophilicity (Cruz-Chu et al., 2006; Wang et al., 2006). In this respect, little is known about the effect that the curvature of a mineral layer could have over the arrangement of surface hydroxyl groups.

The wetting of a mineral surface –its ability to maintain contact with water– strongly depends on the hydrophilicity of the mineral surface. This wetting ability has traditionally been considered as a property uniform over the surface. However, experimental results have shown heterogeneities in the wetting properties of some mineral surfaces. Beaglehole *et al.* determined using ellipsometry that water wets mica incompletely, arriving at a film thickness of between one and two nanometers at

saturation (Beaglehole and Christenson, 1992). They inferred a water coverage value of one statistical monolayer at 75% relative humidity. Similar 'patching' effects were described experimentally by other authors using infrared spectroscopy (Baltrusaitis et al., 2007; Goodman et al., 2001), sum frequency generation (Liu et al., 2005; Xu et al., 2006) or atomic force spectroscopy (Kendall and Martin, 2007) in other more complex mineral surfaces with such as SiO_2 or α-Al_2O_3. The occurrence of this patching effect at the (001) surface of gibbsite and at the imogolite external surface will be described in this work, and its effect on the calculation of the protonation constants discussed.

THEORETICAL METHODS

Molecular models of hydrated gibbsite and imogolite

Models for the gibbsite mineral/water interface were constructed by cleaving the gibbsite structure reported by Saalfeld and Wedde (Saalfeld and Wedde, 1974) along the (001) plane. A simulation box of 17.368 Å × 15.234 Å × 75 Å ($a \times b \times c$) containing two layers of gibbsite was used in all the calculations. Imogolite models were constructed from the structure obtained from Pair Distribution Function refinements. A simulation box of 50 Å × 50 Å × 25.29 Å containing three units of the imogolite nanotube along the *c* axis was used in all the simulations. A nanotube with ten molecular $Al_2(OH)_3SiO_3OH$ units along the circumference, similar to the reported structure of natural imogolite (Cradwick et al., 1972) was chosen.

The CLAYFF force-field was used in all the calculations. CLAYFF is an electrostatic force-field whose hamiltonian includes a 6-12 Lennard-Jones term to reproduce Van der Waals and short-range repulsion interactions, a bond stretching term for surface and water OH bonds and a three-body angular term to reproduce water angle bending modes (Cygan et al., 2004). CLAYFF has been successfully applied in studies of a variety of minerals (Cygan et al., 2009; Wander and Clark, 2008; Wang et al., 2006). Gibbsite was one of the minerals used for its parametrization, and thus its structure is reproduced with high accuracy, the difference with the experimental lattice constant being less than 4.1% (Wang et al., 2006). The structure of imogolite is also well reproduced as it is shown in the diffraction patterns generated from snapshots of the MD trajectories (not shown here).

CLAYFF uses a flexible SPC model to reproduce water interactions. This simple model has been extensively used to evaluate water structure and properties (Wang et al., 2006) and for the interaction of water with hydroxide mineral surfaces (Creton et al., 2008a; Creton et al., 2008b; Creton et al., 2008c; Cygan et al., 2009). As it will be shown later, the SPC model successfully reproduces the two adsorption sites for water molecules at the gibbsite (001) surface reported by Veilly *et al.* using DFT methods (Veilly et al., 2008). For this reason, and in spite of the lack of agreement between the values of some dynamic properties of SPC water and the experimental ones (Creton et al., 2008b), we think that the use of SPC water fits perfectly our requirements for the study of structural differences of adsorbed water at the imogolite and gibbsite interfaces with water.

Molecular dynamics (MD) simulations were carried out using the code LAMMPS (Plimpton, 1995). The dry models were first equilibrated during 50 ps using MD calculations in the canonical ensemble. Water was then loaded by means of Monte Carlo (MC) simulations in the canonical ensemble. MC simulations were performed using the Sorption module of Materials Studio 4.3 (Accelrys Inc.). One million MC steps were run to equilibrate the water molecules on the surface of the minerals. After loading, the hydrated structures were equilibrated during 500 ps using MD simulations. Production runs were performed in the canonical ensemble and MD simulations were run during 500 ps. All MD runs were performed on the NERSC supercomputer Franklin. MC runs were performed at the Linux cluster of the Computer for Science Group of the Institut Laue-Langevin. Analyses of the trajectories were performed using home-made codes written in Fortran 95.

The combination of MD and MC is very useful in the studies of mineral surfaces with surface OH functional groups. MC simulations allow the loading of water molecules on imogolite, where the positions of all the atoms (including the OHs) are fixed. This allows building a hydrated structure that is not far from an energy minimum. Using this MC equilibrated structure as the starting point MD simulations allow relaxing the positions and orientations of surface OHs, providing a method to stabilize the H-bonds formed between water molecules and the mineral surface.

Ab-initio geometrical optimizations of the hydrated structures (with one water layer) of imogolite and gibbsite were performed using the Vienna Ab-initio Simulation Package (VASP) (Kresse and Hafner, 1993; Kresse and Hafner, 1994). The imogolite model used in these *ab-initio* calculations consisted on one imogolite unit cell, with

dimensions 35 Å × 35 Å × 8.43 Å. A vacuum layer of 15 Å existed between the periodical images along the *a* and *b* directions, the tube being periodic along the *c* direction. A supercell of gibbsite containing 2 × 3 unit cells along the *a* and *b* directions (17.37 Å × 15.23 Å × 75 Å) and two layers of gibbsite (001) planes separated by a vacuum layer of 67 Å were used. The calculations were performed at the Gamma point ($k = 0$), using projector augmented wave (PAW) pseudopotentials (Kresse and Joubert, 1999) with a plane wave cutoff of 209 eV and the Perdew-Burke-Ernzerhof (PBE) functional of the generalized gradient approximation (GGA).

RESULTS AND DISCUSSION

Hydration energies

A series of calculations with different hydration levels were performed with the goal of examining possible differences between the hydrophilicity−hydrophobicity of the external face of imogolite and the (001) surface of gibbsite. For this purpose, only the external surface of imogolite was hydrated, and the internal pore was totally dry. The energy of water adsorption (ΔU_H) was calculated using the following expression (Smith, 1998):

$$\Delta U_H = \left[\langle U(N)\rangle - \langle U(0)\rangle\right] / N \quad (1)$$

where *U(N)* is the potential energy of the hydrated surface, *U(0)* is the potential energy of the dry surface and *N* is the number of water molecules. The average corresponds to a time average over all the production run. This method to calculate hydration energies has been successfully applied by Wang *et al.* (Wang et al., 2006) to study the energy of water adsorption on brucite, hydrotalcite, muscovite, talc and gibbsite. Their results for muscovite show a very good agreement with experimental values. These authors also discussed the non inclusion of the $P\Delta V$ term in the energy expression, arguing that these effects are very small at ambient pressures and thus can be safely neglected. Also, as it will be shown here, water is structured in similar ways on both surfaces. This fact has led us to make the assumption that entropic effects are playing a minor role here. We can thus make the approximation of equation (2) (Whitley and Smith, 2004):

$$\Delta S_1 = \Delta S_2 \quad (2)$$

$$\Delta\Delta G = \left(\Delta U_1 - T\Delta S_1\right) - \left(\Delta U_1 - T\Delta S_1\right) = \Delta U_1 - \Delta U_2 \quad (3)$$

In view of equations (2) and (3), the calculated increment in enthalpy of surface water adsorption would be equivalent to the Gibbs energy of surface water adsorption.

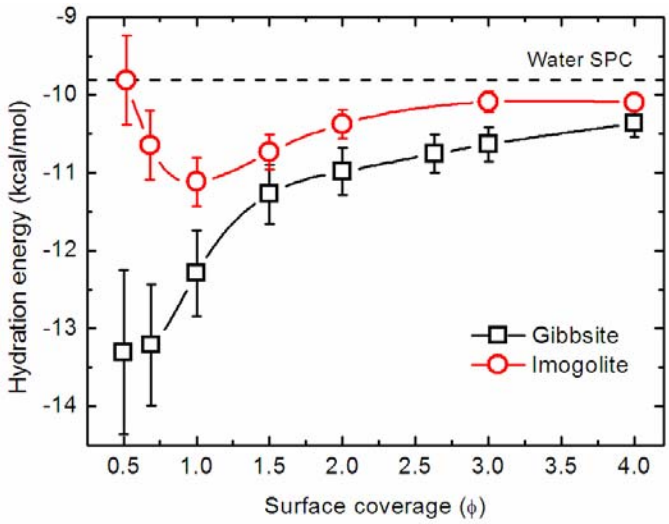


***Figure 2**. Hydration energies as a function of surface water coverage of the gibbsite (001) and imogolite external surfaces. The dotted line corresponds to the Gibbs free energy of a water molecule in SPC bulk water.*

The results are presented in Figure 2. The surface water coverage (ϕ) is defined as the ratio between the number of water molecules and the number of surface oxygen atoms. The constant (dashed line) at ΔU_H = -9.81 kcal/mol indicates the potential energy of a water molecule in bulk SPC water. The curves for the two minerals show a similar behavior: both show a minimum and tend asymptotically to the energy of bulk water at high surface coverage. The fact that both curves lie below the SPC water constant value of potential energy indicate that the surfaces are hydrophilic. The surface of gibbsite is more hydrophilic than the surface of imogolite, presenting a deeper minimum at ΔU_H = -13.30 kcal/mol, placed at a $\phi \approx 0.5$, the same values reported by Wang *et al*. (Wang et al., 2006). The hydration energy curve for imogolite has a minimum of ΔU_H = -11.11 kcal/mol placed at a surface coverage value of $\phi \approx 1$, higher than that of gibbsite. The difference in potential energy is significative, indicating that the surface of imogolite is more hydrophobic than the (001) surface of gibbsite. The occurrence of the minimum can be explained by considering the different interactions that a water molecule suffers when it is adsorbed at a mineral surface. At very low water coverages the water molecules interact uniquely with a surface OH, the interaction being very loose and far from the desired tetrahedral coordination that a water molecule

would adopt in bulk SPC water (Bernal and Fowler, 1933). For this reason, at the $\phi \rightarrow 0$ limit all the hydration curves tend to a value higher than the energy of SPC water. As more water is introduced into the system, small aggregates start to form around the adsorbed molecules, and the coordination of water molecules approaches in number and geometry the coordination of a water molecule in bulk water, lowering its potential energy. The same reasoning is valid for the surface of gibbsite. The difference between both surfaces comes then from their relative ability to form H-bonds with water. In order to explain this behavior and the relative hydrophobicity of imogolite compared to gibbsite, a structural analysis of the water H-bonding behavior to both surfaces will be presented in the next sections.

Orientation of surface OH groups

The projections of the O and H atoms onto the (001) surface of gibbsite and onto the external surface of imogolite are presented in Figure 3.

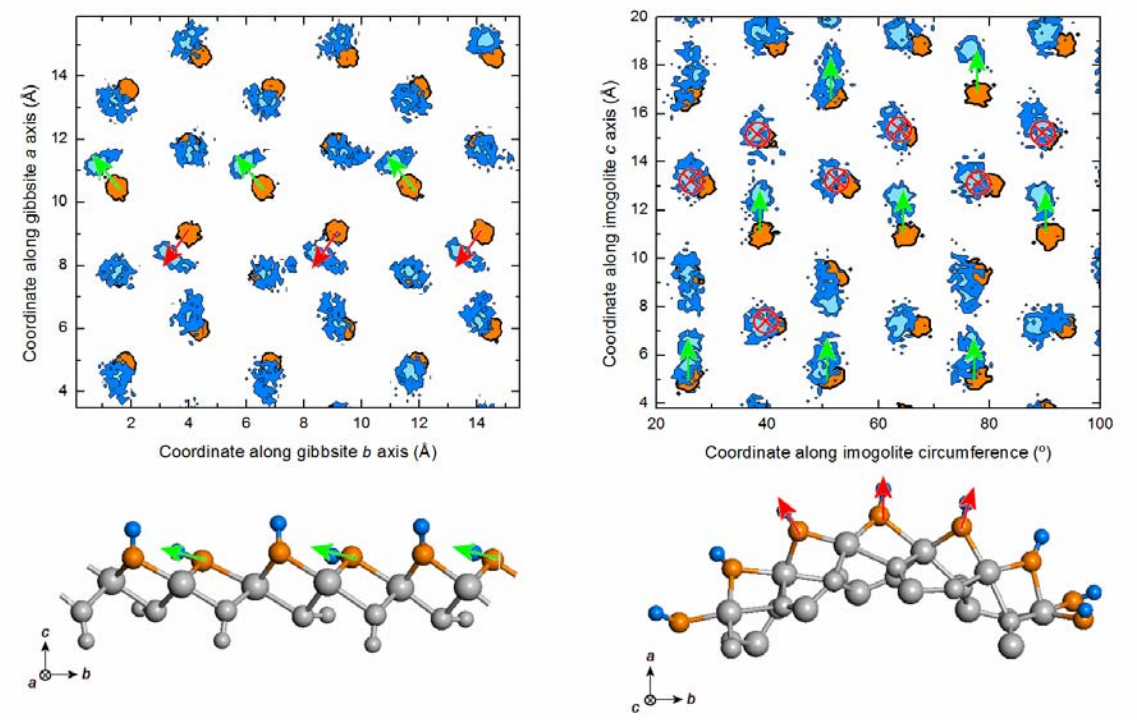


Figure 3. *Projections of surface OH groups onto the (001) gibbsite surface (left) and the external imogolite surface (right). The orange circles represent the positions of surface O atoms. The blue regions indicate the more probable positions for hydroxyl H atoms. Red arrows indicate OH groups perpendicular to the surface. Green arrows indicate OH groups parallel to*

the surface. The position of the empty octahedral site is placed between three O atoms, at the end of the green arrows in the left figure.

Two orientations for the OH groups are found on the (001) surface of gibbsite, which are similar to the orientations described in Wang *et al* (Wang et al., 2006): one in which 5/6 of the OH groups point towards the empty octahedral site of gibbsite (green and red arrows in the left of Figure 3) and another one in which 1/6 of the OH point perpendicularly to the (001) surface. On imogolite, the curvature prevents the formation of H-bonds between surface OH groups along the circumference of the nanotube.

Thus, only 1/3 of the OHs are parallel to the surface, with their direction lying along the *c* axis, where there is no curvature. As it will be shown in the next section, these different orientations of the OH groups cause differences in the structure of water adsorbed on these mineral surfaces.

Structure of adsorbed water at the mineral / water interface

The normalized density profiles of water computed at the gibbsite and imogolite – water interfaces are shown in Figure 4. Similar behaviors are found for both surfaces, indicating that they exert similar influences over the structure of adsorbed water. A difference in the width of the first peak, broader in the water profile of imogolite, indicates a less ordered first shell. The simplest explanation for this difference is the geometrical effect caused by the curvature of the imogolite surface: according to the Poisson-Boltzmann equation (Sposito, 2004), the decay of the electrostatic potential with the distance from the surface is more pronounced for a cylindrical surface than for a planar one[1]. However, although this explanation offers a qualitative idea of the effect of a charged surface over a charged particle (or dipole, like water), it assumes that the surface is uniformly charged, with no 'atomic roughness'.

The existence of two surface sites of adsorption for water molecules on both surfaces can be discerned from the angular distributions of water molecules at the surface (Figures 6 and 7). Two angles are needed to describe the orientation of a water molecule. We have defined θ as the angle between the water dipole vector and the vector normal to the mineral surface, and α the angle between the vector joining the two

[1] Solving the Poisson-Boltzmann equation within the Debye-Hückel approximation it can be shown that the electrostatic potential exhibits an exponential decay with increasing distance from the surface that is more pronounced for a cylindrical surface. The Poisson-Boltzmann equation for a charged cylinder does not have an analytical solution out of the Debye-Hückel approximation.

water hydrogen atoms and a vector normal to the mineral surface. The choice of the origin of the $\vec{HH}$ vector is irrelevant, as the angle α is α = α' for α' < 90° and α = 180° - α' for α' > 90°. The occurrence of the two adsorption sites is confirmed by looking at the distribution of the θ angle at the gibbsite and imogolite surfaces at low water coverage, and is more clearly distinguishable in the case of gibbsite (Figure 6).

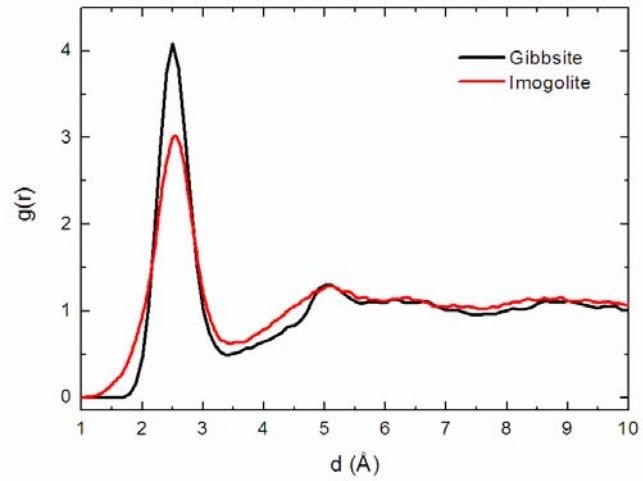


Figure 4*. Normalized water density profiles at the (001) gibbsite surface and at the external imogolite surface. The origin is placed at the positions of the surface O atoms.*

Two peaks can be distinguished in the first shell (d ≈ 2.5 Å) of all the histograms: one centered at θ ≈ 122º and another at an angle of θ ≈ 75º. In the case of gibbsite, this second peak shifts its position towards lower angle values as the water coverage increases. Figure 7 shows the angular distribution of the α angle. A careful examination of the angular distributions allows the orientations of the adsorbed water molecules to be described. In gibbsite, a first orientation (A: θ = 120º, α = 45º), corresponds to a water molecule with an OH pointing towards the surface and donating a hydrogen bond to a surface oxygen. In a second orientation (B: θ = 55º, α = 90º), a water molecule accepts a hydrogen bond from the surface (see Figure 5). These two sites were described first by Wang *et al*. (Wang et al., 2006) in their study of the gibbsite surface. In addition, in the θ maps of gibbsite it can be seen that the peak intensity corresponding to the A orientation (θ = 120º) does not increase when increasing water coverage, meaning that the additional molecules adsorb on the surface in the B orientation. The same orientations for water molecules are found at the imogolite surface (Creton et al., 2008a). However, and contrary to gibbsite, the A site is not saturated at a surface water coverage of $\phi = 0.5$.

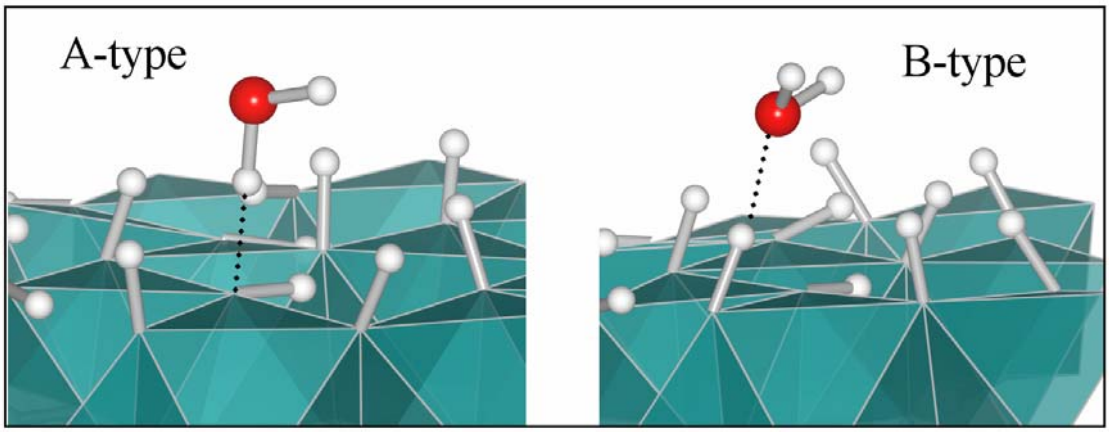


Figure 5*. A-type and B-type water molecules. The hydrogen bonds with the surface are indicated by dotted lines. The A-type water molecule gives a hydrogen bond to a surface oxygen, while the B-type water molecule receives a hydrogen bond from a surface oxygen. The green polyhedra are aluminum octahedra and the white spheres are hydrogen atoms.*

This trend, also observed in the evolution of the water atomic density profiles, can be followed in the evolution of the peak at $\theta = 120º$, which keeps growing from $\phi = 0.5$ to $\phi = 1$. Creton *et al*., also reported the occurrence of the site A on imogolite, but they did not discuss the second site (B) (Creton et al., 2008a). Their work focused on the existence of a third site (C) in which the water dipole vector points away from the surface, and that may occur in positive charged planar regions of the imogolite surface predicted by the vibrational breathing mode (Creton et al., 2008a).

Regarding the second shell ($d \approx 5$ Å) the angular maps for gibbsite show better defined orientations of θ and α, the orientational distribution of the water molecules being centered at $\theta \approx 130º$, $\alpha \approx 90º$. Again, the effect of the curvature is seen in the orientational distribution of the second shell of imogolite, which is poorly defined and much less structured than the second shell at the surface of gibbsite.

Water hydrogen bonds with the surface

An analysis of the hydrogen bonding of surface OH groups with water provides further explanation about the mechanisms of water adsorption. Histograms of the number of hydrogen bonds donated/accepted by an OH group to/from a water molecule are given in Figure 8.

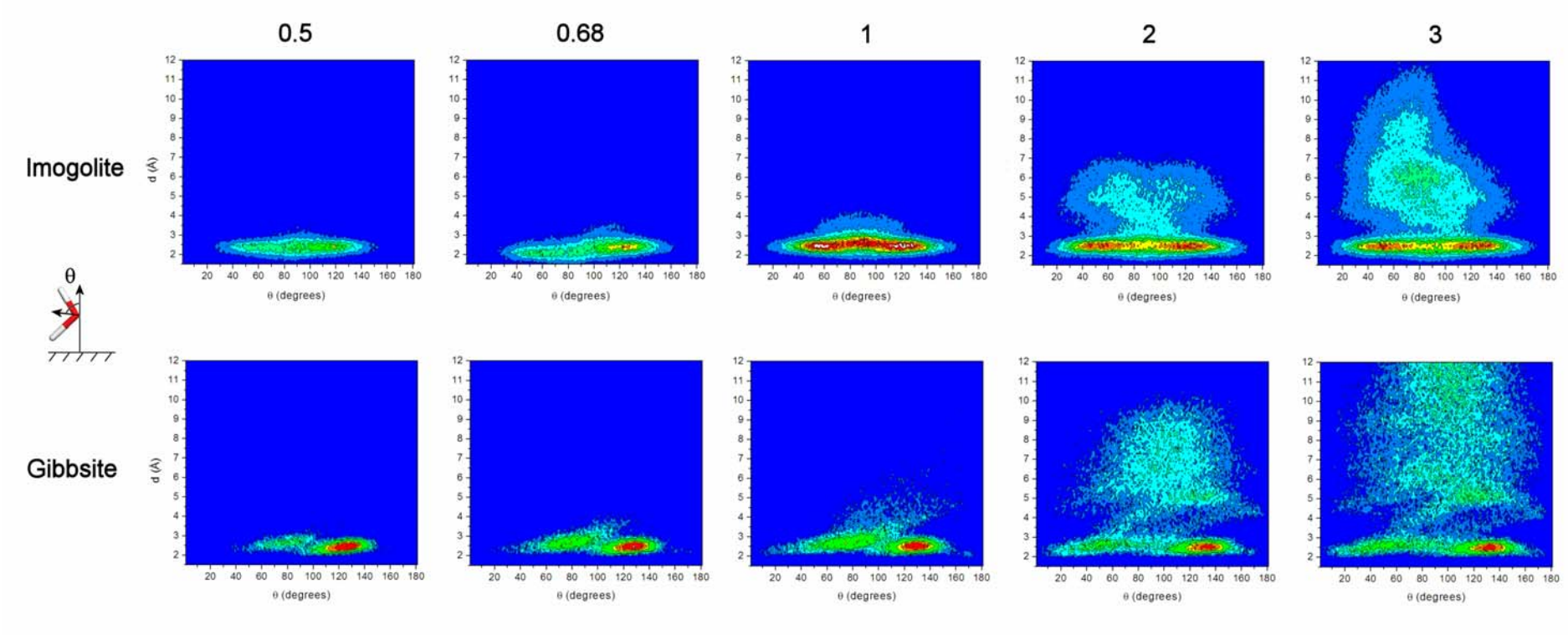


Figure 6. *Histograms of the θ orientations of water molecules at the surfaces of imogolite (up row) and gibbsite (low row) as a function of water coverage (numbers on the top). Blue color indicates a low probability of finding a certain orientation, and red represents the maximum probability. It can be observed that both mineral surfaces induce similar structures of water. A difference is seen in the second shell, much more structured in the case of gibbsite.*

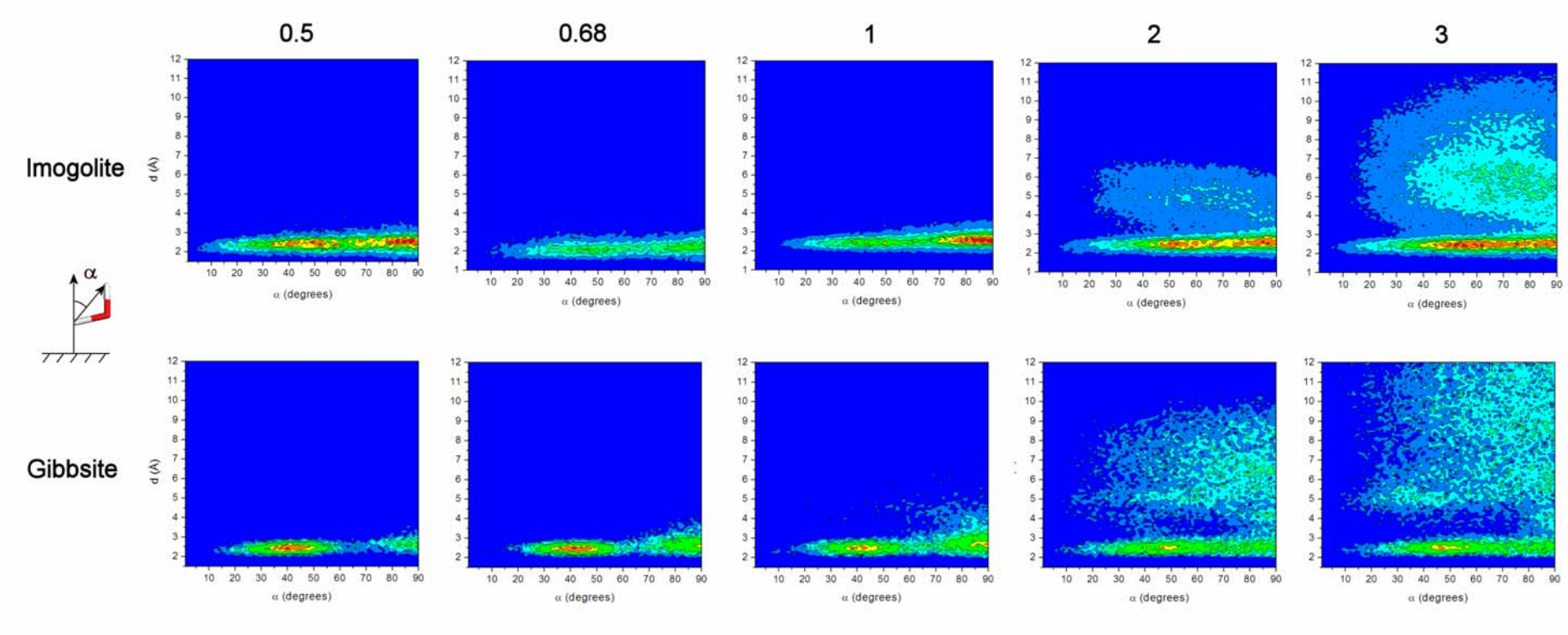


Figure 7*. Histograms of the α orientations of water molecules at the surfaces of imogolite (up row) and gibbsite (low row) as a function of water coverage (numbers on the top). Blue color indicates a low probability of finding a certain orientation, and red represents the maximum probability. Similar behaviors are observed.*

The criteria for defining an hydrogen bond has been set as following: a water molecule has been considered to be H-bonded if it is contained within the first peak of the OH pair correlation function, which extends to 2.2 Å in the case of a receiving H-bond from water, and to 2.3 Å for H-bonds donated to water, similar to the distances found by Machesky *et al*. (Machesky et al., 2008) (pair correlation functions not shown here). The results confirm one of the hypotheses considered previously: the number of accepting hydrogen bonds at the gibbsite surface is constant within all the ϕ range. On the other hand, the number of accepting hydrogen bonds at the imogolite surface increases, reaching a plateau at ϕ = 1. This fact reflects the difference in energetics of the two surfaces: the surface oxygen atoms with OH parallel to the surface (see Figure 3) are high energy sites of adsorption of type-A water molecules, and thus they are saturated at any surface coverage beyond ϕ = 0.5 (Figure 8). At the imogolite surface, 2/3 of the OH groups point perpendicularly to the surface, making the adsorption of type-A water molecules more difficult. The relative importance of type-A hydration water molecule goes from 22% at ϕ = 0.5 to 35% at ϕ = 4. In contrast, the percentage of type-A water molecules at the gibbsite (001) surface has a constant value of 32% throughout the whole ϕ range. Regarding the number of hydrogen bonds donated to water molecules as a function of surface coverage, the number increases on both surfaces reaching a plateau at ϕ = 1.5 and values of 57% of the OH sites giving a H-bond on imogolite, and 43% on gibbsite.

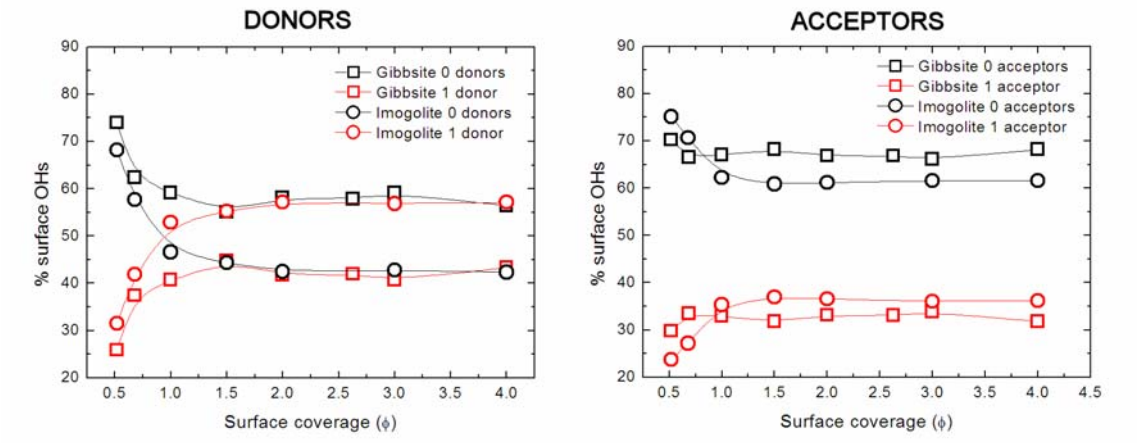


***Figure 8**. Percentages of surface OH groups receiving/donating 0 or 1 H-bonds from/to water molecules. All the curves reach a plateau at ϕ = 1-1.5, indicating that saturation has been reached.*

This analysis shows the effect of curvature, *i.e.*, the effect of the orientations of surface OH groups on the adsorption of water molecules. The imogolite surface is dominated by OH groups pointing perpendicularly to the surface, preventing the adsorption of type-A water molecules. The most common orientation for water is thus that of type-B (57%), which is less stable energetically. The gibbsite surface has surface OH groups pointing parallel to the surface, allowing the adsorption of type-A water molecules, which are more stable. This causes the total potential energy to decrease to a lower value than in the case of imogolite.

In Figure 9 the percentage of OH sites forming 0, 1 or 2 H-bonds with water is shown. It is interesting to note that, although most of the surface OH sites are forming H-bonds, all curves reach a plateau, meaning that a significative number of surface sites remain 'dry' or 'hydrophobic'even at high surface coverage values.

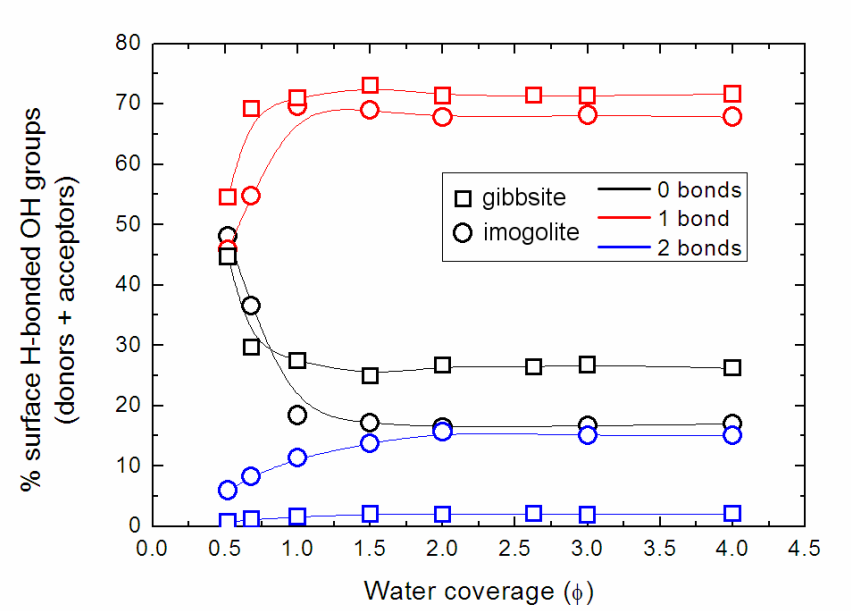


***Figure 9**. Percentages of surface OH groups forming 0, 1 or 2 H-bonds with water molecules. About a 15% of the sites are able to form 2 H-bonds with water molecules, in comparison with a 2% in gibbsite. A significative number of surface OH do not form any H-bond with water, indicating the presence of 'patching' effects of water at the surface.*

Several authors have reported a similar behavior on other mineral surfaces. Rahaman *et al*., who used the term 'surface patch' to describe this uneven repartition of water over the mineral surface, studied this patching effect at the $(10\bar{1}4)$ surface of calcite (Rahaman et al., 2008). They described a dynamic process of adsorption in which the formation of a stable multilayer of water molecules at the mineral surface is

attained after 6 ns reaction time. This time may depend on the nature of the mineral surface: ionic solids (such as calcite) may have longer reaction times, since their non-dissociative interaction with water molecules is weaker than for mineral surfaces populated by OH groups that form strong hydrogen bonds with water molecules. Our simulations show that equilibrium was reached at 1 ns (the occurrence of a plateau in Figure 9 is conclusive evidence that equilibrium was attained, even if tests on adsorption dynamics have not been performed), probably due to the previous equilibration of water using Monte-Carlo simulations. This behavior is striking, and has important conceptual implications in the field of geochemistry. Most geochemical SCMs assume uniform surfaces where the wetting is uniform (Davis et al., 1978; Hiemstra et al., 1989; Hiemstra and VanRiemsdijk, 1996; Sposito, 2004). These effects should be included in any molecular description of the electric double-layer and taken into account in SCMs. As a first step towards this, they will be evaluated in terms of the protonation constants of surface hydroxyl groups at the (001) surface of gibbsite and at the external surface of imogolite.

Effect of the curvature on the pKa

The (001) surface of gibbsite is dominated by $>Al_2OH^0$ functional groups. The pK_{a1} value for these groups has been subject of debate over the last 20 years. A MUSIC model reported by Hiemstra et al. (Hiemstra and VanRiemsdijk, 1996) concluded that these functional groups are not reactive in the pH range of environmental relevance (3-11), with $pK_{a1} = 0.0$. More recently, other authors have recently reported experimental values of $pK_{a1} = 5.9 \pm 0.2$ (Gan and Franks, 2006), that agree with a theoretical study by Bickmore *et al.* (2004) in which several values are reported for this type of doubly-coordinated neutral sites (Bickmore et al., 2004). In a more recent study, Bickmore *et al*. (personal communication) have revised the concept of protonation constant, suggesting that the protonation of a site produces relaxation effects in the bond lengths of the surrounding sites, affecting the pK_a values in a dramatic way (several log units). This finding has important conceptual implications, as the pK_a of a site can not longer be considered constant: its value changes as a function of protonation of the sites around it. This was already the central concept of the constant capacitance surface complexation model, where the pK_a value was linearly diverging from the intrinsic pK_a value as a function of the absolute value of the proton surface charge of the particle (Schindler and Stumm, 1987). Bickmore *et al.* have used a method that makes use of

ab-initio molecular dynamics (AIMD) simulations to calculate the average bond lengths of surface sites over time (Bickmore et al., 2004). They start with a totally de-protonated surface with $>Al_2O^-$ sites and a shell of hydration water; then a proton is added to one site of the oxygens, the bond-lengths are measured and the pK_a calculated. Each site is then protonated step-by-step, tracking the bond lengths and recalculating the pK_a at each step. It is important to note that an explicit water shell was introduced in the simulations, allowing the presence of relaxation effects originated by changes in the H-bonding that affect the number of hydrogen bonds per surface oxygen, and thus the pK_a. The method to calculate the pK_a is the same as the one presented in Bickmore *et al.* (2004). While this method seems to predict with accuracy the pK_a values obtained experimentally by Gan *et al.* (2006), its major drawback is the high amount of computational work it requires. For this reason its application to the surface of imogolite is not feasible with the computational resources available nowadays, due to the big unit cell required by the imogolite unit cell to be simulated. In order to establish the effect that the different hydrogen-bond and water structure has on the acidity of imogolite, compared to that of gibbsite, we opted for using the CD-MUSIC model. In this model, the pK_a is calculated using this expression:

$$-pK_a = \log K_a = -A\left(\sum_j s_j + V\right) \tag{4}$$

where A, equal to +19.8, is a constant that has been obtained from fits relating the log K_a of different known solution monomers with their calculated charge undersaturation (Hiemstra and VanRiemsdijk, 1996). This model introduces the effect of hydration by considering a part of the valence shared with the hydrogen-bond:

$$V \neq -\sum_j s_j = -\left[s_{Al-O} + ms_H + n(1 - s_H)\right] \tag{5}$$

where V is the valence of oxygen (-2), s_j is the valence associated with all the bonds reaching the oxygen atom, $s_{Al\text{-}O}$ is the bond valence of the Al-O bonds, s_H is the valence of the (m) H donating bonds, and (1-s_H) the valence of the (n) accepting ones. The CD-MUSIC model uses a constant s_H value of 0.8 for each strong bond with a hydrogen atom and a constant 0.2 1-s_H value for each H-bond accepted from a water molecule (Hiemstra and VanRiemsdijk, 1996). In our study we have chosen to make use of the bond valence approach to calculate the actual valence of the donor O-H bonds and of the H-bonds accepted by surface oxygen. The following known expression for bond

valence calculations calibrated by (Brown and Altermatt, 1985) from thousands of structures from the International Crystal Structure Database is used:

$$s_{O-H} = \sum_j \exp\left(\frac{r_0 - r_j}{B}\right) \quad (6)$$

where s_{O-H} is the bond valence, r_j is the O-H bond length (including H-bonded water molecules) and r_0 and B are fitted parameters specific of each anion-cation pair. For the O-H bonds the following set of parameters will be used:

r_{O-H} range (Å)	r_0 (Å)	B
< 1.05	0.907	0.28
$1.05 \leq r_{O-H} \leq 1.70$	0.569	0.94
> 1.70 Å	0.99	0.59

***Table 1**. Values of the parameters r_0 and B used to calculate the bond-valence of surface OH bonds, O…H and O…H_2O hydrogen bonds.*

The value of S_{O-H} decreases with the r_{O-H} distance, tending asymptotically to zero for large r_{O-H} distances. This allows the sum in equation 4 to be performed over all the water molecules around a surface site, in opposition to the analysis presented before in which the number of H-bonds was quantified using a distance cut-off value as a criterion. The inclusion of all the water molecules in the bond-valence sum was suggested by Brown *et al*. (Brown, 2002), who observed that interactions of water molecules in bulk water placed at long distances from each other should be considered if proper valence sums were to be maintained.

Equation 2 can be then expressed in the following terms:

$$\log K = -A\left(V + \sum \exp\left[(r_0 - r_{Al_m-O})/0.37\right] + \sum s_{O-H}\right) \quad (7)$$

Our study has been restricted to the protonation constant of the doubly coordinated $>Al_2OH^0$ groups present at the (001) gibbsite surface and at the external surface of imogolite. As it was shown before, the curvature of imogolite affects its H-bonding structure. This effect is reflected in the values of the bond-valences corresponding to accepting hydrogen bonds from water and from other surface hydrogen atoms to surface oxygens (see Figure 10).

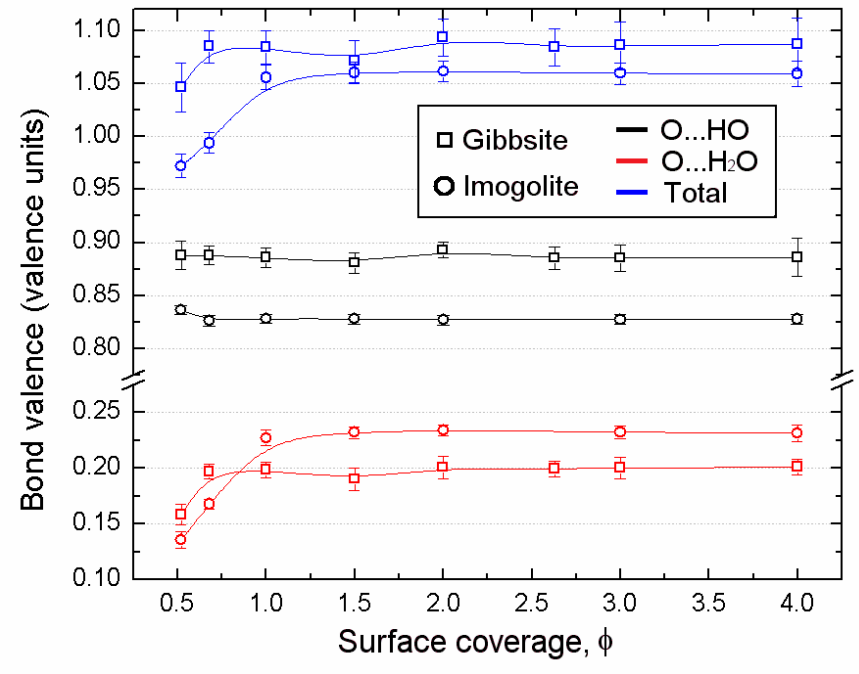


Figure 10. *Bond valences of surface oxygen sites due to H-bonding with water molecules (red) and with other surface OH groups + direct OH bonding (black). The blue curve indicates the total bond valence received by surface O atoms*

The fact that most of the OH groups at the gibbsite surface (5/6) form strong hydrogen bonds with other surface groups is reflected in the bond valence values corresponding to accepted hydrogen bonds plus the bonded hydrogen atoms (black squares in Figure 10), with values around 0.88 valence units. In the case of imogolite, the high percentage (2/3) of OH groups pointing perpendicularly to the surface results in less oxygens accepting hydrogen bonds from neighboring OH groups, their bond valence having values of 0.83 valence units. Regarding the interactions with water, oxygen atoms at the imogolite surface receive more charge from water hydrogens (≈ 0.23 valence units) in comparison to gibbsite, whose value remains constant at a value of 0.19 valence units practically over the whole range of surface coverage.

Values of the protonation constants of the neutral $>Al_2OH^0$ sites calculated by the CD-MUSIC model are very sensitive to small variations of the metal-oxygen bond lengths. We have constrained the bond valence values due to H-bonding of surface sites with water molecules and OH groups. However, in order to obtain these protonation constants using expression (5), values for the Al-O bond lengths have to be determined. Different techniques can be used (Pair Distribution Function, X-ray Absorption Spectroscopy) to obtain interatomic distances from bulk structures, but it is still very

difficult to obtain experimental values of interatomic distances from interfacial atoms. For these reasons, we have used *ab-initio* calculations of gibbsite and imogolite−water interfaces to obtain an estimation of the average Al-O bond lengths. In Figure 11, the Al-O bond lengths have then been used as a variable, and the $s_{Al\text{-}O}$ bond valences were calculated using equation (6), with $B = 0.37$ and $r_0 = 1.651$ Å.

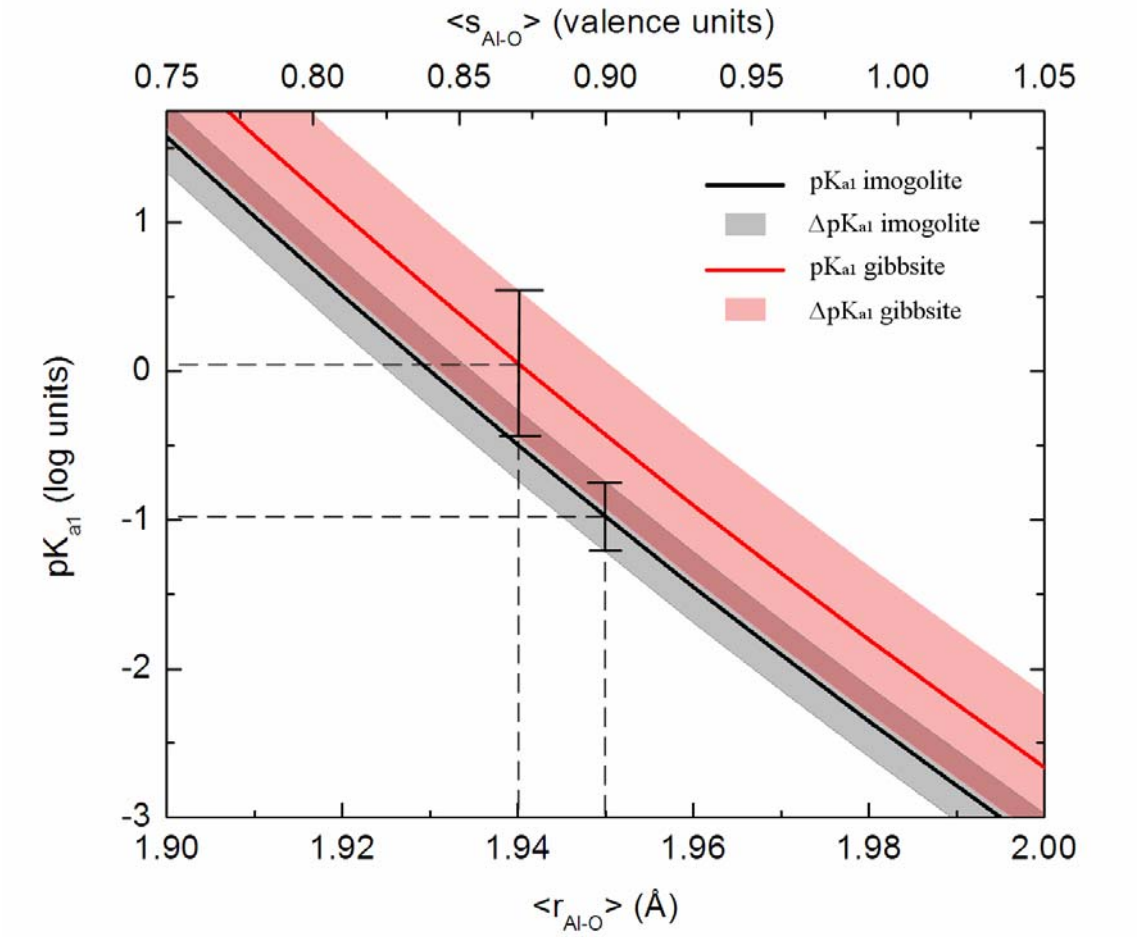


Figure 11. *Calculated pK_{a1} values for surface OH groups according to equation (5), in function of the Al-O bond lengths. The scale in the top abscissa indicates the total bond valence due to the two Al-O bonds. The error bars (gray and pink areas) have been calculated from the errors in the $s_{O\text{-}H}$ bond valences. An estimation of the absolute pK_{a1} values has been done using $<r_{Al\text{-}O}>$ distances obtained from ab-initio calculations.*

Both pK_{a1} values show a decreasing behavior towards lower values as long as the Al-O distances increase. The $r_{Al\text{-}O}$ bond lengths obtained from *ab-initio* calculations give an estimation of the pK_{a1} for each surface. For imogolite we obtained an average value of $<r_{Al\text{-}O}> = 1.95$ Å which yields a $pK_{a1\text{-}Imogolite} = -0.92 \pm 0.24$. The value obtained for the gibbsite groups is of $<r_{Al\text{-}O}> = 1.94$ Å, yielding a $pK_{a1\text{-}Gibbsite} = -0.05 \pm 0.50$. The acidity constant for imogolite doubly coordinated neutral groups is shifted towards more

acidic values by a $\Delta pK_{a1} = 0.87 \pm 0.75$. The value for gibbsite is in close agreement with the value reported by Hiemstra *et al.* (1996) using the CD-MUSIC model ($pK_{a1} = 0.0$), and in disagreement with the more recent results by Gan *et al*. and Bickmore *et al*., who proposed values at $pK_{a1\text{-}Gan} = 5.9 \pm 0.2$ and $pK_{a1\text{-}Bickmore} = 5.2$ (Bickmore et al., 2004; Gan and Franks, 2006).

CONCLUSIONS AND GEOCHEMICAL IMPLICATIONS

The effect of the curvature of two mineral surfaces with the same composition −the external surface of imogolite and the (001) surface of gibbsite− on their surface chemistry has been explored comparing a curved surface –imogolite– with a planar one –gibbsite–. MD simulations have shown that water molecules adsorb on both surfaces adopting similar orientations. However, the curvature of the imogolite surface prevents the formation of some H-bonds between surface OH groups, preventing the adsorption of A-type water molecules, which are strongly adsorbed at the surface of gibbsite. These A-type orientations, correspond to water molecules donating an hydrogen bond to a surface oxygen. At the gibbsite surface, the surface sites of adsorption of A-type water molecules are saturated at low water coverage ($\phi < 0.68$), whereas the surface of imogolite accepts water molecules in the same orientation still at water coverages $\phi > 0.68$. Water Gibbs free energies of adsorption have been calculated, revealing a hydrophilic behavior in both surfaces, but with a difference of $\Delta\Delta G$ = -2.19 kcal/mol between them, the surface of imogolite being more hydrophobic.

This relative imogolite hydrophobicity could be related to several properties that have been classically described as specific of this mineral. One of them, the formation of stable organo-mineral complexes, has been largely reported in the soil science literature as a characteristic of the soils where imogolite (and other *allophanic* clays) are present (Basile-Doelsch et al., 2005; Chevallier et al., 2007; Egli et al., 2008; Theng and Yuan, 2008; Wilson et al., 2008). The formation of organo−mineral complexes can be facilitated by the high density of surface functional groups at the surface of imogolite. However, prior to specific interactions with functional groups, the organic molecule has to be approached to the imogolite surface. The hydrophobic (or less hydrophilic) character of imogolite would be beneficial for this first step, as water is less structured in its surface than in other minerals (Wang et al., 2006), and the absence of isomorphic

substitutions makes that there is no permanent charge on its surface. Further investigations of this property should be made in the future to correctly assess the retention of organic matter by imogolite. Our simulations shed light on another important property of imogolite: its tendency to form bundles. It has been shown using MD simulations that the free energy profile of aggregation of two mineral particles is governed by the energy barriers created upon the formation of a shell of highly ordered water between the mineral surfaces (Spagnoli et al., 2008). In the case of imogolite this shell of adsorbed water is less structured, and a lower energy barrier is expected to occur, thus facilitating the aggregation between different nanotubes. MD simulations exploring these effects are on going.

These two properties (formation of bundles and adsorption of organic matter) are related to the 'patching' behavior observed in our MD simulations. The presence of 'dry' or 'hydrophobic' surface sites can be understood in terms of the low affinity of the surface for water molecules. Interfacial water have a tendency to form aggregates (Creton et al., 2008a) at the surface of imogolite in which the tetrahedral coordination of bulk water can be better satisfied (Bernal and Fowler, 1933). The formation of these 'dry islands' or 'patches' can promote the adsorption of organic molecules or the aggregation of different nanotubes. The presence of these dry sites has also implications in the concept of protonation constant. Models developed up to date including molecular descriptions of the mineral−water interfaces do not account for differences in wetting behavior, assuming that the water surface coverage is uniform over the mineral surface. New simulations and experimental studies of these patching effects are needed to determine (1) residence times of water molecules on specific sites and (2) the effect of these dry sites on the adsorption of ions and molecules. The proton transfer processes that occur upon the protonation or de-protonation of a surface site, in the femtosecond range (Rini et al., 2003), are very fast in comparison with the residence times of the order of picoseconds (Creton et al., 2008a) of water molecules on some mineral surfaces. For this reason the presence of patches can be considered a mechanism non-coupled to the proton transfer. The patches can be then understood as a 'static' property of the surface, only affecting to the surface area that has to be considered. More research in this direction has to be performed in order to address the relevance of these patches on the complexation of ions and molecules at mineral surfaces.

Finally, the structure of the water H-bonding at imogolite and gibbsite−water interfaces has been evaluated in terms of the protonation constants. MD simulations

reveal a more ordered and stronger network of H-bonded surface OH groups at the surface of gibbsite. The curvature of imogolite prevents the formation of some H-bonds between surface OH groups. This yields different values of the bond valences attributed to bonds between surface O atoms and water molecules, which result in more acidic pK_{a1} values for imogolite doubly-coordinated neutral sites by $\Delta pK_{a1} = 0.87 \pm 0.75$. The absolute values of the protonation constants reported in this work coincide with those reported by Hiemstra et al, who used the same CD-MUSIC model, but are in disagreement with the values reported by others. Spectroscopic studies focused on the exploration of the atomic structures at mineral−water interfaces are needed in order to obtain better structural descriptions allowing to develop reliable surface chemistry models.

ACKNOWLEDGEMENTS

Barry Bickmore and Kideok K. Kwon are gratefully acknowledged for enriching discussions. A.F.-M. acknowledges the Région Rhône-Alpes for the financial support received through an Explora'DOC fellowship for a 6-months stay at the University of California, Berkeley.

REFERENCES

Abdelfattah, A., and Wada, K. (1981) Adsorption of lead, copper, zinc, cobalt and cadmium by soils that differ in cation-exchange materials. Journal of Soil Science, 32(2), 271-283.

Abraham, F.F. (1978) Interfacial density profile of a Lennard-Jones fluid in contact with a (100) Lennard-Jones wall and its relationship to idealized fluid-wall systems - Monte Carlo simulation. Journal of Chemical Physics, 68(8), 3713-3716.

Alvarez-Ramirez, F. (2007) Ab initio simulation of the structural and electronic properties of aluminosilicate and aluminogermanate natotubes with imogolite-like structure. Physical Review B, 76(12).

Arai, Y., McBeath, M., Bargar, J.R., Joye, J., and Davis, J.A. (2006) Uranyl adsorption and surface speciation at the imogolite-water interface: Self-consistent spectroscopic and surface complexation models. Geochimica et Cosmochimica Acta, 70(10), 2492-2509.

Balan, E., Lazzeri, M., Morin, G., and Mauri, F. (2006) First-principles study of the OH-stretching modes of gibbsite. American Mineralogist, 91(1), 115-119.

Baltrusaitis, J., Schuttlefield, J., Jensen, J.H., and Grassian, V.H. (2007) FTIR spectroscopy combined with quantum chemical calculations to investigate adsorbed nitrate on aluminium oxide surfaces in the presence and absence of co-adsorbed water. Physical Chemistry Chemical Physics, 9(36), 4970-4980.

Basile-Doelsch, I., Amundson, R., Stone, W.E.E., Masiello, C.A., Bottero, J.Y., Colin, F., Masin, F., Borschneck, D., and Meunier, J.D. (2005) Mineralogical control of organic carbon dynamics in a volcanic ash soil on La Reunion. European Journal of Soil Science, 56(6), 689-703.

Beaglehole, D., and Christenson, H.K. (1992) Vapor adsorption on mica and silicon - Entropy effects, layering and surface forces. Journal of Physical Chemistry, 96(8), 3395-3403.

Bernal, J.D., and Fowler, R.H. (1933) A theory of water and ionic solution, with particular reference to hydrogen and hydroxyl ions. Journal of Chemical Physics, 1(8), 515-548.

Bickmore, B.R., Rosso, K.M., Tadanier, C.J., Bylaska, E.J., and Doud, D. (2006) Bond-valence methods for pK(a) prediction. II. Bond-valence, electrostatic, molecular geometry, and solvation effects. Geochimica et Cosmochimica Acta, 70(16), 4057-4071.

Bickmore, B.R., Tadanier, C.J., Rosso, K.M., Monn, W.D., and Eggett, D.L. (2004) Bond-Valence methods for pK(a) prediction: critical reanalysis and a new approach. Geochimica et Cosmochimica Acta, 68(9), 2025-2042.

Brown, I.D. (2002) The Chemical Bond in Inorganic Chemistry: The Bond Valence Model. Oxford University Press, New York.

Brown, I.D., and Altermatt, D. (1985) Bond-valence parameters obtained from a systematic analysis of the Inorganic Crystal-Stucture Database. Acta Crystallographica Section B-Structural Science, 41(AUG), 244-247.

Cantrell, W., and Ewing, G.E. (2001) Thin film water on muscovite mica. Journal of Physical Chemistry B, 105(23), 5434-5439.

Catalano, J.G., Fenter, P., and Park, C. (2009) Water ordering and surface relaxations at the hematite (110)-water interface. Geochimica et Cosmochimica Acta, 73(8), 2242-2251.

Chevallier, T., Woignier, T., Toucet, J., Blanchart, E., and Dieudonne, P. (2007) Fractal structure in natural gels: effect on carbon sequestration in volcanic soils. 14th International Sol-Gel Conference, p. 231-238, Montpellier, FRANCE.

Cradwick, P.D., Wada, K., Russell, J.D., Yoshinag.N, Masson, C.R., and Farmer, V.C. (1972) Imogolite, a hydrated aluminum silicate of tubular structure. Nature-Physical Science, 240(104), 187-&.

Creton, B., Bougeard, D., Smirnov, K.S., Guilment, J., and Poncelet, O. (2008a) Molecular dynamics study of hydrated imogolite - 2. Structure and dynamics of confined water. Physical Chemistry Chemical Physics, 10(32), 4879-4888.

-. (2008b) Molecular dynamics study of hydrated imogolite. 1. Vibrational dynamics of the nanotube. Journal of Physical Chemistry C, 112(27), 10013-10020.

-. (2008c) Structural model and computer Modeling study of allophane. Journal of Physical Chemistry C, 112(2), 358-364.

Cruz-Chu, E.R., Aksimentiev, A., and Schulten, K. (2006) Water-silica force field for simulating nanodevices. Journal of Physical Chemistry B, 110(43), 21497-21508.

Cygan, R.T., Greathouse, J.A., Heinz, H., and Kalinichev, A.G. (2009) Molecular models and simulations of layered materials. Journal of Materials Chemistry, 19(17), 2470-2481.

Cygan, R.T., Liang, J.J., and Kalinichev, A.G. (2004) Molecular models of hydroxide, oxyhydroxide, and clay phases and the development of a general force field. Journal of Physical Chemistry B, 108(4), 1255-1266.

Dahlgren, R.A., and Ugolini, F.C. (1989) Formation and stability of imogolite in a tephritic spodosol, Cascade Range, Washington, USA. Geochimica et Cosmochimica Acta, 53(8), 1897-1904.

-. (1991) Distribution and characterization of short-range-order minerals in spodosols from the Washington cascades. Geoderma, 48(3-4), 391-413.

Davis, J.A., James, R.O., and Leckie, J.O. (1978) Surface ionization and complexation at oxide-water interface. 1. Computation of electrical double-layer properties in simple electrolytes. Journal of Colloid and Interface Science, 63(3), 480-499.

Egli, M., Nater, M., Mirabella, A., Raimondi, S., Ploetze, M., and Alioth, L. (2008) Clay minerals, oxyhydroxide formation, element leaching and humus development in volcanic soils. Geoderma, 143(1-2), 101-114.

Fenter, P., Park, C., Nagy, K.L., and Sturchio, N.C. (2006a) Resonant anomalous X-ray reflectivity as a probe of ion adsorption at solid-liquid interfaces. 9th International Conference on Surface X-Ray and Neutton Scattering, p. 5654-5659, Taipei, TAIWAN.

Fenter, P., Park, C., and Sturchio, N.C. (2008) Adsorption of Rb+ and Sr2+ at the orthoclase (001)-solution interface. Geochimica et Cosmochimica Acta, 72(7), 1848-1863.

Fenter, P., Park, C., Zhang, Z., and Wang, S. (2006b) Observation of subnanometre-high surface topography with X-ray reflection phase-contrast microscopy. Nature Physics, 2(10), 700-704.

Fenter, P., and Sturchio, N.C. (2004) Mineral-water interfacial structures revealed by synchrotron X-ray scattering. Progress in Surface Science, 77(5-8), 171-258.

Gan, Y., and Franks, G.V. (2006) Charging behavior of the Gibbsite basal (001) surface in NaCl solution investigated by AFM colloidal probe technique. Langmuir, 22(14), 6087-6092.

Geissbuhler, P., Fenter, P., DiMasi, E., Srajer, G., Sorensen, L.B., and Sturchio, N.C. (2004) Three-dimensional structure of the calcite-water interface by surface X-ray scattering. Surface Science, 573(2), 191-203.

Good, W.R. (1973) Comparison of contact angle interpretations. Journal of Colloid and Interface Science, 44(1), 63-71.

Goodman, A.L., Bernard, E.T., and Grassian, V.H. (2001) Spectroscopic study of nitric acid and water adsorption on oxide particles: Enhanced nitric acid uptake kinetics in the presence of adsorbed water. Journal of Physical Chemistry A, 105(26), 6443-6457.

Guimaraes, L., Enyashin, A.N., Frenzel, J., Heine, T., Duarte, H.A., and Seifert, G. (2007) Imogolite nanotubes: Stability, electronic, and mechanical properties. Acs Nano, 1(4), 362-368.

Gustafsson, J.P. (2001) The surface chemistry of imogolite. Clays and Clay Minerals, 49(1), 73-80.

Hiemstra, T., Dewit, J.C.M., and Vanriemsdijk, W.H. (1989) Multisite proton adsorption modeling at the solid-solution interface of (hydr)oxides - A new approach. 2. Application to various important (hydr)oxides. Journal of Colloid and Interface Science, 133(1), 105-117.

Hiemstra, T., and VanRiemsdijk, W.H. (1996) A surface structural approach to ion adsorption: The charge distribution (CD) model. Journal of Colloid and Interface Science, 179(2), 488-508.

Kendall, T.A., and Martin, S.T. (2007) Water-induced reconstruction that affects mobile ions on the surface of calcite. Journal of Physical Chemistry A, 111(3), 505-514.

Kresse, G., and Hafner, J. (1993) Ab-initio molecular dynamics for liquid metals. Physical Review B, 47(1), 558-561.

-. (1994) Ab-initio molecular dynamics simulation of the liquid-metal amorphous semiconductor transition in germanium. Physical Review B, 49(20), 14251-14269.

Kresse, G., and Joubert, D. (1999) From ultrasoft pseudopotentials to the projector augmented-wave method. Physical Review B, 59(3), 1758-1775.

Levard, C., Doelsch, E., Rose, J., Masion, A., Basile-Doelsch, I., Proux, O., Hazemann, J.L., Borschneck, D., and Bottero, J.Y. (2009) Role of natural nanoparticles on the speciation of Ni in andosols of la Reunion. Geochimica et Cosmochimica Acta, 73(16), 4750-4760.

Liu, D.F., Ma, G., Xu, M., and Allen, H.C. (2005) Adsorption of ethylene glycol vapor on alpha-Al2O3(0001) and amorphous SiO2 surfaces: Observation of molecular orientation and surface hydroxyl groups as sorption sites. Environmental Science & Technology, 39(1), 206-212.

Machesky, M.L., Predota, M., Wesolowski, D.J., Vlcek, L., Cummings, P.T., Rosenqvist, J., Ridley, M.K., Kubicki, J.D., Bandura, A.V., Kumar, N., and Sofo, J.O. (2008) Surface Protonation at the Rutile (110) Interface: Explicit Incorporation of Solvation Structure within the Refined MUSIC Model Framework. Langmuir, 24(21), 12331-12339.

Michot, L.J., Villieras, F., Francois, M., Yvon, J., Ledred, R., and Cases, J.M. (1994) The structural microscopic hydrophilicity of talc. Langmuir, 10(10), 3765-3773.

Plimpton, S. (1995) Fast parallel algorithms for short-range molecular dynamics. Journal of Computational Physics, 117(1), 1-19.

Prestidge, C.A., and Ralston, J. (1995) Contact angle studies of particulate sulphide minerals. Minerals Engineering 95, p. 85-102, St Ives, England.

Rahaman, A., Grassian, V.H., and Margulis, C.J. (2008) Dynamics of water adsorption onto a calcite surface as a function of relative humidity. Journal of Physical Chemistry C, 112(6), 2109-2115.

Rahman, S., Takaki, H., Tamai, M., and Nagatomo, Y. (1996) Distribution of zinc, manganese, copper, cobalt, and nickel in Andosols profiles. Soil Science and Plant Nutrition, 42(4), 881-891.

Rini, M., Magnes, B.Z., Pines, E., and Nibbering, E.T.J. (2003) Real-time observation of bimodal proton transfer in acid-base pairs in water. Science, 301(5631), 349-352.

Rosenqvist, J., Persson, P., and Sjoberg, S. (2002) Protonation and charging of nanosized gibbsite (alpha-Al(OH)(3)) particles in aqueous suspension. Langmuir, 18(12), 4598-4604.

Saalfeld, H., and Wedde, M. (1974) Refinement of crystal-structure of gibbsite, $Al(OH)_3$. Zeitschrift Fur Kristallographie, 139(1-2), 129-135.

Schindler, P.W., and Stumm, W. (1987) Aquatic Surface Chemistry, Chemical Processes at the Particle-Water Interface. Ed. J. Wiley and Sons, New York.

Smith, D.E. (1998) Molecular computer simulations of the swelling properties and interlayer structure of cesium montmorillonite. Langmuir, 14(20), 5959-5967.

Spagnoli, D., Banfield, J.F., and Parker, S.C. (2008) Free energy change of aggregation of nanoparticles. Journal of Physical Chemistry C, 112(38), 14731-14736.

Sposito, G. (2004) The surface chemistry of natural particles. 242 p. Oxford University Press, New York.

-. (2008) The chemistry of soils. 330 p. Oxford University Press, New York.

Sposito, G., Skipper, N.T., Sutton, R., Park, S.H., Soper, A.K., and Greathouse, J.A. (1998) Surface geochemistry of the clay minerals. National-Academy-of-Sciences Colloquium on Geology, Mineralogy, and Human Welfare, p. 3358-3364, Irvine, Ca.

Sverjensky, D.A. (2005) Prediction of surface charge on oxides in salt solutions: Revisions for 1 : 1 (M+L-) electrolytes. Geochimica et Cosmochimica Acta, 69(2), 225-257.

Theng, B.K.G., and Yuan, G.D. (2008) Nanoparticles in the Soil Environment. Elements, 4(6), 395-399.

Ugolini, F.C., and Dahlgren, R.A. (1991) Weathering environments and occurrence of imogolite and allophane in selected andisols and spodosols. Soil Science Society of America Journal, 55(4), 1166-1171.

Veilly, E., Roques, J., Jodin-Caumon, M.C., Humbert, B., Drot, R., and Simoni, E. (2008) Uranyl interaction with the hydrated (001) basal face of gibbsite: A

combined theoretical and spectroscopic study. Journal of Chemical Physics, 129(24).

Villalobos, M., Cheney, M.A., and Alcaraz-Cienfuegos, J. (2009) Goethite surface reactivity: II. A microscopic site-density model that describes its surface area-normalized variability. Journal of Colloid and Interface Science, 336(2), 412-422.

Wada, K., and Yoshinaga, N. (1969) Structure of imogolite. American Mineralogist, 54(1-2), 50-&.

Wander, M.C.F., and Clark, A.E. (2008) Structural and Dielectric Properties of Quartz-Water Interfaces. Journal of Physical Chemistry C, 112(50), 19986-19994.

Wang, C., McKeague, J.A., and Kodama, H. (1986) Pedogenic imogolite and soils environments - Case study of spodosols in Quebec, Canada. Soil Science Society of America Journal, 50(3), 711-718.

Wang, J.W., Kalinichev, A.G., and Kirkpatrick, R.J. (2006) Effects of substrate structure and composition on the structure, dynamics, and energetics of water at mineral surfaces: A molecular dynamics modeling study. Geochimica et Cosmochimica Acta, 70(3), 562-582.

Whitley, H.D., and Smith, D.E. (2004) Free energy, energy, and entropy of swelling in Cs-, Na-, and Sr-montmorillonite clays. Journal of Chemical Physics, 120(11), 5387-5395.

Wilson, M.A., Tran, N.H., Milev, A.S., Kannangara, G.S.K., Volk, H., and Lu, G.Q.M. (2008) Nanomaterials in soils. Geoderma, 146(1-2), 291-302.

Xu, M., Liu, D.F., and Allen, H.C. (2006) Ethylenediamine at air/liquid and air/silica interfaces: Protonation versus hydrogen bonding investigated by sum frequency generation spectroscopy. Environmental Science & Technology, 40(5), 1566-1572.

Yu, C.J., Richter, A.G., Datta, A., Durbin, M.K., and Dutta, P. (1999) Observation of molecular layering in thin liquid films using X-ray reflectivity. Physical Review Letters, 82(11), 2326-2329.

Zhang, Z., Fenter, P., Cheng, L., Sturchio, N.C., Bedzyk, M.J., Predota, M., Bandura, A., Kubicki, J.D., Lvov, S.N., Cummings, P.T., Chialvo, A.A., Ridley, M.K., Benezeth, P., Anovitz, L., Palmer, D.A., Machesky, M.L., and Wesolowski, D.J. (2004) Ion adsorption at the rutile-water interface: Linking molecular and macroscopic properties. Langmuir, 20(12), 4954-4969.

Chapter 5

The structure of schwertmannite, a nanocrystalline iron oxyhydroxysulfate

5.1.- Introduction

The uncontrolled release of acid effluents into streams and lakes from abandoned mines, commonly known as 'acid mine drainage', is the responsible of the precipitation of poorly crystalline mineral phases that fix and mobilize trace contaminants such as arsenate, chromate or selenate (Carlson et al., 2002; Regenspurg and Peiffer, 2005). Natural processes, as the oxidative dissolution of iron sulphides, are also responsible of the drainage of acidic waters into the environment. One of these mineral phases, schwetmannite, is commonly found in acidic (pH 2-4) sulphate-rich waters where iron phases precipitate.

Schwertmannite, $Fe_8O_8(OH)_{8-x}(SO_4)_x$, was first reported and named by Bigham *et al.* (1994), who characterized it as having a structure akin to that of akaganeite. Akaganeite is composed by an octahedral iron frame into which chloride ions are adsorbed. A similar iron structure hosting sulphates in the place of chloride atoms has been proposed by many authors (Barham, 1997; Bigham et al., 1990; Waychunas et al., 2001; Waychunas et al., 1995). Laboratory experiments performed by Bigham *et al.* (1990) confirmed this hypothesis: they reported the existence of a poorly crystallized oxyhydroxysulfate of iron when $FeCl_3$ was hydrolysed in the laboratory in the presence of 1000 μg/mL of sulphate. The diffraction pattern of this precipitate showed a characteristic 8-lines profile that was similar to that observed in natural waters. The diffraction pattern showed some similarities to that of akaganeite, with the absence of the (110) reflection (note that another notation will be used in this chapter). Soon, other characterization techniques were applied. Bigham *et al*. (1990) confirmed using Mössbauer spectroscopy that all the iron in the structure was present as Fe^{3+}.

One of the battle horses in the study of the schwertmannite structure has been the variable chemistry reported, with sulphate concentrations ranging from 1 to 1.86 (Yu et al., 1999). Many studies have reported different complexation mechanisms for sulphate onto the *akaganeitic* structure of schwertmannite (Waychunas et al., 2001; Waychunas et al., 2005; Regenspurg and Peiffer, 2005). In particular, FTIR studies have reported different conformations, ranging from purely outer-sphere complexation to bidentate inner-sphere complexation. The use of other spectroscopic techniques like EXAFS has been unsuccessful in the unequivocal positioning of the sulfate groups in the structure.

In this study we report a combined X-ray Pair Distribution Function (PDF), X-ray diffraction analysis and molecular modeling study of the structure of schwertmannite.

The structure of schwertmannite, a nanocrystalline iron oxyhydroxysulfate

A. Fernandez-Martinez[1,2], V. Timon[3], G. Roman-Ross[4], G. J. Cuello[2,5], J. E. Daniels[6] and C. Ayora[7]

[1] *Equipe de Geochimie de l'Environnement, LGIT, University of Grenoble and CNRS. B.P. 53, 38041 Grenoble, France.*

[2] *Institut Laue-Langevin. B.P. 156, 38042 Grenoble, France.*

[3] *Estacion Experimental del Zaidin, CSIC, C/ Profesor Abareda, 1, 18008 Granada, Spain*

[4] *Chemistry Department, University of Girona, Campus de Montilivi, 17071 Girona, Spain*

[5] *Dept. Applied Physics II, UPV/EHU and Ikerbasque, 48080, Bilbao, Spain*

[6] *European Synchrotron Radiation Facility, B.P. 220, 38043 Grenoble, France*

[7] *Institute of Environmental Assessment and Water Research, IDAEA, CSIC, Jordi Girona 18, 08034 Barcelona, Spain*

Submitted to American Mineralogist (June 2009)

ABSTRACT

Schwertmannite is a poorly crystalline mineral that forms ochre rusts and precipitates in acid mine environments. Despite its ubiquity and its role as scavenger of important contaminants such as arsenic or selenium, its structure has not been yet determined. Here, the structure for schwertmannite is presented based on Pair Distribution Function (PDF) data, X-ray Diffraction (XRD) analyses and Density Functional Theory (DFT) calculations. We propose a structure formed by a deformed frame of iron octahedra similar to that of akaganeite. Simulations of X-ray diffraction patterns unveil the presence of long-range order associated with the position of the sulfate molecules, providing a useful way to discern two types of sulfate complexes in the structure. Knowledge of the positions of the sulfates in the structure will help to better understand their exchange processes with oxyanions of trace contaminants such as arsenate, chromate or selenate, strongly influencing their biogeochemical cycling in mining ecosystems.

INTRODUCTION

Schwertmannite is a poorly crystalline ferric oxyhydroxysulfate that forms ochreous coatings on sulfide-bearing rocks and soils. It also precipitates in streams and lakes receiving acid mine drainage where the weathering of iron sulfide minerals produces SO_4 and Fe(II) acid solutions. When exposed to the atmosphere, bacterially mediated oxidation of Fe(II) occurs and large quantities of nanoparticulated Fe(III) phases may form. Moreover, schwertmannite is a key solid in removing acidity in treatment systems where Fe(II) is rapidly oxidized by addition of alkalinity to acid mine drainage (Gagliano et al., 2004; Rotting et al., 2008). Further, in anoxic environments such as acid lakes, flooded soils and wetlands, schwertmannite particles can serve as electron acceptor for Fe(III) reducing bacteria, releasing the Fe(II) necessary for sulfate reduction and neoformation of iron sulfides (Burton et al., 2007). Schwertmannite forms aggregates of nanoparticles of typical hedge-hog morphology.

Due to its high specific surface and positive charge in acid waters, schwertmannite efficiently removes oxyanions such as AsO_4^{3-}, SeO_4^{2-} and CrO_4^{2-} from water (Carlson et al., 2002; Regenspurg and Peiffer, 2005; Waychunas et al., 1995). However, despite its ubiquity and its important geochemical role, schwertmannite was only recently recognized as a mineral (Bigham et al., 1994). Reasons for this late recognition include its poor crystallinity, its frequent association with more crystalline phases such as goethite and jarosite, and its metastable structure, which transforms into goethite and jarosite within months (Acero et al., 2006; Bigham et al., 1996).

The chemical composition of schwertmannite is also object of controversy. Bigham et al (Bigham et al., 1994) first proposed the chemical formula as $Fe_8O_8(OH)_{8-x}(SO_4)_x$, with x varying from 1 to 1.75. Yu et al. (Yu et al., 1999) later estimated x to vary from 1.74 to 1.86. Uncertainty on the range of x values may be caused by the different location of the sulfate groups in the structure. The first approach to the structure of a “poorly crystalline sulfate oxyhydroxide” was given by Bigham et al. (Bigham et al., 1990), who synthesized akaganeite-like materials with different concentrations of sulfate, that reproduced the 8-diffraction lines characteristic of schwertmannite, suggesting similarities between the octahedral iron frame of schwertmannite and akaganeite. Although some authors have proposed a ferrihydrite-like structure (Loan et al., 2004), there is more general agreement in the literature about this idea of schwertmannite structure being akin to that of akaganeite, with a channel-like iron octahedral frame to which sulfate molecules are bound (Barham, 1997; Bigham et al., 1990; Waychunas et al., 2001; Waychunas et al., 1995). However, no

clear experimental evidence on the structure of the iron octahedra or the positions of the sulfates has been reported yet. Since trace element oxyanions like AsO_4^{3-}, SeO_4^{2-} or CrO_4^{2-} replace SO_4^{2-}, knowing the allocation of the sulfate groups in the structure is essential to understand the retention of the oxyanions in the solid phase.

X-ray diffraction studies have been limited by the reduced size of schwertmannite crystallites, which give broad diffraction peaks making thus difficult to perform a detailed crystallographic analysis of the structure. In the recent years, the Pair Distribution Function (PDF) technique, classically known as the Patterson function technique (Guinier, 1994), has been used to study poorly crystalline precipitates of environmental relevance like mackinawite (Michel et al., 2005; Scheinost et al., 2008), magnetite (Scheinost et al., 2008) or ferryhydrite (Michel et al., 2007a; Michel et al., 2007b). This technique relies on a Fourier transform of the whole diffraction pattern, and it is thus particularly well suited to the study of poorly crystalline phases of reduced crystallite size, where diffuse scattering has a significant contribution to the diffraction pattern. In this study, we present a combined high-energy X-ray diffraction and theoretical study of the structure of schwertmannite.

MATERIALS AND METHODS

Two types of schwertmannite specimens were used in this study: natural and synthetic. Natural samples were taken as fresh precipitates from the acid drainage in Monte Romero mine (Iberian Pyrite Belt), Spain. Synthetic schwertmannite was precipitated by adding ferric chloride to sodium sulfate solutions. The produced suspension was held at 60° C for 12 minutes and then cooled at room temperature and dialysed for a period of 30 days (Schwertmann and Cornell, 1991). Samples of natural schwertmannite were dried following two different procedures: air-dried, and freeze-dried. This allowed us to check for any possible effect of the drying mechanism on the observed structure. Once dried, the powder samples were loaded into 0.8 mm diameter polymide capillaries which were sealed with wax.

High-energy X-ray total scattering experiments were performed at beamline ID15B of the European Synchrotron Radiation Facility, Grenoble, France. Scattering data were collected with a Pixium 4700 detector (Daniels and Drakopoulos, 2009) using the Rapid-Acquisition pair Distribution Function technique (Chupas et al., 2003). Measurements of the samples, empty capillary, and the background were made at ambient temperature in a q-range of 0 – 25 $Å^{-1}$. The X-ray wavelength was refined using a Ni standard (λ = 0.14252 Å).

Corrections for sample-detector distance, tilt angle of the detector with respect to the direction of the incident radiation and polarization were performed using Fit2D (Hammersley et al., 1995). Total scattering structure functions and Pair Distribution Functions (PDF) were obtained using the PDFGetX2 software (Qiu et al., 2004). A crystalline standard (LaB_6) was measured and used to calculate the instrumental resolution effect on the PDF (Toby and Egami, 1992). Fits of the PDFs were performed using the PDFGui software (Farrow et al., 2007). In a PDF, the partial pair correlation functions between two atoms *i* and *j*, $g_{ij}(r)$, are weighted by a function, $w_{ij}(r)$ (Egami and Billinge, 2003):

$$w_{ij} = c_i c_j \frac{f_i f_j}{\langle f \rangle^2} \tag{1}$$

c_i and c_j being the concentrations of the elements *i* and *j* and f_i and f_j their atomic form factors evaluated at $q = 0$. q is the scattering vector:

$$q = \frac{4\pi \sin(\theta)}{\lambda} \tag{2}$$

and:

$$\langle f \rangle^2 = \left(\sum_i c_i f_i \right)^2 \tag{3}$$

Only the *x* and *z* coordinates of the iron atoms were refined during the fitting procedure. The reason for this is two-folded: (1) we expect the changes in the structure coming from changes in the *a* and *c* lattice parameters, or from changes in the value of the β angle, and (2) as shown in Figure 1, the correlations between Fe-Fe and Fe-O atom pairs are the dominant contributions in the PDF of schwertmannite. The atomic form factor f_i is proportional to the atomic number Z. Of all the elements present in the structure of schwertmannite, iron is the one with higher atomic number ($Z_{Fe} = 26$), which makes that the weighting factors of the atomic pair-correlations (equation 1) including iron atoms are higher. The goodness of the refinements was checked using the weighted agreement factor R_w (Egami and Billinge, 2003).

All the geometry optimizations were performed using the DFT code CASTEP (Clark et al., 2005). The calculations were performed using Vanderbilt ultrasoft pseudopotentials, with a plane-wave basis set energy cut-off of 760 eV and the Revised Perdew-Burke-Ernzerhof functional (Perdew et al., 1996) of the Generalized Gradient Approximation

(GGA). Brillouin zone integrations were done at special k-points determined according to the Monkhorst-Pack method, which gave 6 special k points. Preliminary calculations were performed on akaganeite structure (Post et al., 2003) with the aim of tuning the convergence in k-points, pseudopotentials and energy cut-off. The obtained cell parameters show good agreement with the experimental values, within 1% (see Table 2).

Diffraction patterns of the resulting models of schwertmannite were generated using the code FORCITE (Accelrys Inc.). In this code the diffraction pattern is calculated using the Debye formula of diffraction:

$$I_N(q) = \sum_{n,m\neq n}^{N} f_n(q) f_m(q) \frac{\sin(qr_{nm})}{qr_{nm}} \qquad (4)$$

where r_{nm} is the distance between two pair of atoms n and m. A cutoff of 40 Å was used, meaning that only pairs of atoms placed at a distance r_{nm} < 40 Å were included in the calculation.

The structure of akaganeite is composed of double chains of iron (95% occupancy) or nickel (5% occupancy) oxide (or hydroxide) octahedra, which share corners to form squared tunnels (see Figure 2) (Post et al., 2003). Each unit cell has two identical tunnels, with centers in the points of fractional coordinates (0, 0, 0) and (0.5, 0.5, 0.5) of the akaganeite unit cell. The research strategy followed in this work is as follows: the structure of akaganeite was modified replacing all the nickel atoms by iron atoms. A supercell 1×2×1 was created, and the chlorine atoms were substituted by two sulfate molecules forming bidentate inner-sphere complexes on the internal surface of akaganeite's channel (this model will be called from now on 'sulfate-doped akaganeite'). The PDF of the sulfate-doped akaganeite structure was simulated in order to figure out the sensitivity of the X-ray PDF technique to determine the relative positions of the different atoms within the unit cell. As it can be seen it Figure 1, the result of the simulation shows that the PDF technique is mostly sensitive to the relative positions of Fe and O atoms only. The contribution of the sulfate molecules to the total PDF is very low, as it could be expected from previous theoretical estimations done using equations (1-3). This structure was used as the initial model for the fitting of the PDF data. In parallel, the sulfate-doped akaganeite was optimized using DFT in order to understand the some trends observed in the structures obtained in the PDF refinements. Charge equilibration was ensured in the unit cells by adjusting the number of hydrogen atoms present in the structures as OH groups so the total

charge is zero. In addition, powder diffraction patterns of the refined and other structures were simulated to check the consistency between the short-range order revealed by PDF analyses and the long-range order underlying the diffraction patterns.

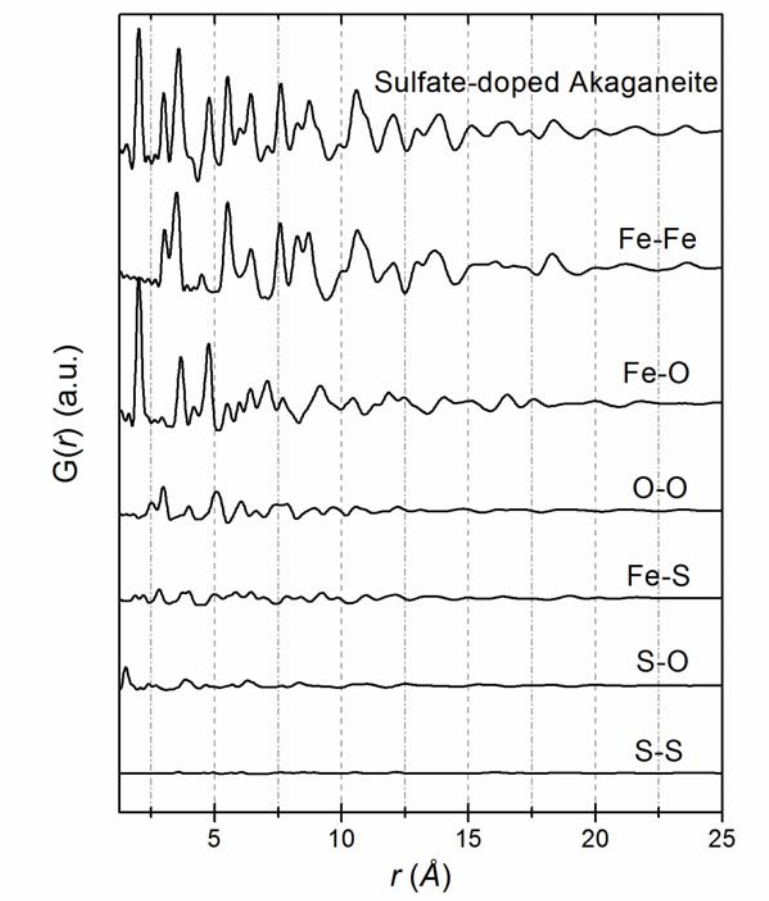


Figure 1. *Simulated PDF of sulfate-doped akaganeite with its partial PDFs. The partial PDFs are weighted by their weighting functions,* w_{ij}*.*

RESULTS AND DISCUSSION

Octahedral iron frame

PDFs of the natural and synthetic schwertmannite samples and simulated PDFs of the akaganeite (Post et al., 2003) and sulfate-doped akaganeite structures are presented in Figure 3. No major differences can be found between the PDFs of air-dried and freeze-dried samples, meaning that the schwertmannite structure does not suffer any structural modifications when freeze-dried, as found, for instance, for ferrihydrite (Greffie et al., 2001). The main difference is a slight increase in the intensity of the first peak in the PDF of natural freeze-dried schwertmannite. However, we do not think this is a structural effect nor a consequence of the drying procedure, as (1) the intensity of this peak is affected by vibrational correlations (Egami and Billinge, 2003) and (2) we do not observe the same

effect in the freeze-dried synthetic schwertmannite. A comparison with the PDF of the crystalline standard LaB_6 (not shown) allows estimating the size of the coherent domains of schwertmannite. The decay in the intensity of the PDF of LaB_6 at high *r* values can be ascribed to the effect of instrumental resolution (Toby and Egami, 1992). Instead, a more pronounced decay (within the instrumental resolution) is found in the PDF of the schwertmannite samples. Fits of this decay with a function reproducing particles of spherical shape (Gilbert, 2008), yield an average particle diameter of 3-4 nm (see Table 1). The small size of the coherent domains contrasts with that of schwertmannite aggregates, which are usually described as having hedgehog-like morphologies with needles in the range of the micrometer.

The PDFs of akaganeite and schwertmannite structures reveal very similar local structures. Common structural features can be identified in the region from 1 to 7 Å: the position of the first peak at ~1.98 Å is the same for both structures. It corresponds to the Fe-O distance of Fe^{3+} in octahedral coordination. The presence of sulfates in sulfate-doped akaganeite and in schwertmannite can be discerned from a small peak appearing at a distance of ~1.64 Å, which corresponds to the S-O distance. The peaks at ~3 Å and ~3.45 Å, better resolved in the modeled PDFs of akaganeite, correspond to Fe-Fe distances of different types of edge-sharing iron octahedra: the distance at ~3 Å is originated by two iron octahedra lying on the

same equatorial plane, while the distance at ~3.45 Å comes from edge-sharing iron octahedra with different equatorial planes. The next three peaks (4.75 Å, 5.45 Å, 6.33 Å) correspond to Fe-Fe and Fe-O correlations. Although there are some small differences, their positions and intensities are very similar. The main differences between these two structures arise from correlations in the region 7 Å < *r* < 10 Å. A significant decrease in the intensity of the peak at *r* = 7.5 Å is observed in the PDF of the schwertmannite samples. This peak is originated by correlations between iron atoms placed on opposite sides of the akaganeite's channel (atoms Fe1 and Fe2 in Figure 2). However, its intensity is affected by the presence of sulfate molecules in the structure, as can be observed in the case of sulfate-doped akaganeite, where it has lower intensity.

Fitting of the PDF data was performed with the aim of explaining the differences observed between the theoretical PDFs of akaganeite and sulfate-doped akaganeite, and the

experimental PDFs of schwertmannite. The structure of sulfate-doped akaganeite was used as initial model in the refinements. The results of the refinements are presented in Figure 4.

	Natural air-dried	Natural freeze-dried	Synthetic freeze-dried	LaB_6
a (Å)	10.368 (0.097)	10.4974 (0.060)	10.5279 (0.072)	4.1594 (0.0004)
b (Å)	6.05 (0.04)	6.03597 (0.045)	6.03025 (0.025)	4.1594 (0.0004)
c (Å)	10.75 (0.17)	10.752 (0.15)	10.7657 (0.12)	4.1594 (0.0004)
β (º)	87.87 (1.3)	86.70 (0.88)	87.19 (0.83)	90
Vol (Å^3)	674.8 (0.3)	680.1 (0.3)	682.6 (0.2)	71.9602 (0.0012)
U_{Fe} (Å^2)	0.003 (0.002)	0.002 (0.001)	0.003 (0.002)	
U_O (Å^2)	0.008 (0.006)	0.009 (0.005)	0.01 (0.01)	
[1]U_S (Å^2)	0.0015	0.015	0.015	
U_{La} (Å^2)				0.0044 (0.0004)
U_B (Å^2)				0.0107 (0.002)
d (Å)	44.15 (0.04)	30.91 (0.05)	37.95 (0.06)	∞
[2]σ_q (Å^{-1})	0.0309	0.0309	0.0309	0.0309 (0.0014)
R_w (%)	25.98	26.01	21.71	17.85

[1] U_S was fixed to an estimated value of $U_S = 0.015$ Å^2.

[2] The value of the dampening factor was calculated for the LaB_6 standard and kept constant during the refinements of the schwertmannite PDFs.

Table 1. *Results of the PDF refinements. U stands for the isotropic thermal displacement contributing to the Debye-Waller factor, σ_q is the instrumental dampening factor of the PDFs originated by the limited q-resolution, d is the diameter of the coherent domain size (spherical approximation) and R_w is the weighted agreement factor.*

All the fits converged yielding a structure where the initial akaganeite unit cell was deformed, with values of the β angle around $\beta \approx 87º$ (Table 1). This deformation was observed in all the fits performed. We found a monoclinic unit cell, with three different values for the parameters *a*, *b* and *c* (see lattice parameters in Table 1). The unit cell parameters obtained differ from those proposed by Bigham *et al.*, (Bigham et al., 1994),

who proposed a tetragonal unit cell with lattice parameters $a = c = 10.66$ Å and $b = 6.04$ Å. A note has to be made here about the indexation of the akaganeite and schwertmannite structures. Bigham and co-workers have used an indexation in which the direction of the channel of akaganeite's structure lies on the *c* axis. However, we used to build our models the akaganeite structure published by Post (Post et al., 2003), in which the channel extends along the *b* axis of akaganeite's unit cell. From now on the notation of Post et al. (2003) will be used in the text.

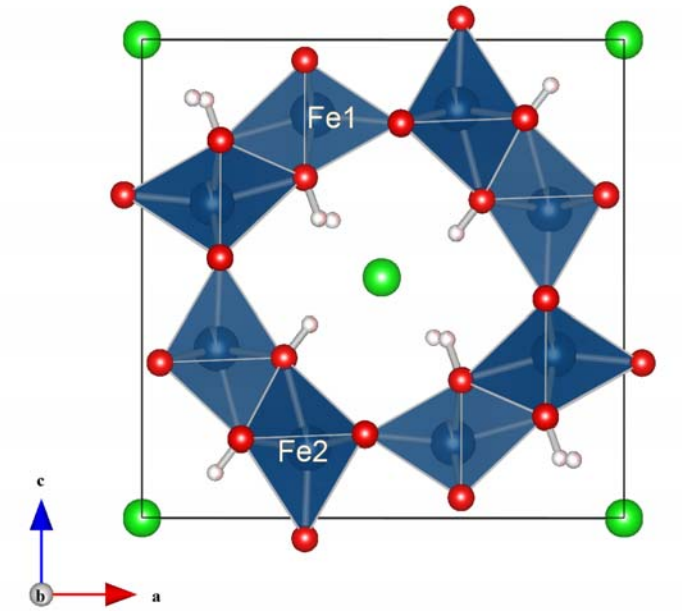


Figure 2. *Structure of akaganeite. The octahedra are formed by iron (95%) or nickel (5%) atoms (blue) surrounded by six oxygen atoms (red). The tunnel structure is occupied by chlorine atoms (green). The distance between atoms Fe1 and Fe2 is equal to d = 7.5 Å, and can be clearly distinguished in the PDF of akaganeite (Figure 3).*

The different values found for the lattice parameters *a* and *b* provide a partial explanation for the decreasing of the intensity of the correlation at r = 7.5 Å. A splitting of this distance into several distances in the range between 7.4 - 7.8 Å is found in the refined structures. This splitting is reflected in the PDF of schwertmannite by a decrease in the peak intensity and a broadening of its width. As shown in Figure 3, the presence of sulfates in the structure affects the intensity of this peak too. Two different configurations for the iron atoms within the unit cell of schwertmannite resulted from the PDF refinements. In a first model, (called Model 1 from now on), the distortion of the β angle causes that the distance between some adjacent iron atoms (Fe1 and Fe2 in Figure 5) is too long to form two corner-sharing iron octahedra (d ~ 4.3 Å). This model was obtained after the fitting procedure of

the PDF of the natural freeze-dried schwertmannite sample. The second model (Model 2) yielded a structure where the Fe1 octahedron is turned by 90 degrees, sharing an edge with another iron octahedron from the neighbor frame (Figure 6).

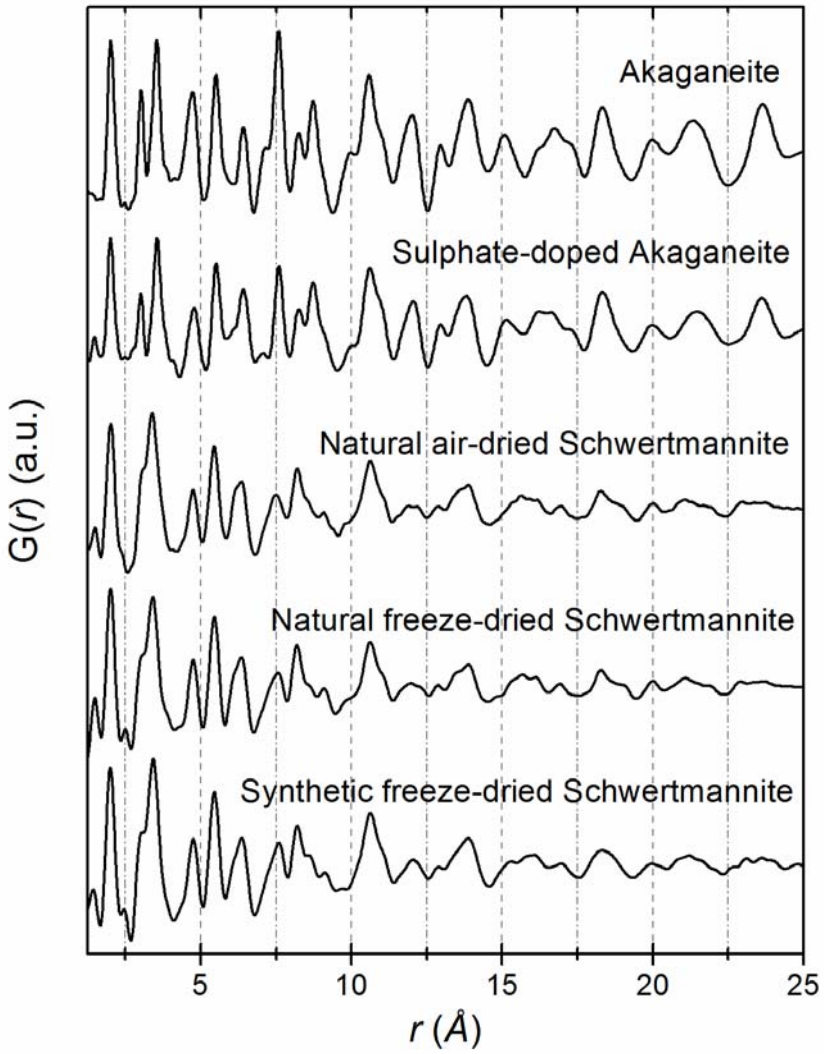


Figure 3. *Simulated PDFs for akaganeite and sulfate-doped akaganeite, and experimental PDFs of schwertmannite samples. The decay in the intensity seen at high r in the schwertmannite PDFs has been taken into account in the simulated PDFs by using the instrumental dampening factor obtained from the refinement of the* LaB_6.

This second structure resulted from the fitting of the natural air-dried and synthetic freeze-dried schwertmannite samples. The fact that the PDFs of the three samples are almost identical and that the agreement factors of the three fits lie in the same range (Table 1) tells us about the no-uniqueness of the result. Both models are then possible within the experimental resolution of our data.

In order to better understand the origin of the deformation, we performed DFT-based geometry optimization of the structure of sulfate-doped akaganeite. This structure has two sulfate molecules forming bidentate inner-sphere complexes (C_{2v} symmetry). The optimized and non-optimized structures are shown in Figure 7, and their cell parameters are given in Table 2.

Structure	***a* (Å)**	***b* (Å)**	***c* (Å)**	**α (°)**	**β (°)**	**γ (°)**	**Volume (Å^3)**
DFT-optimized akaganeite	10.45	3.07	10.45	90.00	90.25	89.91	337
Experimental akaganeite	10.58	3.03	10.52	90	90.03	90	337
DFT-optimized sulfate-doped akaganeite	10.55	6.03 [1]	10.59	90.47	87.39	89.40	674

[1] The structure of sulfate-doped akaganeite was formed from a supercell 1×2×1 of akaganeite. This is the reason why the *b* parameter and the volume are almost double than for akaganeite.

Table 2. *Unit cell parameters and volume of the optimized and experimental akaganeite structures (Post et al., 2003) and of the optimized sulfate-doped akaganeite structure.*

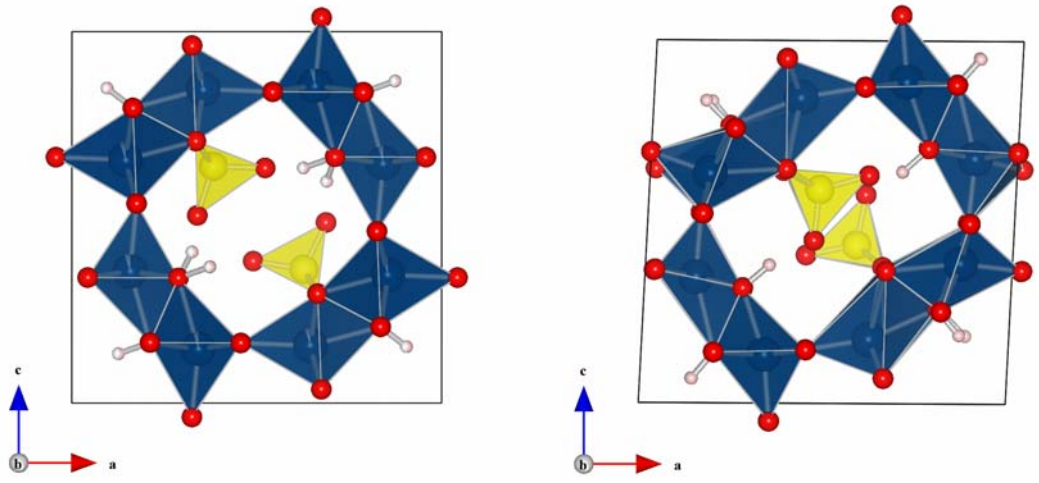


Figure 7. *Structure of sulfate-doped akaganeite before (left) and after (right) being optimized using DFT-based calculations.*

A similar deformed structure to the observed experimentally, with $\beta \approx 87^{o}$ was obtained. The volume of the optimized cell (V = 674 $Å^3$) is slightly smaller than the experimental value for schwertmannite reported by Bigham et al. V = 687 $Å^3$ (Bigham et al., 1994), and it is in the same order of magnitude of the experimental values found by PDF analysis (see Table 1). The deformation of the unit cell can be monitored by looking at the values of the stress tensor calculated by CASTEP at the first optimization step. The presence of the sulfate molecules in the structure makes that the off-diagonal elements σ_{XZ} and σ_{ZX} have values higher than zero, indicating a shear stress which leads to the deformation of the angle β of the unit cell (see Table 3). The non-zero values of the diagonal elements (σ_{XX}, σ_{YY} and σ_{ZZ}) are responsible for changes in the lattice parameters and thus do not induce deformations of the unit cell angles. The fact that this deformed structure fits well the experimental PDF data supports thus the hypothesis, suggested by FTIR data (Jonsson et al., 2005; Peak et al., 1999), that these inner-sphere complexes, with sulfates having $C_{2\upsilon}$ symmetry, actually exist in the schwertmannite structure.

Position of the sulfate molecules

It is important to note that the PDF of schwertmannite is dominated by correlations involving iron and oxygen atoms (see Figure 1). This implies that only the short-range order of the octahedral iron frame is refined in the PDF fitting procedure, rendering impossible the determination of (1) the number of sulfates, (2) their exact positions and (3) their orientations within the unit cell of schwertmannite from PDF data analysis. In addition, PDF analysis gives information only about the local or short-range order of the schwertmannite structure. Information about the long-range order can be extracted by analyzing the powder diffraction pattern. This kind of analysis has been hindered by the broad diffraction peaks found in the schwertmannite diffraction patterns. For this reason, the use of X-ray diffraction for structural studies has been limited in the schwertmannite literature, serving mainly as a fingerprint for identification purposes. In contrast to these data collected by laboratory X-ray sources, synchrotron powder diffraction data have a higher resolution, and allow us to use it as a reference to compare our modeled powder diffraction patterns.

The fitting range used in our PDF analyses extended from 1 to 30 Å, which is longer than the three lattice parameters of the structural models used as input in the analyses. This implies that the long-range order arising from repetitions along the unit cell axes is already

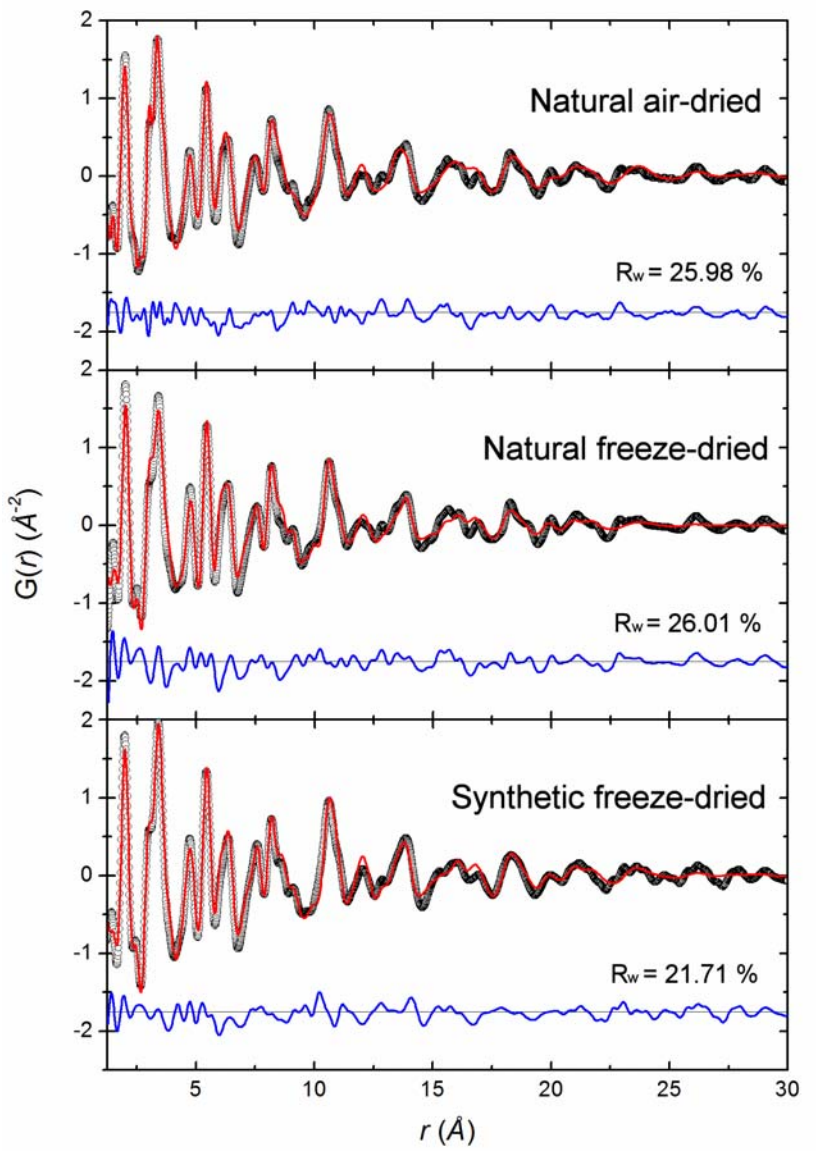


Figure 4. *Experimental PDF data (black circles) fitted by the refined model PDF (red line). A difference plot (blue line) is included beneath each data set.*

σ_{ij} (GPa)	*x*	*y*	*z*
x	2.93	-0.29	**2.40**
y	-0.29	12.36	0.64
z	**2.40**	0.64	3.2

Table 3. *Stress tensor calculated at the initial step of the DFT-geometry optimization of the sulfate-doped akaganeite structure. The off diagonal elements* σ_{xz} *and* σ_{zx} *indicate a shear stress responsible of the deformation of the angle* β*.*

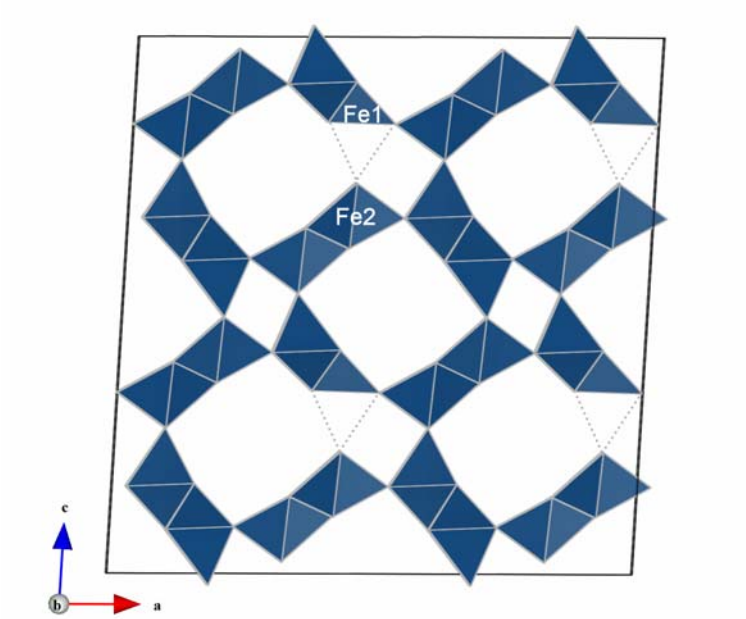


Figure 5. *2×1×2 supercell of the Model 1 obtained after PDF fitting. Only the positions of the iron atoms were refined. The distance from Fe1 to Fe2 is too long to form two corner-sharing octahedral (illustrated with dotted line).*

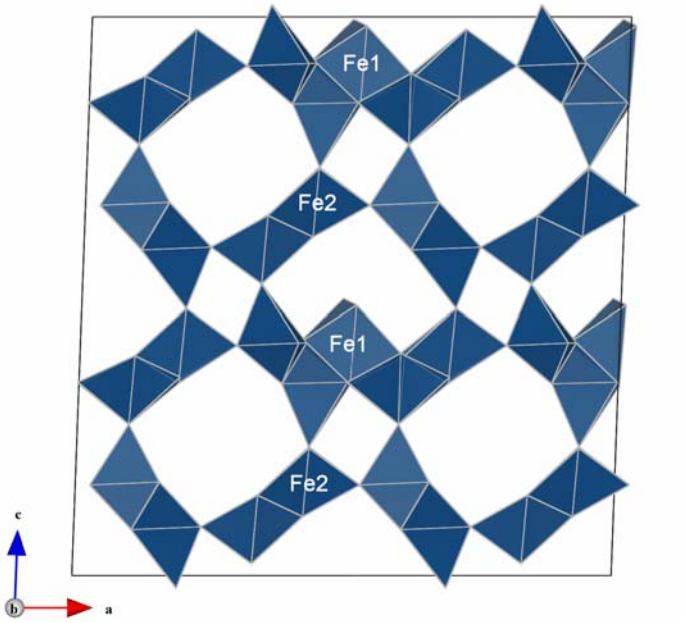


Figure 6. *2×1×2 supercell of the Model 2 obtained after PDF fitting. Only the positions of the iron atoms were refined. The Fe1 octahedron is turned by 90º, sharing two edges with two neighbouring iron atoms.*

taken into account in the PDF analysis, and thus the resulting structure should reproduce both short-range and long-range order along the three directions of space. In order to check this consistency we have calculated theoretical powder diffraction patterns of the refined structures, varying the number and positions of the sulfates molecules within the unit cell.

The calculated diffraction patterns of schwertmannite Models 1 and 2 are presented in Figure 8, and compared to the experimental patterns. Positions and intensities of the diffraction lines are given in Table 4. It is important to note that, due to the different *a* and *c* lattice parameters, originally single peaks of akaganeite are split into two or more different peaks (see Table 4). However, due to the small coherent domain sizes of schwertmannite, these split reflections overlap, being impossible to accurately determine their positions and intensities. This high degree of overlapping has made impossible the application of analysis techniques as Le Bail fits, which would be very useful to precisely determine the cell parameters. From now on, we will continue to use the original notation of akaganeite when referring to the diffraction lines, even though some of them are composed by several overlapping reflections (see Table 4 for a complete list of reflections of Model 1).

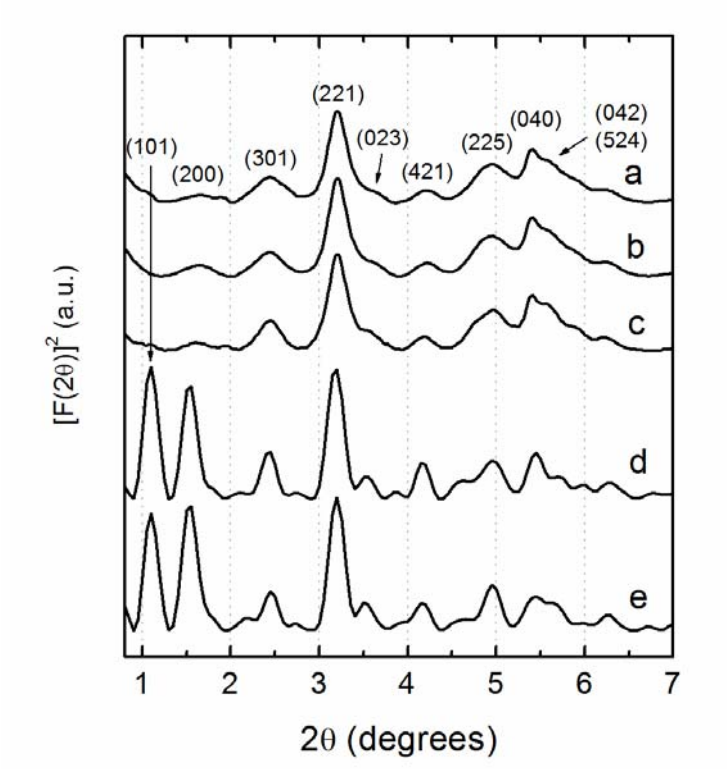


Figure 8. *Diffraction patterns of (a) Natural air-dried schwertmannite. (b) Natural freeze-dried schwertmannite. (c) Synthetic freeze-dried schwertmannite. (d) Model 1. (e) Model 2.*

There are only small differences between the two models, the most significative being a higher intensity in the (042) and (524) reflections of Model 2, which agrees better with the observed experimentally. The calculated patterns are in quite good agreement with the experimental ones, except for the intensities of some lines. The (040) reflection is lower in the Model 1 and 2 patterns than in the experiments and the (200) and (101) reflections have higher intensity in the models. This is especially true for the (101) reflection, which is absent in the experimental patterns. Bigham et al. (Bigham et al., 1990) observed how the intensity of this reflection decreased proportionally to the amount of sulfate added during the precipitation of akaganeite. They found that schwertmannite was the only precipitation product formed when the synthesis was made in the presence of 2000 ppm of sulfate. The precipitate showed the typical 8 diffraction lines characteristic of schwertmannite, with the akaganeite (101) reflection absent. We have checked this correlation between the intensity of the (101) line and the unit cell sulfate content by generating a series of diffraction patterns of the schwertmannite structure obtained from the PDF analysis loaded with different amounts of sulfate molecules. Only two different kind of sulfate molecules were considered: (1) a bidentate inner-sphere complex placed sharing two oxygens with the iron frame, as shown in Figure 9a (the shared oxygens were chosen so they have same *x* and *z* coordinates, but placed at a different *y* coordinate), and (2) an outer-sphere complex placed in the center of the channel, as shown in Figure 9a. All the calculations were performed using the structure of Model 1 for the octahedral iron frame. The results are presented in Figure 9, b. Only the intensities of the reflections (101), (200), (301), (023), (042) and (524) are sensitive to the concentration of sulfate molecules in the structure and to their positions within the unit cell. The most important variations of intensity are found for the diffraction peaks (101), (200) and (301), as shown in Figure 9, c-e. The intensity of the (101) peak decreases as long as more sulfates are introduced in the channel of the octahedral iron frame of schwertmannite, as reported by Bigham (Bigham et al., 1990). The best result, with the (101) reflection practically absent, is found when four sulfates forming outer-sphere complexes are present in the structure. The evolution of the (200) and (301) intensity shows opposite behaviors, being the intensity of these two peaks dependent on the positions of the sulfate within the structure. Their relative peak intensities have been calculated using the intensity of line (221) (the more intense in the experimental patterns), and are presented in Table 5.

h	k	l	d_{hkl} (Å)	2-theta (º)	I / I_{max}
1	0	1	7.6013	1.0743	36.08
1	0	-1	7.3252	1.1148	87.6
0	0	2	5.3742	1.5195	100
2	0	0	5.1804	1.5763	25.04
1	0	2	4.8444	1.6857	11.32
1	0	3	3.4254	2.3841	11.76
1	0	-3	3.348	2.4392	11.65
3	0	1	3.324	2.4568	14.89
3	0	-1	3.2532	2.5103	14.85
0	0	4	2.6871	3.0393	15.61
4	0	0	2.5902	3.153	24.15
1	2	2	2.5659	3.1828	11.67
1	-2	2	2.5659	3.1828	12.84
2	2	1	2.5494	3.2035	15.43
2	-2	1	2.5494	3.2035	15.6
1	-2	-2	2.5438	3.2105	6.21
1	2	-2	2.5438	3.2105	5.25
4	0	1	2.5396	3.2158	10.9
3	0	3	2.5338	3.2232	4.59
2	-2	-1	2.5276	3.231	18.38
2	2	-1	2.5276	3.231	20.49
3	0	-3	2.4417	3.3447	10.51
0	2	3	2.3114	3.5334	9.03
0	2	-3	2.3114	3.5334	8.84
1	2	-4	1.9621	4.1626	5.83
1	-2	-4	1.9621	4.1626	6.26
4	2	1	1.9451	4.1992	5.46
4	-2	1	1.9451	4.1992	5.77
0	0	6	1.7914	4.5596	13.99
6	0	0	1.7268	4.7302	7.57
2	2	5	1.6753	4.8756	6.86
2	-2	5	1.6753	4.8756	6.44
2	-2	-5	1.6449	4.9658	11.51
2	2	-5	1.6449	4.9658	11.43
5	-2	2	1.6437	4.9696	6.71
5	2	2	1.6437	4.9696	6.73
5	2	-2	1.6149	5.0581	6.39
5	-2	-2	1.6149	5.0581	6.28
5	2	3	1.5615	5.2311	4.8
5	-2	3	1.5615	5.2311	4.82
0	4	0	1.5126	5.4006	19.42
5	2	4	1.4627	5.5847	2.96
5	-2	4	1.4627	5.5847	2.96
0	4	-2	1.456	5.6106	2.58
0	4	2	1.456	5.6106	2.1
7	0	2	1.4407	5.6703	3.15
5	-2	-4	1.4228	5.7415	4.95
3	0	7	1.4227	5.7419	2.58

Table 4. *X-ray powder reflections of structural 'model 1' of schwertmannite. Only the reflections with $I / I_{max} > 2$ are presented. The 2-theta is related to our experimental conditions, with wavelength $\lambda = 0.14252$ Å.*

A maximum intensity for the (200) reflection is found when four inner-sphere complexes are present in the structure. On the other hand, a maximum is found for the (301) peak for the structure with four outer-sphere complexes. The relative intensities of these two peaks can thus be used to evaluate the sulfate content and the binding mechanisms to the structure, by comparison to the experimental values (see Table 5). Simulations of structures where sulfates are present both as inner and outer-sphere complexes were then performed in order to better reproduce the experimental data. The results are presented in Figure 10, and compared with the experimental data. Relative intensities are reported in Table 5.

Structure	$I_{(101)}/I_{(221)}$	$I_{(200)}/I_{(221)}$	$I_{(301)}/I_{(221)}$
No SO_4	1.28	0.78	0.48
1 SO_4 IS	1.06	0.79	0.42
2 SO_4 IS	0.93	0.81	0.37
1 SO_4 OS	0.78	0.59	0.57
4 SO_4 IS	0.69	0.88	0.28
2 SO_4 OS	0.43	0.42	0.68
4 SO_4 OS	0.05	0.13	0.95
Natural air-dried schwertmannite	**0.04**	**0.08**	**0.28**
2 SO_4 IS + 2 SO_4 OS	0.29	0.38	0.52
4 SO_4 IS + 2 SO_4 OS	0.20	0.48	0.41
2 SO_4 IS + 2 SO_4 OS + 8 H_2O	**0.11**	**0.26**	**0.47**

Table 5. *Values of the relative intensity of the (101), (200) and (301) reflections for different structures with Inner-Sphere (IS) and Outer-Sphere (OS) sulfate complexes. The intensity of the (221) reflection is used as reference. The best agreement is highlighted in bold fonts.*

If only sulfates are considered to be present, none of the combinations made match the relative intensities found in the experimental patterns (see, for example, the intensity ratios of the structure with 4 outer-sphere SO_4 complexes in Table S3, which yield good $I_{(101)}/I_{(221)}$ and $I_{(200)}/I_{(221)}$ but very bad agreement for the $I_{(301)}/I_{(221)}$). For this reason, we have considered the case where water is present in the structure. This hypothesis is supported by thermo-gravimetric data of Yu et al. (1999), who reported a range of 8.5 to 8.9 water molecules per unit cell, and it seems to be very reasonable in view of the exchange processes taking place between sulfates and other oxyanions, which are hydrated species.

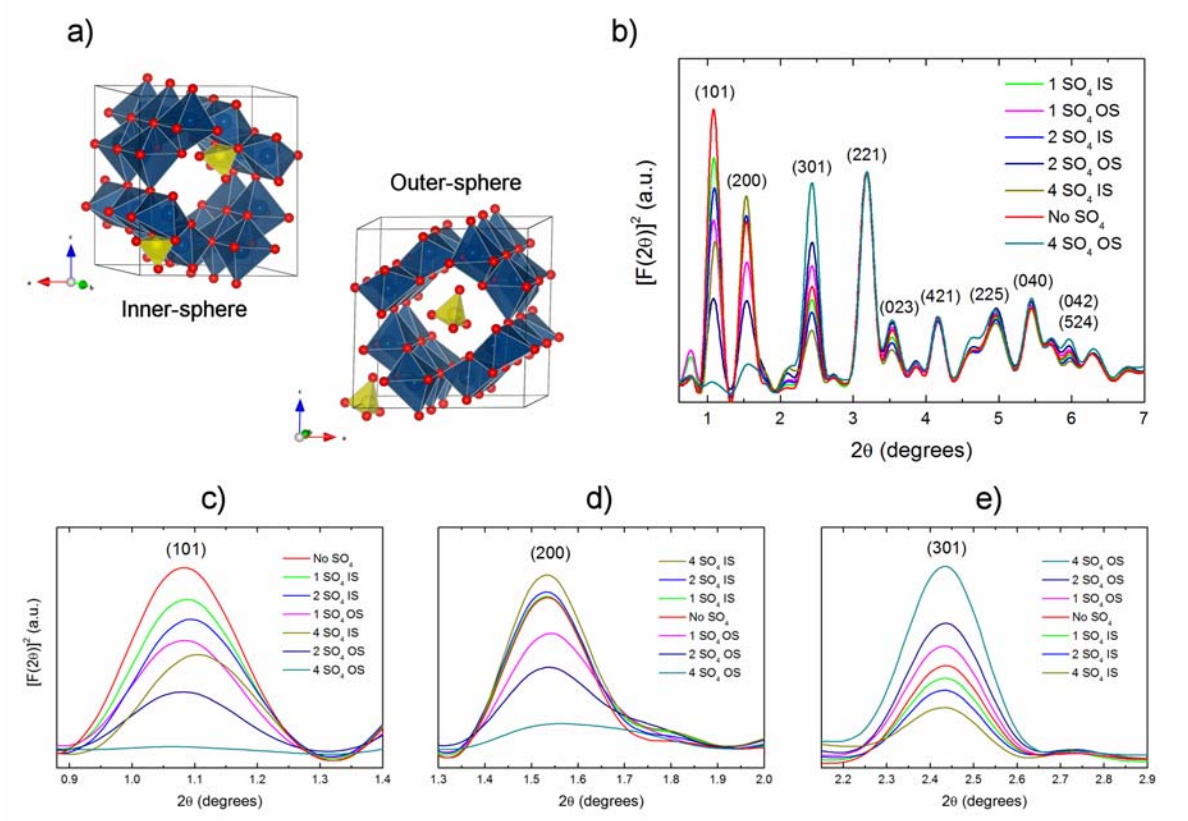


Figure 9. *Diffraction patterns of Model 1 loaded with different amounts of sulfate molecules.*

Preliminary calculations including 9 molecules per cell do improve the agreement with the experimental XRD pattern (see Figure 10). The determination of the exact positions of the water molecules within the unit cell is challenging, especially using X-ray radiation as experimental probe. The use of DFT calculations is also limited by the fact that there are many degrees of freedom in the system, and it becomes thus difficult to explore all the possibilities of the positions of water molecules and outer-sphere sulfate molecules. For these reasons, the water molecules were placed in the structure with the only care that the minimum distance between atoms from different water molecules was 1.8 Å, as expected from hydrogen bonded water molecules. The best agreement with the experiment, as reported in Table 5, is found for the structure containing two outer-sphere and two inner-sphere complexes with 8 water molecules per unit cell. This explains the range of stoichiometry reported for the mineral formula, with SO_4 varying from 2 to 3.72 each 16 Fe atoms (Bigham et al., 1994; Yu et al., 1999). The lower limit is coincident with the number of inner-sphere complexes in the structure, whereas the rest corresponds to outer-sphere complexes. This result suggests that the variability in the sufate content may come from the

different amounts of outer-sphere sulfate complexes, which may be energetically less stable than inner-sphere complexes.

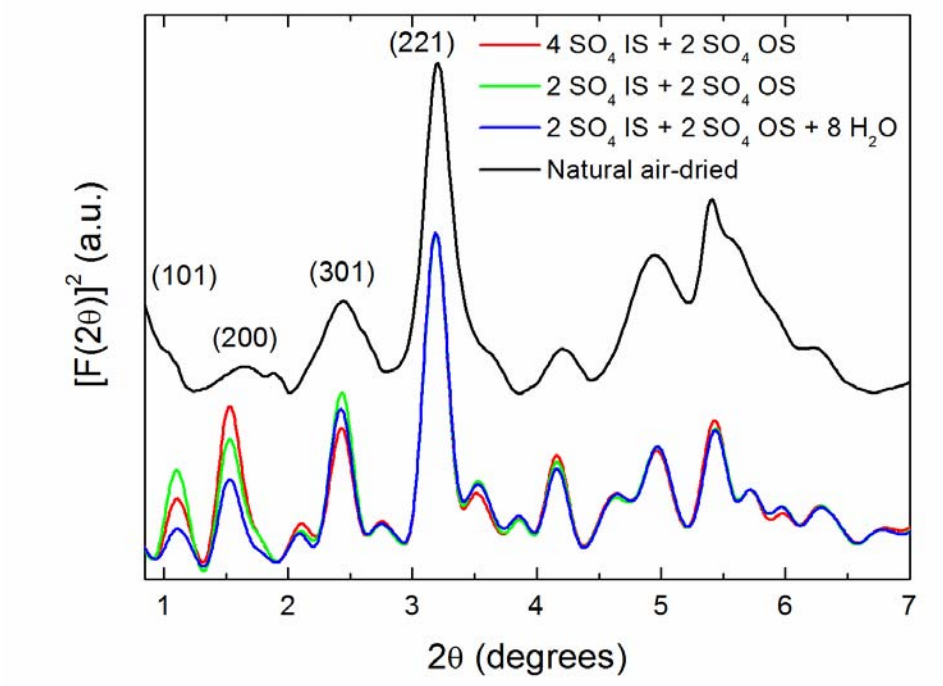


Figure 10. *Diffraction patterns of natural air-dried schwertmannite and of Model 1 loaded with different amounts of sulfate and water molecules.*

CONCLUSIONS

During the last 15 years, the structure of schwertmannite was supposed to be similar to the akaganeite structure, due to the similarities of the diffraction patterns of both minerals. However, the poor crystallinity of schwertmannite has hindered any detailed structural analysis. Here, a structure for the octahedral iron frame of schwertmannite is proposed based on PDF data. The PDF technique is sensitive to the correlations between iron atoms. We have found that a structure with a slightly distorted unit cell ($\beta \approx 87^{\circ}$) fits well the experimental PDF. DFT calculations support the occurrence of this deformation, suggesting that inner-sphere complexes of sulfate molecules are responsible for the deformation.

The simulations of X-ray diffraction patterns presented here explore different variables as the amount and positions of sulfates within the unit cell, that are determinant to get a good agreement between experimental and calculated patterns. The occurrence of a mixture of outer-sphere and inner-sphere complexes of sulfate is needed to get a good agreement

with the relative intensities of the (200) and (301) diffraction peaks. The total number of sulfates is inversely proportional to the intensity of the (101) reflection, which is not present in schwertmannite. Other experimental values, like a maximum number of sulfates of 3.72 sulfates per unit cell, provide a constraint to our models, suggesting that some water molecules have to be present in the structure to get better agreement with the experimental relative intensities. For this reason, we propose a structure where two sulfates form bidentate inner-sphere complexes, other two form outer-sphere complexes and eight water molecules are present. This structure is in good agreement with FTIR observations (Bigham et al., 1994), which suggest the presence of inner-sphere sulfate complexes, and with the suggestion by Waychunas et al. (Waychunas et al., 2001) that both outer and inner-sphere complexes are present in the structure.

This proposed structure allows interpreting an eventual transformation to goethite in structural terms. Goethite has an orthorhombic unit cell, with a rectangular pore extending along the *c* axis. The transformation of schwertmannite to goethite should include at least two steps: (1) the release of the sulfate molecules from the structure and (2) the release of two iron octahedra, leading to the transformation of the squared schwertmannite channel to the rectangular one present in goethite. The loosening of the interactions between the iron octahedra observed experimentally in this work (Figure 2) makes that the step (2) would be facilitated.

The small size of the coherent domain found in the fits of the PDFs adds further complexity to the analyses and interpretations of the structure. It can be interpreted in two ways: as a result of structural disorder (vacancies, strains…) or as a real limit of a less defective nanoparticle. In the last case, the occurrence of adsorption sites at the external surface of the nanoparticle would influence the symmetry of the sulfate complexes. We have limited our analysis to the bulk phase, not considering schwertmannite crystallites' external surfaces. Further spectroscopic studies would be required to complete the information presented in this work and to get more precise constraints for the symmetry of sulfate within the structure of schwertmannite.

SUPPLEMENTARY INFORMATION

PDF-refined structures of the octahedral iron frame of schwertmannite are provided in accompanying .cif files.

ACKNOWLEDGEMENTS

The authors thank Ian C. Bourg, Laurent Charlet and Andreas C. Scheinost for fruitful discussions during the preparation of the manuscript. A.F.-M. thanks the French Minister of National Education and Research for an 'Allocation de Recherche', and the Région Rhône-Alpes, France for an 'EXPLORA-DOC Fellowship'. The work has been funded by the Spanish R+D contract CTM2007-66724-C02-01/TECNO and a grant of the Catalonia Supercomputing Centre (CESCA). GRR thanks the Spanish Minister of Science and Innovation and the Ramón y Cajal Programme.

References

Acero, P., Ayora, C., Torrento, C., and Nieto, J.M. (2006) The behavior of trace elements during schwertmannite precipitation and subsequent transformation into goethite and jarosite. Geochimica et Cosmochimica Acta, 70(16), 4130-4139.

Barham, R.J. (1997) Schwertmannite: A unique mineral, contains a replaceable ligand, transforms to jarosites, hematites, and/or basic iron sulfate. Journal of Materials Research, 12(10), 2751-2758.

Bigham, J.M., Carlson, L., and Murad, E. (1994) Schwertmannite, a new iron oxyhydroxysulphate from Pyhasalmi, Finland, and other localities. Mineralogical Magazine, 58(393), 641-648.

Bigham, J.M., Schwertmann, U., Carlson, L., and Murad, E. (1990) A poorly crystallized oxyhydroxysulfate of iron formed by bacterial oxidation of Fe(II) in acid-mine waters. Geochimica et Cosmochimica Acta, 54(10), 2743-2758.

Bigham, J.M., Schwertmann, U., Traina, S.J., Winland, R.L., and Wolf, M. (1996) Schwertmannite and the chemical modeling of iron in acid sulfate waters. Geochimica et Cosmochimica Acta, 60(12), 2111-2121.

Burton, E.D., Bush, R.T., Sullivan, L.A., and Mitchell, D.R.G. (2007) Reductive transformation of iron and sulfur in schwertmannite-rich accumulations associated with acidified coastal lowlands. Geochimica et Cosmochimica Acta, 71(18), 4456-4473.

Carlson, L., Bigham, J.M., Schwertmann, U., Kyek, A., and Wagner, F. (2002) Scavenging of as from acid mine drainage by schwertmannite and ferrihydrite: A comparison with synthetic analogues. Environmental Science & Technology, 36(8), 1712-1719.

Chupas, P.J., Qiu, X.Y., Hanson, J.C., Lee, P.L., Grey, C.P., and Billinge, S.J.L. (2003) Rapid-acquisition pair distribution function (RA-PDF) analysis. Journal of Applied Crystallography, 36, 1342-1347.

Clark, S.J., Segall, M.D., Pickard, C.J., Hasnip, P.J., Probert, M.J., Refson, K., and Payne, M.C. (2005) First principles methods using CASTEP. Zeitschrift Fur Kristallographie, 220(5-6), 567-570.

Daniels, J.E., and Drakopoulos, M. (2009) High-energy X-ray diffraction using the Pixium 4700 flat-panel detector. Journal of Synchotron Radiation, 16, 1-6.

Egami, T., and Billinge, S.J.L. (2003) Underneath the Bragg Peaks: Structural analysis of complex materials. Pergamon, Elsevier.

Farrow, C.L., Juhas, P., Liu, J.W., Bryndin, D., Bozin, E.S., Bloch, J., Proffen, T., and Billinge, S.J.L. (2007) PDFfit2 and PDFgui: computer programs for studying nanostructure in crystals. Journal of Physics: Condensed Matter, 19, 335219-335226.

Gagliano, W.B., Brill, M.R., Bigham, J.M., Jones, F.S., and Traina, S.J. (2004) Chemistry and mineralogy of ochreous sediments in a constructed mine drainage wetland. Geochimica et Cosmochimica Acta, 68(9), 2119-2128.

Gilbert, B. (2008) Finite size effects on the real-space pair distribution function of nanoparticles. Journal of Applied Crystallography, 41, 554-562.

Greffie, C., Amouric, M., and Parron, C. (2001) HRTEM study of freeze-dried and untreated synthetic ferrihydrites: consequences of sample processing. Clay Minerals, 36(3), 381-387.

Guinier, A. (1994) X-Ray Diffraction in Crystals, Imperfect Crystals, and Amorphous Bodies. Dover Publications Inc.

Hammersley, A.P., Svensson, S.O., Hanfland, M., Fitch, A.N., and Hausermann, D. (1995) Two-dimensional detector software: From real detector to idealised image or two-theta scan. 4th Workshop of the IUCr High Pressure Group on Synchrotron and Neutron Sources, p. 235-248, Kek, Japan.

Jonsson, J., Persson, P., Sjoberg, S., and Lovgren, L. (2005) Schwertmannite precipitated from acid mine drainage: phase transformation, sulphate release and surface properties. Applied Geochemistry, 20(1), 179-191.

Loan, M., Cowley, J.M., Hart, R., and Parkinson, G.M. (2004) Evidence on the structure of synthetic schwertmannite. American Mineralogist, 89(11-12), 1735-1742.

Michel, F.M., Antao, S.M., Chupas, P.J., Lee, P.L., Parise, J.B., and Schoonen, M.A.A. (2005) Short- to medium-range atomic order and crystallite size of the initial FeS precipitate from pair distribution function analysis. Chemistry of Materials, 17(25), 6246-6255.

Michel, F.M., Ehm, L., Antao, S.M., Lee, P.L., Chupas, P.J., Liu, G., Strongin, D.R., Schoonen, M.A.A., Phillips, B.L., and Parise, J.B. (2007a) The structure of ferrihydrite, a nanocrystalline material. Science, 316(5832), 1726-1729.

Michel, F.M., Ehm, L., Liu, G., Han, W.Q., Antao, S.M., Chupas, P.J., Lee, P.L., Knorr, K., Eulert, H., Kim, J., Grey, C.P., Celestian, A.J., Gillow, J., Schoonen, M.A.A., Strongin, D.R., and Parise, J.B. (2007b) Similarities in 2-and 6-line ferrihydrite based on pair distribution function analysis of X-ray total scattering. Chemistry of Materials, 19(6), 1489-1496.

Peak, D., Ford, R.G., and Sparks, D.L. (1999) An in situ ATR-FTIR investigation of sulfate bonding mechanisms on goethite. Journal of Colloid and Interface Science, 218(1), 289-299.

Perdew, J.P., Burke, K., and Ernzerhof, M. (1996) Generalized gradient approximation made simple. Physical Review Letters, 77(18), 3865-3868.

Post, J.E., Heaney, P.J., Von Dreele, R.B., and Hanson, J.C. (2003) Neutron and temperature-resolved synchrotron X-ray powder diffraction study of akaganeite. American Mineralogist, 88(5-6), 782-788.

Qiu, X.Y., Bozin, E.S., Juhas, P., Proffen, T., and Billinge, S.J.L. (2004) Reciprocal-space instrumental effects on the real-space neutron atomic pair distribution function. Journal of Applied Crystallography, 37, 110-116.

Regenspurg, S., and Peiffer, S. (2005) Arsenate and chromate incorporation in schwertmannite. Applied Geochemistry, 20(6), 1226-1239.

Rotting, T.S., Caraballo, M.A., Serrano, J.A., Ayora, C., and Carrera, J. (2008) Field application of calcite Dispersed Alkaline Substrate (calcite-DAS) for passive treatment of acid mine drainage with high Al and metal concentrations. Applied Geochemistry, 23(6), 1660-1674.

Scheinost, A.C., Kirsch, R., Banerjee, D., Fernandez-Martinez, A., Zaenker, H., Funke, H., and Charlet, L. (2008) X-ray absorption and photoelectron spectroscopy investigation of selenite reduction by Fe-II-bearing minerals. Journal of Contaminant Hydrology, 102(3-4), 228-245.

Schwertmann, U., and Cornell, R.M. (1991) Iron Oxides in the Laboratory: Preparation and Characterization. Wiley-VCH.

Toby, B.H., and Egami, T. (1992) Accuracy of Pair Distribution Function analysis applied to crystalline and noncrystalline materials. Acta Crystallographica Section A, 48, 336-346.

Waychunas, G.A., Myneni, S.C.B., Traina, S.J., Bigham, J.M., Fuller, C.C., and Davis, J.A. (2001) Reanalysis of the Schwertmannite structure and the incorporation of SO_4^{2-} groups: An IR, XAS, WAXS and simulation study. Eleventh Annual V. M. Goldschmidt Conference.

Waychunas, G.A., Xu, N., Fuller, C.C., Davis, J.A., and Bigham, J.M. (1995) XAS study of AsO_4^{3-} and SeO_4^{2-} substituted in Schwertmannites. Physica B, 208-209, 481-483.

Yu, J.Y., Heo, B., Choi, I.K., Cho, J.P., and Chang, H.W. (1999) Apparent solubilities of schwertmannite and ferrihydrite in natural stream waters polluted by mine drainage. Geochimica et Cosmochimica Acta, 63(19-20), 3407-3416.

Chapter 6

Conclusions

The research activity carried out during this thesis work was aimed to explore the external mineral – water interface of imogolite nanotubes, the ability of imogolite to form strong complexes with selenium oxyanions, and the structure of schwertmannite nanoparticles.

The application of Molecular Dynamics (MD) techniques to the study of water adsorption onto gibbsite and imogolite has revealed differences in the strength of the interactions on both surfaces. The planar structure of gibbsite allows the formation of strong hydrogen bonds between adjacent surface hydroxyl groups. On gibbsite, 5/6 of the surface hydroxyl groups are parallel to the surface, allowing the adsorption of a water molecule donating a hydrogen bond to a surface oxygen atom. This water molecule (A-type) is oriented with a OH pointing perpendicularly to the surface, and it is strongly adsorbed. The curvature of imogolite makes that only 1/3 of the surface hydroxyl groups are parallel to the surface, preventing the adsorption of A-type water molecules, and making the imogolite surface less hydrophilic than that of gibbsite. The curvature of the surface is thus a key parameter controlling the orientation of the hydroxyl groups and thus the hydrophilicity of the mineral surfaces. This result has important implications in the reactivity of natural nanoparticles. Usually, the 'nano' effect is expected to come from atomic surface relaxation processes, as it happens for instance in gold nanoparticles, with structures very different than their bulk counterparts (Gilbert et al., 2004). This study shows that, even in the absence of atomic structural relaxations, the reactivity of mineral nanoparticles with surfaces populated by hydroxyls groups can be very different from the reactivity expected from minerals with large crystal faces.

The curvature effect can also be observed on the formation of a less structured second shell of water at the imogolite surface with respect to gibbsite. This effect can

have implications in the adsorption properties of imogolite. The formation of a structured shell of adsorbed water, as the one observed on the gibbsite surface, can be understood as a new pseudo-layer to which ions can adsorb, forming outer-sphere complexes. MD simulations studying the free energy profiles of adsorption as a function of the distance to the mineral surface will be useful to study this effect.

In addition, patching effects similar to those described by other authors on the surfaces of calcite have been described (Rahaman et al., 2008). Little is known today about the importance of these patches regarding the adsorption properties of ions. It is interesting to note that in this study, gibbsite has been reported to have a higher percentage of surface sites non-coordinated to water molecules than imogolite (26% on gibbsite *vs*. 19% on imogolite). But, at the same time, selenate ions have been reported to form inner-sphere complexes at the surface of imogolite (Chapter 3), while they only form outer-sphere complexes at the gibbsite (001) surface (Papelis et al., 1995). These two results could indicate that the patching effects do not have any influence on the adsorption of selenate ions. New studies focusing on the reactivity of these 'dry' sites should be performed in the future.

Water Gibbs free energies of adsorption have been calculated revealing a hydrophilic behavior for both surfaces, with a difference of $\Delta\Delta G$ = -2.19 kcal/mol between them, being the surface of imogolite more hydrophobic. The ability of allophanic Andosols to accumulate organic matter is well known (Basile-Doelsch et al., 2005; Dynes and Huang, 1997). The relative hydrophobicity of imogolite provides a favorable environment for the adsorption of organic molecules, prior to the formation of inner-sphere complexes between the imogolite surface hydroxyl groups and the carboxyl groups present in organic compounds. Our simulations shed light to another important property of imogolite: its tendency to form bundles. It has been shown using MD simulations that the free energy profile of aggregation of two mineral particles is governed by the energy barriers created upon the formation of a shell of highly ordered water between the mineral surfaces (Spagnoli et al., 2008). In the case of imogolite this shell of adsorbed water is less structured, and a lower energy barrier is expected to occur, thus facilitating the aggregation between different nanotubes. MD simulations exploring these effects are ongoing.

The finding of inner-sphere complexation for the two selenium oxyanions at the imogolite – water interface has important implications for the correct assessment of selenium deficit causes and effects in volcanic environments. The formation of inner-

sphere complexes involves the formation of covalent bonds, immobilizing the selenium oxyanions at the surface of imogolite. This strong mechanism of retention can affect the uptake of selenium oxyanions by plants, limiting the concentrations of selenium entering the food chain. This adsorption mechanism is thus proposed as responsible (at least in part) for the low bioavailability of selenium in volcanic soils, a problematic reported by some authors (Reilly, 1997; Stone, 2009). The use of molecular modeling has allowed us to describe a competition for the adsorption site between the A-type water molecules and the selenite molecules. The adsorption of selenite molecules has to be preceded by the removal of water from the adsorption sites.

The structure of the water H-bonding at imogolite and gibbsite−water interfaces has been evaluated in terms of the protonation constants. MD simulations reveal a more ordered and stronger network of H-bonded surface OH groups at the surface of gibbsite. The curvature of imogolite prevents the formation of some H-bonds between surface OH groups. This yields different values of the bond valences attributed to bonds between surface oxygen atoms and water molecules, which result in more acidic pK_{a1} values for imogolite doubly-coordinated neutral sites by $\Delta pK_{a1} = 0.87 \pm 0.75$. The absolute values of the protonation constants reported in this work coincide with those reported by (Hiemstra and VanRiemsdijk, 1996), who used the same CD-MUSIC model, but are in disagreement with the values reported by others. Spectroscopic studies focused on the exploration of the atomic structures at mineral−water interfaces are needed in order to obtain better structural descriptions allowing to develop reliable surface chemistry models.

During the last 15 years, the structure of schwertmannite was supposed to be similar to the akaganeite structure, due to the similarities of the diffraction patterns of both minerals. However, the poor crystallinity of schwertmannite had hindered any detailed structural analysis. The use of the PDF technique has allowed us to describe the structure of the octahedral iron frame of schwertmannite. The PDF technique is sensitive to the correlations between iron atoms. We have found that a structure with a slightly distorted unit cell ($\beta \approx 87^{o}$) fits well the experimental PDF. DFT calculations support the occurrence of this deformation, suggesting that inner-sphere complexes of sulfate molecules are responsible for the deformation.

The simulations of X-ray diffraction patterns presented here explore different variables as the amount and positions of sulfates within the unit cell, that are determinant to get a good agreement between experimental and calculated patterns. The

occurrence of a mixture of outer-sphere and inner-sphere complexes of sulfate is needed to get a good agreement with the relative intensities of the (200) and (301) diffraction peaks. The total number of sulfates is inversely proportional to the intensity of the (101) reflection, which is not present in schwertmannite. Other experimental values, like a maximum number of 3.72 sulfates per unit cell, provide a constraint to our models, suggesting that some water molecules have to be present in the structure to get better agreement with the experimental relative intensities. For this reason, we propose a structure where two sulfates form bidentate inner-sphere complexes, other two form outer-sphere complexes and eight water molecules are present. This structure is in good agreement with FTIR observations (Bigham et al., 1994), which suggest the presence of inner-sphere sulfate complexes, and with the suggestion by Waychunas et al. (Waychunas et al., 2001) that both outer and inner-sphere complexes are present in the structure.

REFERENCES

Ackerman, W.C., Smith, D.M., Huling, J.C., Kim, Y.W., Bailey, J.K., and Brinker, C.J. (1993) Gas vapor adsorption in imogolite - A microporous tubular aluminosilicate. Langmuir, 9(4), 1051-1057.

Basile-Doelsch, I., Amundson, R., Stone, W.E.E., Masiello, C.A., Bottero, J.Y., Colin, F., Masin, F., Borschneck, D., and Meunier, J.D. (2005) Mineralogical control of organic carbon dynamics in a volcanic ash soil on La Reunion. European Journal of Soil Science, 56(6), 689-703.

Bigham, J.M., Carlson, L., and Murad, E. (1994) Schwertmannite, a new iron oxyhydroxysulphate from Pyhasalmi, Finland, and other localities. Mineralogical Magazine, 58(393), 641-648.

Dynes, J.J., and Huang, P.M. (1997) Influence of organic acids on selenite sorption by poorly ordered aluminum hydroxides. Soil Science Society of America Journal, 61(3), 772-783.

Gilbert, B., Huang, F., Zhang, H.Z., Waychunas, G.A., and Banfield, J.F. (2004) Nanoparticles: Strained and stiff. Science, 305(5684), 651-654.

Hiemstra, T., and VanRiemsdijk, W.H. (1996) A surface structural approach to ion adsorption: The charge distribution (CD) model. Journal of Colloid and Interface Science, 179(2), 488-508.

Papelis, C., Brown, G.E., Parks, G.A., and Leckie, J.O. (1995) X-Ray-Absorption Spectroscopic Studies of Cadmium and Selenite Adsorption on Aluminum-Oxides. Langmuir, 11(6), 2041-2048.

Rahaman, A., Grassian, V.H., and Margulis, C.J. (2008) Dynamics of water adsorption onto a calcite surface as a function of relative humidity. Journal of Physical Chemistry C, 112(6), 2109-2115.

Reilly, C. (1997) Selenium in food and health. 360 p. Blackie Academic & Professional, London.

Spagnoli, D., Banfield, J.F., and Parker, S.C. (2008) Free energy change of aggregation of nanoparticles. Journal of Physical Chemistry C, 112(38), 14731-14736.

Stone, R. (2009) A Medical Mystery in Middle China. Science, 324(5933), 1378-1381.

Waychunas, G.A., Myneni, S.C.B., Traina, S.J., Bigham, J.M., Fuller, C.C., and Davis, J.A. (2001) Reanalysis of the Schwertmannite structure and the incorporation of SO_4^{2-} groups: An IR, XAS, WAXS and simulation study. Eleventh Annual V. M. Goldschmidt Conference.

Annex I

Multi-scale characterization of synthetic imogolite

Since the development of the first methods for the synthesis of imogolite by (Farmer et al., 1977; Wada et al., 1979) many works have reported the existence of a certain diameter polydispersity (Barrett et al., 1991; Farmer et al., 1983; Wada, 1987; Wada et al., 1979). There is general agreement that natural imogolite has smaller external diameters than the synthetic one ($d_{e\text{-}natural}$ = 2 nm *vs.* $d_{e\text{-}synthetic}$ = 2.1 – 2.4 nm) (Barrett et al., 1991; Ohashi et al., 2004; Wada, 1987). Imogolites with different diameters are supposed to be composed of different number of $(Al_2(OH)_3SiO_3OH)_n$ molecular units, being n = 20 for natural imogolite and n = 24 – 28 for synthetic imogolite. (Wada, 1987) synthesized imogolite at 25°C, and reported diameters similar to those of the natural material. He proposed that the elongation of the Si-O bond lengths during high temperature synthesis at high temperature (most syntheses are done at 95°C) is the responsible of the formation of imogolite with longer diameters. On the other hand, studies using theoretical *ab-initio* and classical molecular mechanics techniques have reported minimum values for the total energy at diameters corresponding to n = 24 (Guimaraes et al., 2007; Konduri et al., 2006), n = 32 (Tamura and Kawamura, 2002).

Synthetic and natural imogolite is usually found forming bundles composed of several tubes. These meso-structures have been studied by different authors using the low-angle part of diffraction patterns, and reporting a variety of different inter-tube distances. For instance, (Barrett et al., 1991) proposed a perfect hexagonal packing using synthetic imogolite, while (Mukherjee et al., 2005) proposed a quasi-hexagonal structure with a monoclinic cell in which γ = 78°, and (Alvarez-Ramirez, 2007) proposed, using theoretical methods, a value of γ = 64°.

The hydrophilic character of imogolite and the fact that it is formed under humid conditions (synthetic imogolite is formed through a sol-gel procedure) makes water an important component of imogolite. However, only few studies have focused on the

structure and dynamics of water adsorbed on imogolite (Ackerman et al., 1993; Creton et al., 2008a; Creton et al., 2008b; Farmer et al., 1983). Creton *et al.* (2008) performed Molecular Dynamics (MD) simulations of the water present in the inter-tube pores of hexagonal close-packed bundles of imogolite showing that water interacts with the silanol groups much strongly than with the aluminol groups on the external surface. It has been also shown that this strong interaction and the reduced size of the internal pore (diameter ≈ 1 nm) makes difficult the diffusion of water along the tube axis (Zang et al., 2009). (Farmer et al., 1983) reported results from a dehydration experiment, showing that when passing from 100°C to 200°C an irreversible collapse of the inter-tubular structure is found, with the diffraction maxima corresponding to the center-to-center distance passing from 2.7 to 2.3 nm. They reported a partial breakdown of the structure at 300°C and the start of dehydroxylation and a phase transition to an amorphous state at 350°C.

In addition to the characterization studies of synthetic imogolite already presented in Chapter 3, we have performed other experimental studies of this material. In this appendix, X-ray Pair Distribution Function (PDF) and Transmission Electron Microscopy (TEM) studies of synthetic imogolite will be presented. In addition, the amount of water present at the imogolite structure will be quantified using Controlled Rate Thermal Analysis (CRTA) and Fourier Transform Infrared Spectroscopy (FTIR).

MATERIALS AND METHODS

High energy X-ray Pair Distribution Function

High-energy X-ray total scattering experiments were performed at beamline ID15B of the European Synchrotron Radiation Facility, Grenoble, France. Scattering data were collected with a Pixium 4700 detector (Daniels and Drakopoulos, 2009) using the Rapid-Acquisition pair Distribution Function technique (Chupas et al., 2003). Measurements of the samples, empty capillary, and the background were made at ambient temperature in a Q-range of 0 – 25 $Å^{-1}$. The X-ray wavelength was refined using a Ni standard (λ = 0.14252 Å). Corrections for sample-detector distance, tilt angle of the detector with respect to the direction of the incident radiation and polarization were performed using Fit2D (Hammersley et al., 1995). Total scattering structure functions and Pair Distribution Functions were obtained using the PDFGetX2 software (Qiu et al., 2004). A crystalline standard (LaB_6) was measured and used to calculate the

instrumental resolution effect on the PDF (Toby and Egami, 1992). Fits of the PDFs were performed using the PDFGui software (Farrow et al., 2007).

Transmission Electron Microscopy

TEM investigations were carried out on a Philips CM 200 microscope operating at 200 kV. Prior to observation, the powders were immersed in an aqueous solution. A droplet of this solution was deposited on a copper grid. TEM observations were made after evaporation of the solvent.

Fourier Transform Infrared Spectroscopy

FTIR spectra of the imogolite freeze-dried powders were taken to characterize the product obtained after the synthesis. Transmission FTIR spectra were obtained using a Bruker HYPERION 3000 FTIR microscope in the transmission mode. KBr pellets (1 mg of imogolite in 100 mg of KBr) were used. One hundred scans taken using a resolution of 2 cm^{-1} were averaged to obtain spectra in the range 4000–370 cm^{-1}. The measurements were done using a home-made cell consisting of a vacuum chamber with a resistance heater controlled by an external unit.

Controlled-Rate Thermal Analyses (CRTA)

This technique allows performing a water desorption experiment controlling the desorption rate using a mass spectrometer at the exit of the vacuum pump. In this technique, the heating rate is controlled by the sample and it depends on the rate of desorption of adsorbed species. When desorption occurs, molecules leave the surface. This leads to a pressure increase over the sample. In order to keep the pressure constant, the heating is stopped and the system remains at constant temperature until the desorption starts to decrease. The temperature is then increased again until another significant desorption process begins. For a constant rate of vapor loss, the temperature *vs.* time data may be converted immediately into the temperature *vs.* mass loss. The use of a feedback system to control the temperature allows obtaining a significant enhancement of the resolution.

Dehydration experiments were performed using a home-made apparatus (LEM, Nancy) equipped with a turbo-molecular vacuum pump TMH 071P and a membrane vacuum pump MVP 012 (Pfeiffer). Vacuum is controlled by a PKR 251 (Pfeiffer)

gauge. The mass spectrometer is a Balzers (QMS, QMA and QME 200 Pfeiffer Vacuum).

RESULTS

Structural analyses

TEM images are shown in Figure 1. The bundle structure can be appreciated, with associations of 5 or more nanotubes arranged in parallel. Distances between tubes have been measured yielding an average value of <*d* = 2.2 nm>. In the central image of Figure 1, lengths up to 200 nm can be observed for some tubes. The image at right is an enlargement of the central one showing the structure of five tube's edges. The circular section of the tubes is appreciated, confirming that the nanotubes are open on the edges.

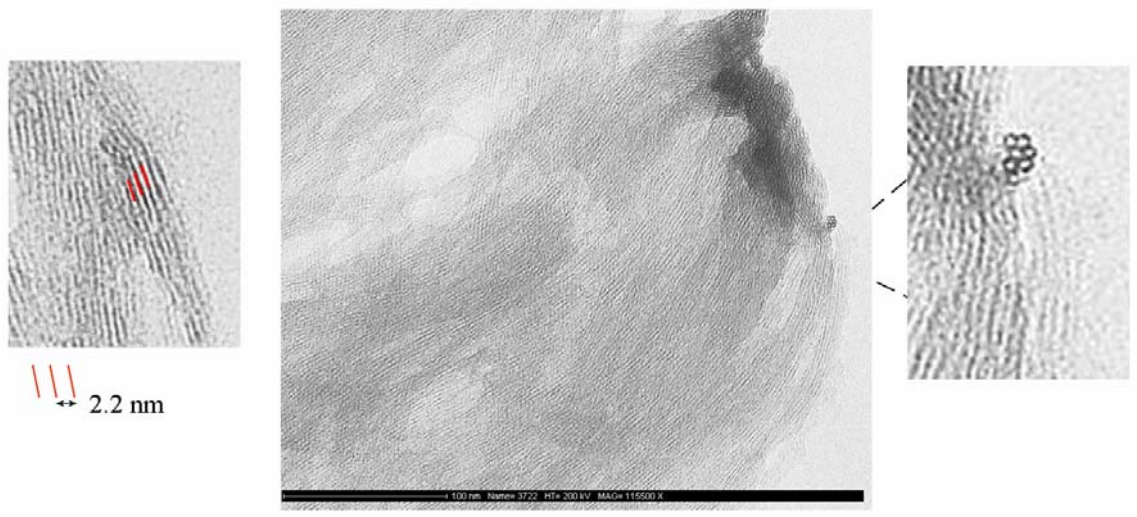


Figure 1.- *TEM micrographs of synthetic imogolite.*

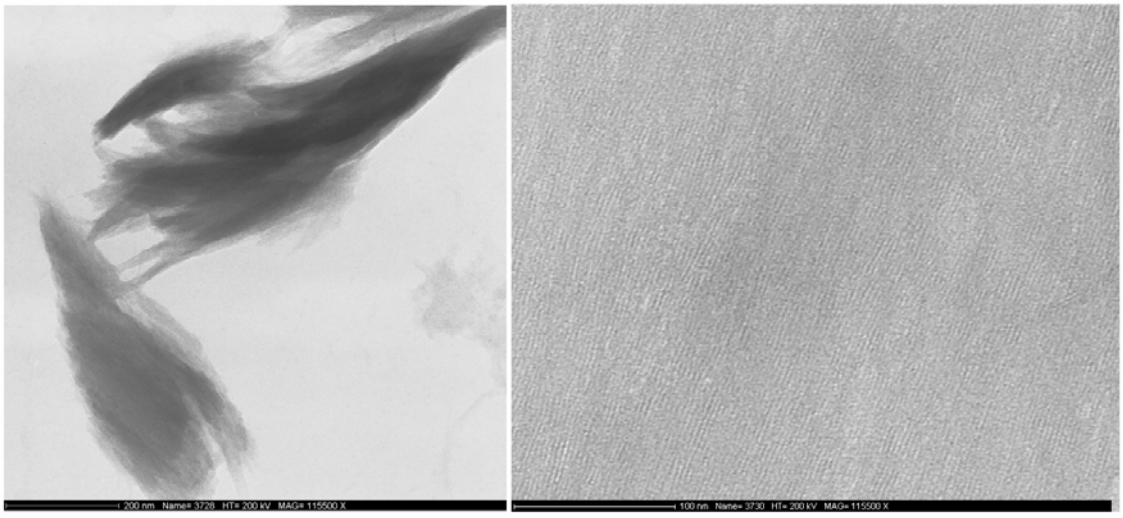


Figure 2*. TEM micrographs of oriented films of synthetic imogolite.*

Figure 2 shows a sample of synthetic imogolite dried following a roto-evaporation procedure. The roto-evaporation is done in a spherical glass containing the imogolite solution is put after the dialysis. The glass is rotated at 40 turns per minute, and it is immersed in water at 50°C, making that water from the imogolite solution is evaporated. During this process, films of oriented imogolite nanotubes are formed (Figure 2, right).

The diffraction pattern of freeze-dried imogolite obtained using high-energy X-ray radiation is shown in Figure 3 and compared with diffraction patterns from other studies. The abscissa scale has been converted to momentum transfer, *Q*, using equation (1) in order to compare with the results from other authors.

$$Q = \frac{4\pi \sin(\theta)}{\lambda} \qquad (1)$$

where λ is the wavelength of the X-rays and θ is half the diffraction angle (2θ). The signal at low-Q has been enlarged in the inset of Figure 3. The diffraction pattern can be separated in two regions, the limit between them being at 1.25 $Å^{-1}$ (corresponding to interatomic distances d > 5 Å). The first region contains the low-Q part of the pattern, and describes the inter-tube structure. The pattern obtained in this study only contains one peak centered at 0.66 Å, that is also present in the diffraction patterns of (Ohashi et al., 2004). Peaks at lower Q values are not present due to the effect of the beam-stop, optimized to acquire signal from high Q values. The second region, from 1.25 $Å^{-1}$ corresponds to the intra-tubular structure and is very similar in the three samples.

Figure 4 shows the experimental PDF of synthetic imogolite. High frequency oscillations are observed in the signal, due to the truncation effect affecting the Fourier transform (Toby and Egami, 1992). The intensity of the PDF shows a decay, getting to zero at distances of 22 Å. Some authors have attributed this decay to the finite size of the nanoparticles (Gilbert, 2008; Michel et al., 2007a; Michel et al., 2007b; Scheinost et al., 2008), a decay that can be fitted using size models to obtain the diameter of the nanoparticle. However, this result is somehow striking in the PDF of imogolite. The nanotubular structure of imogolite makes that correlations between atoms along the tube axis are expected to appear at $r > 8.4$ Å, the repetition unit along the tube axis. The lack of these correlations has to be interpreted then differently. Actually, what is seen in the PDF is the size of the coherent domain. A hypothesis that could explain this effect is the occurrence of strains in the structure. Strains may induce the formation of coherent nano-domains, whose size could fluctuate due to vibration modes. Vacant sites could be also responsible for the formation of these domains.

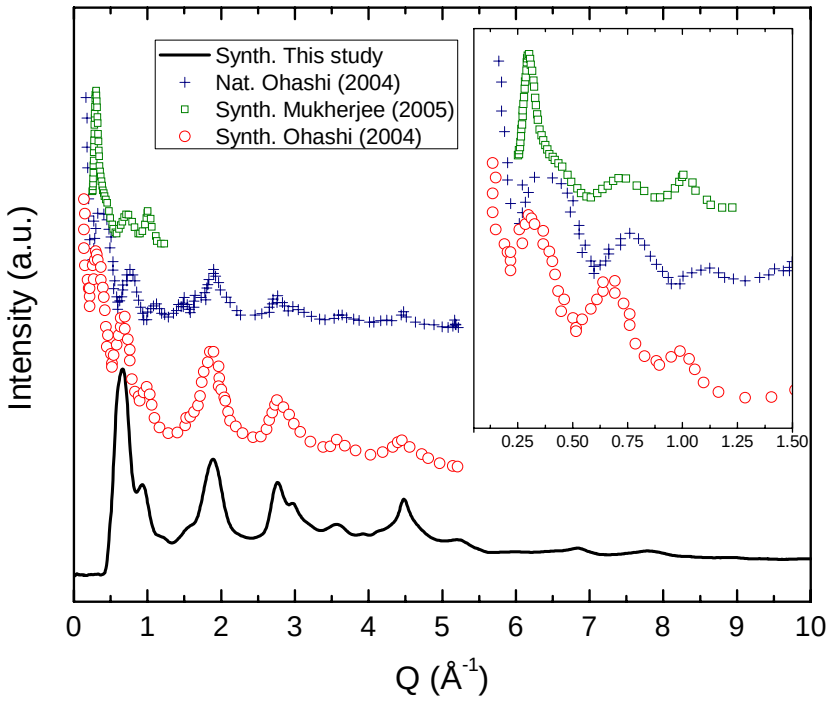


***Figure 3**. Diffraction patterns of synthetic (Synth) and natural imogolite (Nat) obtained in this and other studies (Mukherjee et al., 2005; Ohashi et al., 2004). Positions of the peaks at Q values higher than 1.25 Å^{-1} are similar for all the samples. The signal at low Q (inset) shows differences between the samples. Peaks at low Q values contain information about the packing and the bundle structure, as shown by Mukherjee et al., (2005). The diffraction pattern obtained in this study has been truncated at Q = 10 Å^{-1}, although it reaches a Q_{max}=23.5 Å^{-1}. It does not*

contain data at low Q due to the effect of the beam-stop used in the PDF experiments, which shields the low-Q signal.

Fits of the PDF are presented in Figure 5. The fits were performed using a model of imogolite constructed containing 20 molecular units, as it has been reported by (Cradwick et al., 1972) for natural imogolite. A unit cell of 30 Å × 30 Å × 8.4 Å was used. During the fits, lattice parameters, thermal displacement factors, Al and Si atomic positions and some parameters related to the resolution of the instrument were refined (see Table 1). The use of a whole section of imogolite involves the refinement of many atomic parameters (> 100). For this reason, the obtained structure after PDF fitting was compared to that reported by Cradwick et al., (1972). No significant deviation from the initial structure was observed, which indicates that the model proposed by Cradwick et al., (1972) for natural imogolite fits well the structure of synthetic imogolite. However, the R_w parameter is probably too small due to the high number of parameters allowed to refine. Fits including smaller repetition units were tried without success. The cylindrical symmetry group makes more difficult the fit of the PDF. Further investigations are on going.

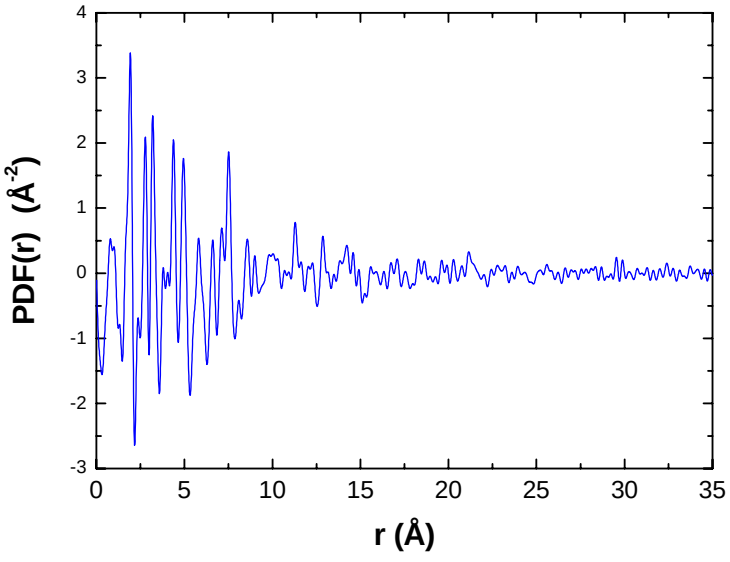


***Figure 4**. PDF of synthetic imogolite. High frequency oscillations are due to a truncation effect affecting the Fourier transform.*

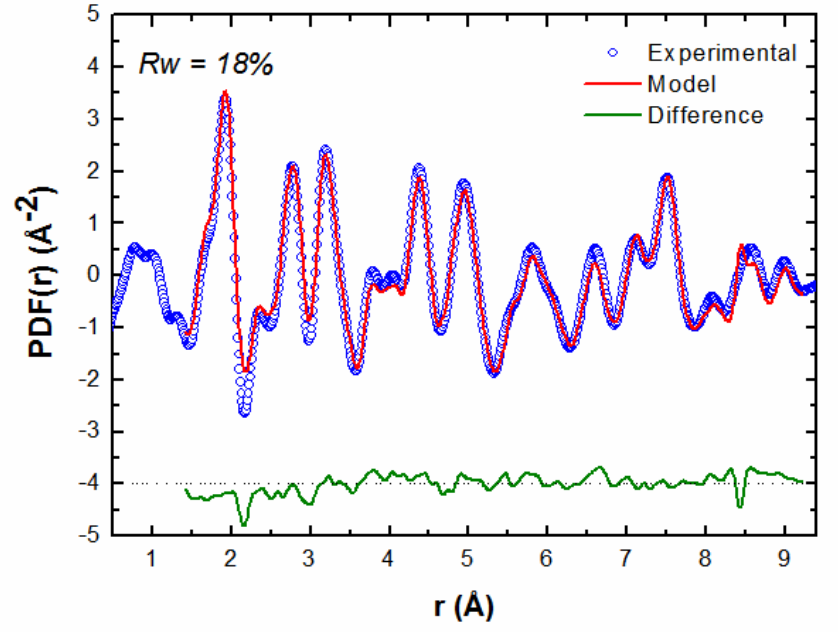


***Figure 5**. PDF of synthetic imogolite. Experimental, fitted and difference curves are shown together with the value of the R_w parameter, which indicates the goodness of the refinement.*

a (Å)	*b* (Å)	*c* (Å)	U_{Al} (Å^2)	U_{Si} (Å^2)	U_O (Å^2)	*d* (Å)	σ_q (Å^{-1})	R_w (%)
29.98(11)	30.13(15)	8.449(14)	0.00092	0.0007	0.002	15.05(50)	0.027	18.48

***Table 1**. Results of the PDF refinements. U stands for the isotropic thermal displacement contributing to the Debye-Waller factor, σ_q is the instrumental dampening factor of the PDFs originated by the limited q-resolution, d is the diameter of the coherent domain size (spherical approximation) and R_w is the weighted agreement factor. The value of the dampening factor was calculated for the LaB_6 standard and kept constant during the refinements of the imogolite PDF.*

The 20-molecular-units structural model used to fit the PDF corresponds to an imogolite with a small diameter, as it has been found for natural imogolite (Cradwick et al., 1972; Farmer et al., 1983). However, the structure of synthetic imogolite has been reported to have bigger diameters (Farmer et al., 1983; Ohashi et al., 2004; Wada, 1987). This discrepancy is due to the fact that the changes in diameter cause only very subtle changes in the local-order of imogolite, within the PDF experimental resolution. Also, the big size of the unit cell and the many parameters involved in the fitting procedure allows small differences to be fitted. Other techniques are better suited to the study of the diameter sizes and polydispersity. (Creton et al., 2008b) suggested using

molecular modeling techniques that the radial breathing mode of imogolite can be observed using Raman spectroscopy, the frequency of this vibrational mode being affected by changes on imogolite diameter. Diffraction techniques (electron and X-ray) reveal also details about the bundle structure.

The structure of synthetic imogolite has been fitted in this work using a structural model of natural imogolite. As indicated above, only the positions of Al and Si atoms have been fitted, the O atoms being fixed. After visual inspection of the resulting structure no significant changes have been observed. In order to check the consistency of the results, we have generated a diffraction pattern of the fitted structured, and compared it with the measured using high-energy X-rays (Figure 6).

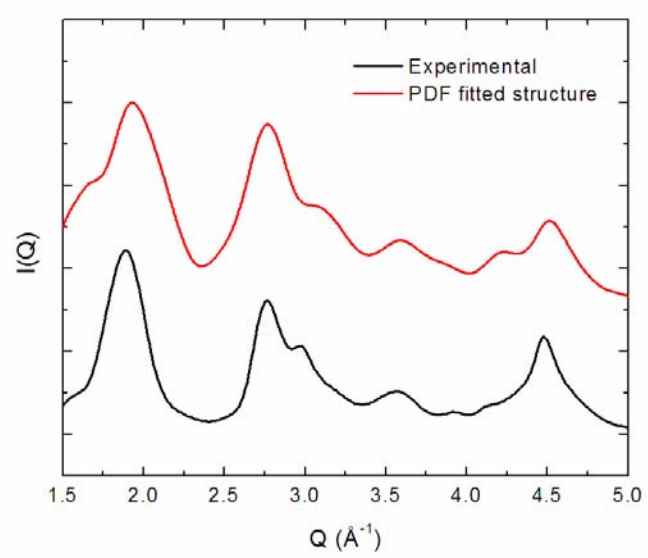


Figure 6. *Experimental and theoretical patterns of the imogolite sample and of the PDF-fitted structure.*

Although some small differences can be appreciated in the positions of the peaks, overall the intra-tube structure is well reproduced. Some authors had reported differences in the structure between natural and synthetic imogolite (Kogure et al., 2003). From this study we can conclude that the local structure of synthetic imogolite is identical to that of natural imogolite. The structure proposed by (Cradwick et al., 1972) is thus valid also for synthetic imogolite. Differences in diameter and in packing properties of imogolite bundles have not been studied here.

Water desorption

Results from CRTA experiments are shown in Figure 7 (blue curve). Weighting the sample before and after the water desorption experiment allows quantifying the weight loss. The use of a mass spectrometer has allowed confirming that the observed weight loss is due to desorption of water molecules. Quantification of the water desorbed at selected temperatures is shown in Table 2. Three peaks can be observed in the water desorption curve (blue curve, Figure 7) of the CRTA spectra, indicating the presence of (at least) three different environments for water. Colors in Figure 7 indicate the temperature ranges in which water from the different environments is desorbed. (Ackerman et al., 1993) proposed the existence of three different pores in bundles of imogolite: (1) the internal pore of the nanotube;

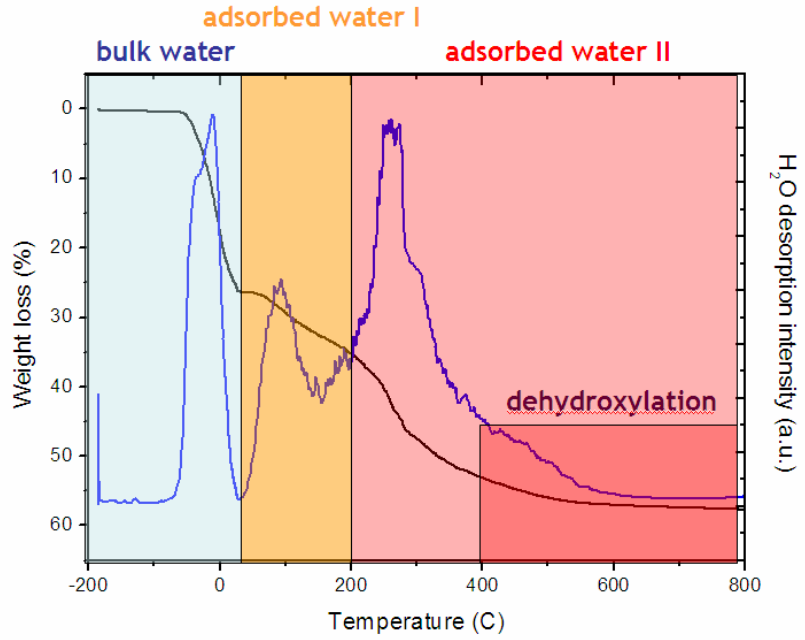


Figure 7*. Results of the CRTA experiment. The blue curve is the water intensity at the mass spectrometer as a function of the temperature. Integration of the blue curve and substraction from the initial mass yields the black curve, which is the weight loss.*

(2) pores formed between the tubes of a same bundle and (3) the pores between different bundles. The first peak in the desorption curve can be assigned then to bulk-like water present in pore (3). This type of water is desorbed under vacuum conditions at room temperature, indicating that low adsorption energies are binding it to the structure. Bulk-like water accounts for a 26 % of the total weight of freeze-dried imogolite. Drying procedures are expected to play an important role on the formation of these pores. As it has been shown in Figure 2, imogolite powders with different textures

can be synthesized by only changing the drying method. Differences in hydration levels between natural samples have been ascribed by other authors to differences in tube alignment (Farmer et al., 1983; Yoshinaga, 1968). (Farmer et al., 1983) reported that better aligned tubes exhibit more intense inter-tube X-ray diffraction diffraction maxima, lower hydration levels and lower dehydroxylation temperatures (shifted by 50°C). Further diffraction studies using the imogolite films and freeze-dried powders shown in Figures 1 and 2 are on-going. The second peak in the desorption curve indicates the presence of adsorbed water molecules, probably in the inter-tubular spacing. Integration of the desorption intensity up to a temperature of 150°C (the position of the minimum between the second and third peaks) yields a weight loss of 33%. The water remaining in the structure at this temperature represents a 27% of the weight, resulting in a number of 149 water molecules per unit cell of imogolite. According to the model of (Cradwick et al., 1972) a unit cell of imogolite contains an internal surface where 20 oxygen atoms are exposed to water, forming hydroxyl groups, and an external surface with 60 oxygen atoms also forming hydroxyl groups. If we define a surface coverage of one water layer as the presence of one adsorbed water molecule per surface oxygen atom, this would mean that 80 water molecules are needed to cover both surfaces of imogolite with one layer of water. However, this description is not entirely correct. Some authors (Creton et al., 2008a)(Fernandez-Martinez, in preparation) have shown that the internal pore of imogolite is more hydrophilic than the external surface. Monte Carlo molecular simulations would be then needed to reproduce the water adsorption isotherms in order to ascertain which pores have adsorption sites with higher adsorption energies. Nevertheless, the water content in the sample after desorption at 150°C, equivalent to 149 water molecules per unit cell, is equivalent, at least, to the formation of two shells of water on each surface.

Temperature (°C)	Weight loss (%)	Remaining stoichiometry	Remaining H_2O per imogolite unit cell	ϕ
27	26	$Al_2SiO_7H_4 \cdot 9H_2O$	184	2.3
150	33	$Al_2SiO_7H_4 \cdot 7H_2O$	150	1.87
287	47	$Al_2SiO_7H_4 \cdot 4H_2O$	72	0.9
350	51	$Al_2SiO_7H_4 \cdot 2H_2O$	48	0.6

Table 2. *Weight loss, stoichiometry of imogolite after degassing, number of water molecules per unit cell after degassing and surface coverage (ϕ). ϕ is defined as the ratio between the number of water molecules and the number of surface oxygen atoms.*

Integration of the water desorption intensity present in the third peak is complicated due to two effects: (1) it has been reported by several authors that the dehydroxylation of the surface starts at ~350°C (Farmer et al., 1983). This temperature falls in the middle of the long tail observed at temperatures between 300°C and 600°C. This tail can thus be explained by two effects: (1) imogolite dehydroxylation occurs breaking the structure of the nanotube, creating holes in the structure from where adsorbed water inside the nanotube pore can desorb, and (2) desorption of water from the nanotube pore is restricted by an steric effect due to the small size of the nanotube pore and to the highly ordered structure of water inside it (Creton et al., 2008a).

The integration of all the desorption curve of water yields a total water content of 54%. This implies that the stoichiometry for synthetic freeze-dried imogolite is $Al_2SiO_7H_4 \cdot 16H_2O$, or a water content of 320 water molecules per unit cell.

Infrared spectroscopy

FTIR spectra have been taken under a vacuum of 10^{-3} bar, at three different temperatures. Results highlighting the stretching vibational mode of water O-H bonds are presented in Figure 8 (left). The stretching band shows a large peak with a long tail extending to lower frequency values. This broad peak is characteristic of confined water. The maximum of the peak is shifted towards higher frequency values as long as the temperature increases. The shape of the band shows a discontinuity when passing from 150°C to 300°C, the signal at 300°C having a sharper shape, indicating that different environments are present for water in imogolite. Differences between the FTIR signals at different temperatures have been done and are shown in Figure 8 (right). The green curve corresponds to the signal of water desorbing from the structure in the temperature range 35°C to 150°C. A similar subtraction has been done between the signal at temperatures 150°C and 300°C (magenta curve). Both curves show a stretching band with similar shape, with a maximum at ~3400 cm^{-1} and shape very different to the band of water at 300°C, cenetered at 3550 cm^{-1}. The black curve (300°C) includes also the vibrations of structural hydroxyl groups that overlap with the signal from water adsorbed in the internal pore of imogolite.

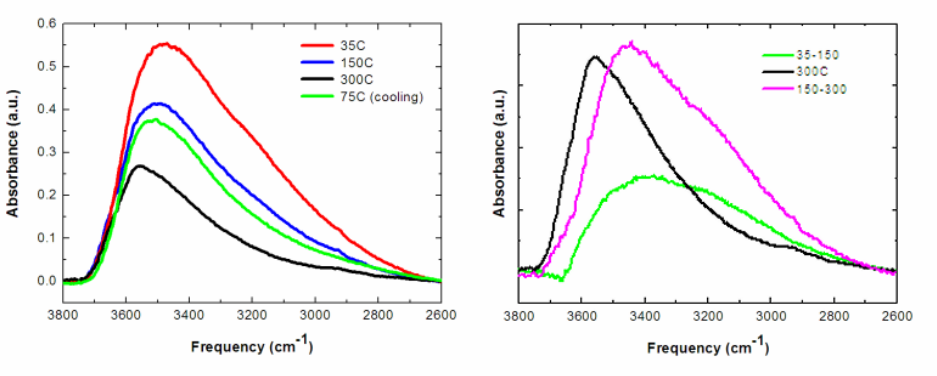


***Figure 8**. FTIR spectra showing the stretching vibational mode of water adsorbed on imogolite at different temperatures. Left: FTIR spectra at four temperatures (one during the cooling). Right: differences between signals at different temperatures.*

The hysteresis effect reported by (Farmer et al., 1983) has been observed during the cooling of the imogolite sample. Prior to the cooling, the vacuum over the sample was broken, allowing its rehydratation under ambient moisture conditions (75%). FTIR spectra taken at a temperature of 75°C during the cooling shows a band with a maximum centered at an intermediate position between the signals of the 150°C and 300°C taken during the heating. This indicates that part of the desorbed water during the heating is not adsorbed back to the sample. Farmer et al., (1983) attributed a similar effect to the irreversible collapse of the bundle structure. The presence of hydroxyl groups at the surface facilitates the formation of strong hydrogen bonds between the nanotubes, if the water residing in the inter-tubular pores is evacuated.

CONCLUSIONS

Different techniques have been applied to the characterization of synthetic imogolite. TEM observations have allowed identifying the presence of open tube edges. The internal surface of the nanotube is thus accessible for the diffusion of water and the ion exchange between the external and internal surfaces. X-ray PDF measurements have revealed a local structure similar to that of natural imogolite. More studies focusing on the diameter polydispersity of synthetic imogolite should be performed to clarify the effect of the different synthesis procedures over the sizes of the final products. Comparisons between low-Q X-ray diffraction patterns show differences in the packing structure of synthetic imogolite nanotubes whose origin is not understood.

The water content of imogolite has been studied experimentally using a combination of CRTA and FTIR spectroscopy. CRTA reveals the presence of three types of adsorbing water that may be adsorbed onto the three pores suggested by Ackerman et al. (1993). Desorption experiments reveal the existence of a steric effect during the desorption of water at high temperatures, corresponding to water from the internal pore of the nanotubes. This steric effect may be due to the long lengths and restricted diffusion of water along the internal imogolite pore. FTIR spectra of the stretching mode of adsorbed water show the existence of two different types of water. FTIR taken during the cooling and at ambient humidity conditions reveal the collapse of the bundle structure.

REFERENCES

Ackerman, W.C., Smith, D.M., Huling, J.C., Kim, Y.W., Bailey, J.K., and Brinker, C.J. (1993) Gas vapor adsorption in imogolite - A microporous tubular aluminosilicate. Langmuir, 9(4), 1051-1057.

Alvarez-Ramirez, F. (2007) Ab initio simulation of the structural and electronic properties of aluminosilicate and aluminogermanate natotubes with imogolite-like structure. Physical Review B, 76(12).

Barrett, S.M., Budd, P.M., and Price, C. (1991) The synthesis and characterization of imogolite. European Polymer Journal, 27(7), 609-612.

Chupas, P.J., Qiu, X.Y., Hanson, J.C., Lee, P.L., Grey, C.P., and Billinge, S.J.L. (2003) Rapid-acquisition pair distribution function (RA-PDF) analysis. Journal of Applied Crystallography, 36, 1342-1347.

Cradwick, P.D., Wada, K., Russell, J.D., Yoshinag.N, Masson, C.R., and Farmer, V.C. (1972) Imogolite, a hydrated aluminum silicate of tubular structure. Nature-Physical Science, 240(104), 187-&.

Creton, B., Bougeard, D., Smirnov, K.S., Guilment, J., and Poncelet, O. (2008a) Molecular dynamics study of hydrated imogolite - 2. Structure and dynamics of confined water. Physical Chemistry Chemical Physics, 10(32), 4879-4888.

-. (2008b) Molecular dynamics study of hydrated imogolite. 1. Vibrational dynamics of the nanotube. Journal of Physical Chemistry C, 112(27), 10013-10020.

Daniels, J.E., and Drakopoulos, M. (2009) High-energy X-ray diffraction using the Pixium 4700 flat-panel detector. Journal of Synchotron Radiation, 16, 1-6.

Denaix, L., Lamy, I., and Bottero, J.Y. (1999) Structure and affinity towards Cd2+, Cu2+, Pb2+ of synthetic colloidal amorphous aluminosilicates and their precursors. Colloids and Surfaces a-Physicochemical and Engineering Aspects, 158(3), 315-325.

Farmer, V.C., Adams, M.J., Fraser, A.R., and Palmieri, F. (1983) Synthetic imogolite - Properties, synthesis and possible applications. Clay Minerals, 18(4), 459-472.

Farmer, V.C., Fraser, A.R., and Tait, J.M. (1977) Synthesis of imogolite - Tubular aluminum silicate polymer. Journal of the Chemical Society-Chemical Communications(13), 462-463.

Farrow, C.L., Juhas, P., Liu, J.W., Bryndin, D., Bozin, E.S., Bloch, J., Proffen, T., and Billinge, S.J.L. (2007) PDFfit2 and PDFgui: computer programs for studying nanostructure in crystals. Journal of Physics: Condensed Matter, 19, 335219-335226.

Gilbert, B. (2008) Finite size effects on the real-space pair distribution function of nanoparticles. Journal of Applied Crystallography, 41, 554-562.

Guimaraes, L., Enyashin, A.N., Frenzel, J., Heine, T., Duarte, H.A., and Seifert, G. (2007) Imogolite nanotubes: Stability, electronic, and mechanical properties. Acs Nano, 1(4), 362-368.

Hammersley, A.P., Svensson, S.O., Hanfland, M., Fitch, A.N., and Hausermann, D. (1995) Two-dimensional detector software: From real detector to idealised image or two-theta scan. 4th Workshop of the IUCr High Pressure Group on Synchrotron and Neutron Sources, p. 235-248, Kek, Japan.

Kogure, T., Suzuki, A., Mitome, M., and Bando, Y. (2003) Quantitative electron diffraction analyses of natural and synthetic imogolites. 13th Annual VM Goldschmidt Conference, p. A226-A226. Pergamon-Elsevier Science Ltd, Kurashiki, Japan.

Konduri, S., Mukherjee, S., and Nair, S. (2006) Strain energy minimum and vibrational properties of single-walled aluminosilicate nanotubes. Physical Review B, 74(3).

Michel, F.M., Ehm, L., Antao, S.M., Lee, P.L., Chupas, P.J., Liu, G., Strongin, D.R., Schoonen, M.A.A., Phillips, B.L., and Parise, J.B. (2007a) The structure of ferrihydrite, a nanocrystalline material. Science, 316(5832), 1726-1729.

Michel, F.M., Ehm, L., Liu, G., Han, W.Q., Antao, S.M., Chupas, P.J., Lee, P.L., Knorr, K., Eulert, H., Kim, J., Grey, C.P., Celestian, A.J., Gillow, J., Schoonen, M.A.A., Strongin, D.R., and Parise, J.B. (2007b) Similarities in 2-and 6-line ferrihydrite based on pair distribution function analysis of X-ray total scattering. Chemistry of Materials, 19(6), 1489-1496.

Mukherjee, S., Bartlow, V.A., and Nair, S. (2005) Phenomenology of the growth of single-walled aluminosilicate and aluminogermanate nanotubes of precise dimensions. Chemistry of Materials, 17(20), 4900-4909.

Ohashi, F., Tomura, S., Akaku, K., Hayashi, S., and Wada, S.I. (2004) Characterization of synthetic imogolite nanotubes as gas storage. Journal of Materials Science, 39(5), 1799-1801.

Qiu, X.Y., Bozin, E.S., Juhas, P., Proffen, T., and Billinge, S.J.L. (2004) Reciprocal-space instrumental effects on the real-space neutron atomic pair distribution function. Journal of Applied Crystallography, 37, 110-116.

Scheinost, A.C., Kirsch, R., Banerjee, D., Fernandez-Martinez, A., Zaenker, H., Funke, H., and Charlet, L. (2008) X-ray absorption and photoelectron spectroscopy investigation of selenite reduction by Fe-II-bearing minerals. Journal of Contaminant Hydrology, 102(3-4), 228-245.

Tamura, K., and Kawamura, K. (2002) Molecular dynamics modeling of tubular aluminum silicate: Imogolite. Journal of Physical Chemistry B, 106(2), 271-278.

Toby, B.H., and Egami, T. (1992) Accuracy of Pair Distribution Function analysis applied to crystalline and noncrystalline materials. Acta Crystallographica Section A, 48, 336-346.

Ugolini, F.C., and Dahlgren, R.A. (1991) Weathering environments and occurrence of imogolite and allophane in selected andisols and spodosols. Soil Science Society of America Journal, 55(4), 1166-1171.

Wada, K. (1989) Allophane and imogolite. In J.B. Dixon, and S.B. Weed, Eds. Minerals in soil environments, p. 1051-1087.

Wada, S.I. (1987) Imogolite synthesis at 25 degrees C. Clays and Clay Minerals, 35, 379-384.

Wada, S.I., Eto, A., and Wada, K. (1979) Synthetic allophane and imogolite. Journal of Soil Science, 30(2), 347-&.

Yoshinaga, N. (1968) Identification of imogolite in the filmy gel materials in the Imaichi and Shichihonzakura pumice beds. Soil Science Plant Nutrition, 14, 238-246.

Zang, J., Konduri, S., Nair, S., and Sholl, D.S. (2009) Self-Diffusion of Water and Simple Alcohols in Single-Walled Aluminosilicate Nanotubes. Acs Nano, 3(6), 1548-1556.

Annex II

- Papers related to this thesis published by the author during the last three years:

1. Montes-Hernandez G., Fernandez-Martinez A., Renard F. Novel method to estimate the linear growth rate of submicrometric calcite produced in a triphasic gas-liquid-solid system. *Crystal Growth and Design* 2009, 9, 4567-4573.

2. Fernandez-Martinez A. and Charlet L. Selenium bioavailability and cycling in the environment: a structural chemist point of view. *Reviews in Environmental Science and Biotechnology* 2009, 8, 81-110.

3. Scheinost A. C., Kirsch R., Banerjee D., Fernandez-Martinez A., Zaenker H., Funke H., Charlet L. X-ray absorption and photoelectron spectroscopy investigation of selenite reduction by Fe(II)-bearing minerals. *Journal of Contaminant Hydrology* 2008, 102, 228-245.

4. Montes-Hernandez G., Fernandez-Martinez A., Scheinost A. C., Bueno M., Charlet L. and Renard F. Synthesis of a Se(0)/calcite composite using hydrothermal carbonation of $Ca(OH)_2$ coupled to a complex selenocystine fragmentation. *Crystal Growth and Design* 2008, 8, 2497-2504.

5. Fernandez-Martinez A., Cuello G. J., Johnson M. R., Bardelli F., Roman-Ross G., Charlet L. and Turrillas X. Arsenate incorporation in gypsum probed by neutron, X-ray scattering and DFT modelling. *Journal of Physical Chemistry A* 2008, 112, 5159-5166.

6. Montes-Hernandez G., Fernandez-Martinez A., Charlet L., Tisserand D. and Renard F. Textural properties of synthetic nano-calcite produced by hydrothermal carbonation of calcium hydroxide. *Journal of Crystal Growth* 2008, 310, 2946-2953.

7. Charlet L., Scheinost A. C., Tournassat C., Greneche J. M., Gehin A., Fernandez-Martinez A., Coudert S., Tisserand D. and Brendle J. Electron transfer at the mineral/water interface: Selenium reduction by ferrous iron sorbed on clay. *Geochimica Cosmochimica Acta* 2007, 71, 5731-5749.

8. Fernandez-Martinez A., Roman-Ross G., Cuello G. J., Turrillas X., Charlet L., Johnson M. R. and Bardelli F. Arsenic uptake by gypsum and calcite: modeling and probing by neutron and x-ray scattering. *Physica B: Condensed Matter* 2006, 385-386, 935-937.

9. Roman-Ross G., Cuello G. J., Turrillas X., Fernandez-Martinez A. and Charlet L. Arsenite sorption and co-precipitation by calcite. *Chemical Geology* 2006, 233, 328.

- Other papers/book chapter published by the author during the last three years:

1. Gorria P., Martinez-Blanco D., Perez M. J., Blanco J. A., Hernando A., Laguna-Marco M. A., Haskel D., Souza-Neto N., Smith R. I., Marshall W. G., Garbarino G., Mezouar M., Fernandez-Martinez A., Chaboy J., Fernandez-Barquin L., Rodriguez Castrillon J. A., Moldovan M., Garcia Alonso J. I., Zhang J., Llobet A., Jiang J. S. Stress-induced large Curie temperature enhancement in $Fe_{64}Ni_{36}$ Invar alloy. *Physical Review B* 2009, 80, 064421.

2. Cuello G. J., Roman-Ross G., Fernandez-Martinez A., Sobolev O., Charlet L. and Skipper N. T. Pollutant speciation in water and related environmental treatment issues. In *Neutron applications in Earth, Energy and Environmental Sciences*. 'Neutron scattering applications and techniques' series. Edited by Liang L., Rinaldi R. and Schober H. Springer Ed. (2009).

3. Gorria P., Boada R., Fernandez-Martinez A., Garbarino G., Smith R. I., Chaboy J., Garcia Alonso J. I., Martinez-Blanco D., Castro G. R., Mezouar M., Hernando A. and Blanco J. A. Stress-induced Curie temperature increase in the $Fe_{64}Ni_{36}$ invar alloy. *Physica Status Solidi - Rapid Research Letters* 2009, 4, 115-117.

4. Fernandez-Martinez A., Martinez-Blanco D., Perez M. J., Cuello G. J., Castro G. R., Gorria P. and Blanco J. A. Structural and magnetic study of mechanically-alloyed $Fe_{30}Cr_{70}$ by neutron thermo-diffractometry and magnetization measurements. *Journal of Non-Crystalline Solids* 2008, 354, 5156-5158.

5. Cristiglio V., Hennet L., Cuello G. J., Johnson M. R., Fernandez-Martinez A., Fischer H. E., Pozdnyakova I., Zanghi D., Brassamin S., Brun J. F. and Price D. L. Ab-initio molecular dynamics simulations of the structure of liquid aluminates. *Journal of Non-Crystalline Solids* 2007, 353, 1789-1792.

6. Cuello G. J., Piarristeguy A. A., Fernandez-Martinez A., Fontana M. and Pradel A. Structure of chalcogenide glasses by neutron diffraction. *Journal of Non-Crystalline Solids* 2007, 353, 729-732.

7. Fernandez-Martinez A., Gorria P., Cuello G. J., Santos J. D. and Perez M. J. Kinetics of crystallization of FeB-based amorphous alloys studied by neutron thermodiffractometry. *Journal of Non-Crystalline Solids* 2007, 353, 855-858.